PHOTONIC DEVICES BASED ON ENGINEERED SILICON STRUCTURES FOR OPTICAL GUIDANCE AND MODULATION

Ph.D. Thesis

by

Sourabh Jain

Under the supervision of

Dr. Mukesh Kumar
&
Dr. Arvind Kumar Srivastava (Co-supervisor, RRCAT, Indore)

DISCIPLINE OF ELECTRICAL ENGINEERING

INDIAN INSTITUTE OF TECHNOLOGY INDORE

JULY 2020

PHOTONIC DEVICES BASED ON ENGINEERED SILICON STRUCTURES FOR OPTICAL GUIDANCE AND MODULATION

A THESIS

Submitted in partial fulfillment of the requirements for the award of the degree

of

DOCTOR OF PHILOSOPHY

by

Sourabh Jain

Under the supervision of

Dr. Mukesh Kumar
&
Dr. Arvind Kumar Srivastava (Co-supervisor, RRCAT, Indore)

DISCIPLINE OF ELECTRICAL ENGINEERING

INDIAN INSTITUTE OF TECHNOLOGY INDORE

JULY 2020

INDIAN INSTITUTE OF TECHNOLOGY INDORE

CANDIDATE'S DECLARATION

I hereby certify that the work which is being presented in the thesis entitled "**Photonic Devices Based On Engineered Silicon Structures For Optical Guidance And Modulation**" in the partial fulfillment of the requirements for the award of the degree of **Doctor Of Philosophy** and submitted in the **Discipline Of Electrical Engineering, Indian Institute of Technology Indore**, is an authentic record of my own work carried out during the time period from July 2016 to July 2020 under the supervision of Dr. Mukesh Kumar, Associate Professor, Discipline of Electrical Engineering, IIT Indore.

The matter presented in this thesis has not been submitted by me for the award of any other degree of this or any other institute.

Signature of the student with date
(SOURABH JAIN)

This is to certify that the above statement made by the candidate is correct to the best of my/our knowledge.

22/7/2020

Signature of Thesis Supervisor with date
(Dr. Mukesh Kumar)

Signature of External Thesis Supervisor with date
(Dr. Arvind Kumar Srivastava)

Sourabh Jain has successfully given his/her Ph.D. Oral Examination held on **14-Dec-2020**

Signature of Chairperson (OEB)
Date: 14/12/2020

Signature of External Examiner
Date:

Signature of Thesis Supervisor
Date: 14/12/2020

Signature of External-Supervisor
Date:

S. Mukherjee
Signature of PSPC Member #1
Date: 14/12/2020

Signature of PSPC Member #2
Date: 14/12/2020

Signature of Convener, DPGC
Date: 14/12/2020.

(Acting Head, EE)
Signature of Head of Discipline
Date: 14/12/2020

I

Acknowledgments

This thesis is the cumulative outcome of four years in which many people have made their contributions through guidance, advice, energy, and constructive criticism. This thesis has become a reality with the kind support, love, care, motivation, enthusiasm, and the help of many individuals. I express my gratitude to everyone who supported me throughout the journey of my research. I would like to take this opportunity to acknowledge them all who prepared me for this achievement.

Foremost, I would like to express my sincere gratitude to my respectable thesis supervisor, ***Dr. Mukesh Kumar*** *for his aspiring guidance, invaluably constructive opinion, and sincere advice during this journey. I am truly grateful to him for his unwavering support in enlightening me with his insightful and illuminating views and discussion on several issues related to the project and research. It was great learning about professionalism, perfection, and devotion, by working with him during my entire Ph.D. His guidance helped me all the time in my research. I am thankful to him for providing his precious time and suggestions for my thesis corrections. I feel a deep sense of respect for him and I surely can say that I could not have imagined having a better supervisor for my Ph.D. research.*

I am also highly indebted to my co-thesis supervisor, ***Dr. Arvind Srivastava,*** *and PSPC members,* ***Dr. Shaibal Mukherjee****, and* ***Dr. Kapil Ahuja****, for the considerate endorsement and their honest, cooperative response and queries solicited in this study. I am thankful to Convener, DPGC for all immense help. I am thankful to* ***Dr. Pragya Tiwari*** *and* ***Mr. Puspen Mondal*** *from Raja Ramanna Centre for Advanced Technology (RRCAT) Indore for providing in-depth and handful knowledge of fabrication and techniques.*

I want to express my deep gratitude to Optoelectronic Nanodevice Research Laboratory (ONRL), IIT Indore and colleagues, Mr. Lalit Singh, Mr. Sulabh, Mr. Vishal Kaushik, Ms. Swati Rajput, Mr. Suresh Pandey, Mr. Rahul Mishra and Mr. Prem Babu who helped me in various ways during my thesis work and for providing invaluable support and motivation.

I would like to extend my sincere thanks to all my seniors, juniors, and friends at IIT Indore, Dr. Ambika Prashad, Dr. Rajeev Sharma, Dr. Prateek Bhojane, Dr. Chinky Binnani. Dr. Jasmine, Dr. Dharmendra, Mr. Vijay, Ms. Priya, and Mr. Palash for all encouragement and understanding through all these years of my Ph.D.

I would like to express my sincere thanks to my loving families. I express my deep sense of gratitude to my parents ***Mr. Narendra Kumar Jain*** *and* ***Mrs. Saroj Jain*** *for their love and faith they kept in my dreams. My special thanks go to my younger brother **Gaurav Jain**, and my loving sister **Kavita Jain** and **Jijaji**, for all their constant help, love, and support. I would also like to acknowledge my mother-in-law **Mrs. Nirmala Rathi** for her constant support, especially at the time of arrival of my angel daughter when I was completely indulging with my work, she took care of both my wife & daughter. I am deeply indebted to my sister-in-law **Mrs. Neha Maheshwari**, brother-in-law **Mr. Varun Maheshwari** and **Mr. Abhilash Rathi** for celebrating each accomplishment and for helping in whatever way they could during this challenging period.*

*Dreams give wings to fly. This is not only me who did this dissertation, else, it is the combined effort made by us. She is my motivation, my reason to make efforts without letting down, and most important my backbone, YES, I am talking about my loving and caring wife **Reena.** I appreciate her for being there in my hard times during the journey of Ph.D. For all her love she showered over me and moral support which always gave me strength for doing better. I would like to appreciate her selflessness and kindness for giving me the strength to overcome all the difficulties. My great support to this journey is made by my little daughter **Prisha** who gives me a smile even when I came up with full stress. I used to forget my tiredness when she recites rhymes in her sweet voice. Thank you for allowing me time away from you to research and write. At last, I am sincerely thankful to "**Aacharya, Vidhyasagarji Maharaj**" for the blessings, he has bestowed upon me and for giving me the strength and wisdom to achieve my dream destination. Finally, I thank my God "The superpower" for letting me through all the difficulties and I will keep on trusting you for my future. Thank you "**LORD**".*

Words are short to express my deep sense of gratitude, but at the end of this journey, it is my great pleasure to thank them all who contributed in many ways to my success and made it an unforgettable experience for me.

Thank You!!!!!

Sourabh Jain

"The more you know, the more you know that you don't know"

This thesis is dedicated to

"TO OUR CORONA WARRIORS"

Abstract

The development of electronic photonic integrated circuits (EPIC) has revolutionized inter/intra chip short-haul communication by replacing bandwidth-limited metal interconnects with high-speed optical interconnects. Silicon photonics is playing a major role in the growth of EPIC that enables the fabrication of various on-chip photonic components on matured CMOS platform. This dissertation investigates the guidance and electrical control of light in photonic structure-based engineered silicon for application in optical modulation. Here, mainly four issues are identified for an optical modulator working in depletion and injection modes of operation, those are: (i) RC time constant limited bandwidth in lumped electrode-based electro-optic modulator, (ii) weak coupling between RF and optical modes at higher microwave frequencies in traveling-wave electrode-based configuration, (iii) FSR limited and highly thermal sensitive optical characteristics in resonant based structure, and (iv) shifting of transmission dip/peak in resonance-based optical structure with applying an electric field.

A high-speed electro-optic modulator based on CMOS compatible silicon waveguide is proposed to improve coupling between RF and optical mode. The optical waveguide in silicon is formed by creating a slot in a rib structure that results in strong optical confinement with an acceptably low propagation loss. The proposed design of the slotted-rib waveguide with a traveling-wave electrode facilitates an efficient optical modulation in silicon. Taking the advantage of velocity matched between optical and microwave modes, a high-speed operation up to 70 Gbps with an extinction ratio of ≈ 4.9 dB is reported at a peak to peak voltage of 3 V_{pp} under a reverse bias of 4 V. An insertion loss of 3.1 dB is obtained for a 4 mm long device. However, moderate modulation efficiency remains a major issue with the proposed device structure.

The given issue of moderate modulation efficiency is considered in the next work, where optical modulation in silicon with high data rate and high modulation efficiency is proposed by a laterally separated vertical p-n junction. Two independent but synchronized p-n junctions that support the common

optical mode are created by forming a slot waveguide structure. It provides a prominent way to enhance the light-material interaction necessary to achieve low $V_{\pi}L$ along with the low RC time constant which is crucial for the high-speed operation. The proposed device shows a high modulation efficiency of 0.74 V-cm for a 1.2 mm long device. The calculated intrinsic 3-dB bandwidth reaches up to ≈ 58 GHz at a reverse bias of 6 V. We show high-speed operation up to 25 Gbit/s for the device length of 600 μm with a simple lumped electrode configuration. The Traveling-wave electrodes as a coplanar waveguide are employed to further improve the speed performance of the device. By taking advantage of excellent velocity matching between optical group index and RF effective index, high data rate performance up to 100 Gbit/s is obtained with an extinction ratio of 2.4 dB. The proposed device opens new avenues for high speed optical interconnect on an SOI platform.

In order to achieve a compact on-chip device with a novel guiding mechanism, a silicon-based compact comb-like asymmetric grating is proposed as a thermally stable optical filter for multi-functional applications such as bio-sensor, electro-optic modulator, DWDM, etc. The device is designed and fabricated with a cavity section introduced between the two grating regions which are partially etched in the lateral direction to ensure the nonzero coupling of the fundamental and first-order modes in the propagation and counter-propagation direction. To demonstrate efficient optical guidance in the proposed device, refractive index sensing based on resonance shift in the spectrum is demonstrated with sodium chloride (NaCl) dissolved in DI water. In contrast to conventional Bragg grating where stopband lies in the transmission spectrum, the proposed device allows a single narrow passband transmission peak with a large Free Spectral Range (FSR) attributed to the engineered photonic bandgap of two modes present in the waveguide region. The device is deliberately designed such that slightly wide resonance peak is obtained that makes device operation thermally stable for a large temperature variation of ±15 K. A higher-order leaky mode with strong light-analyte interaction (due to long corrugation width) in the gratings governs high sensitivity of ≈ 352 nm/RIU for different concentrations of NaCl from 0% to 10% in the Deionized (DI) water with a small footprint area of 18 μm^2 only. Proposed filter characteristics are well suited for multifunctional applications in integrated photonic devices. However, fabrication of the proposed device is complex due to the presence of two grating periods of nearly equal dimensions.

Further, to ease the fabrication complexity in the dual perturbed structure, next we proposed a tapered cavity coupled comb-like asymmetrical grating-based optical filter where both set of gratings are having an equal grating period and duty cycle. The narrow FWHM of 1.2 nm with a high extinction ratio of 14 dB is demonstrated in the fabricated device. In addition to the measured optical guidance mechanism, we theoretically investigate electrically tunable optical characteristics of the device by considering the two p-n junctions formed in both sets of gratings. Optical signal tunability is reported in two different ways: (i) resonance peak shift with an applied bias to one set of gratings, (ii) tuning of peak resonance intensity at a fixed wavelength using a programmable set of bias voltages at both the junctions. A high reduction of nearly 79% is achieved with the given multi-bias approach.

List of Publications

(A) Publications from Ph.D. thesis work

A1. In refereed Journals:

1. S. Jain, S. Rajput, V. Kaushik, and M. Kumar, “High speed optical modulator based on silicon slotted-rib waveguide,” Optics Communications, vol. 434, pp. 49–53, 2019.
2. S. Jain, S. Rajput, Sulabh, V Kaushik, and M. Kumar, “Efficient Optical Modulation with High Data-rate in Silicon Based Laterally Split Vertical p-n Junction”, IEEE Journal of Quantum Electronics, vol.56(2). pp.1-7, 2020.
3. S. Jain, Sulabh, S. Rajput, L. Singh, P. Tiwari, A. Shrivastava, and M. Kumar, “Thermally stable optical filtering using silicon-based comb-like asymmetric grating for sensing applications,” IEEE Sensors Journal, vol.20 (7) pp.3529-3535, 2020.

A2. In refereed conferences:

1. S. Jain, L. Singh, S. Rajput and M. Kumar,” Low Group Index Optical Slot Structure for Efficient Optical Modulation”, Conference on Laser and Electro-Optics CLEO-2020, San-Jose, California, USA, 2020.
2. S. Jain, L. Singh, S. Rajput, and M. Kumar,” Waveguide Engineering in Optical Slot Structure for Efficient Optical Modulation”, International Conference on Optics and Electro-Optics ICOL-2019, DRDO, Dehradun, 2019.
3. S. Jain, S. Rajput, and M. Kumar,” Phase Modulation in Optical Hollow Waveguide Embedded in Silicon p-i-n Junction”, Photonics-2018, IIT Delhi, 2018.
4. S. Jain, V. Kaushik, S. Rajput and M. Kumar, “Silicon-based Broadband Reflector for on-chip photonic devices”, International Symposium on Integrated Functionalities ISIF-2017 held at Shangri LA’s Eros Hotel, New Delhi, India, 2017.

(B) Other publications during PhD

B1. In refereed Journals:

1. L. Singh, S. Jain, and M. Kumar, "Electrically Writable Silicon Nanophotonic Resistive Memory with Inherent Stochasticity," Optics Letters, 2019. Vol. 44(16), pp. 4020- 4023, 2019.
2. S. Rajput, V. Kaushik, S. Jain, and M. Kumar, "Slow Light Enhanced Phase Shifter Based on Low-Loss Silicon-ITO Hollow Waveguide", IEEE Photonics Journal, Vol.11, No.1, pp.1-8, February 2019.
3. Sulabh, L. Singh, S. Jain, and M. Kumar, "Optical Slot Waveguide with Grating-Loaded Cladding of Silicon and Titanium Dioxide for Label-Free Bio-Sensing," in IEEE Sensors Journal, vol. 19, no. 15, pp. 6126-6133, 1 Aug.1, 2019.
4. S. Rajput, V. Kaushik, S. Jain, and M. Kumar, "Optical Modulation in Hybrid Waveguide based on Si-ITO Heterojunction" Journal of Lightwave Technology", vol.38(6), pp.1365-1371, 2020.
5. S. Rajput, V. Kaushik, S. Jain, and M. Kumar, "Slow light Assisted Electrical Tuning in Hollow Optical Waveguide via Carrier Depletion in Silicon and Indium Tin Oxide Gratings" JOSA-B". (Accepted-2020)
6. V. Kaushik, S. Rajput, Sulabh, S. Jain, L. Singh, and M. Kumar, "Efficient Sub-bandgap Photodetection via Two-Dimensional Electron Gas in ZnO Based Heterojunction", Journal of Lightwave Technology. DOI: 10.1109/JLT.2020.3003371, 2020.
7. Sulabh, L. Singh, S. Jain, and M. Kumar "Nanophotonic Device based on Fano Resonance in Engineered Slot Waveguide for Optical Detection of Hepatitis B" "IEEE Sensor" (First Revision Submitted).

B1. In refereed Conferences:

1. L. Singh, R. D. Mishra, S. Rajput S. Jain, and M. Kumar, "Enhanced Optical Readout in Resistive Memory Through Plasmonic Amplification," European Conference on Interventional Oncology, ECIO-2020, Paris, France, June 2020.

2. L. Singh, S. Jain, S. Rajput, and M. Kumar," Loss Compensation in Hybrid Plasmonic Waveguide by Controlled Electron Injection", International Conference on Optics and Electro-Optics ICOL-2019, DRDO, Dehradun, 2019.

3. S. Rajput, V. Kaushik, S. Jain, and M. Kumar," Electrically Tunable Absorption in Hollow Waveguide for Optical Modulation", International Conference on Optics and Electro-Optics ICOL-2019, DRDO, Dehradun, 2019.

4. S. Rajput, S. Jain, V. Kaushik, and M. Kumar "High-speed optical modulation in compact hybrid silicon-graphene based slot waveguide" Photonics-2018, IIT Delhi, 2018.

5. S. Rajput, V. Kaushik, S. Jain and M. Kumar "International Symposium on Integrated Functionalities ISIF-2017" held at Shangri LA's Eros Hotel, New Delhi, India.

Table of Contents

List of Figures

List of Tables

List of Abbreviations

IC:	Integrated Circuit
PIC:	Photonic Integrated Circuit
c-Si:	crystalline Silicon
CMOS:	Complementary metal oxide semiconductor
VLSI:	Very Large-Scale Integration
BOX:	Buried-Oxide
SOI:	Silicon-On-Insulator
MZI:	Mach Zehnder Interferometer
SMF:	Single Mode Fiber
MMF:	Multi-Mode Fiber
SWG:	Sub-Wavelength Grating
DBR:	Distributed Bragg Reflector
HCG:	High Contrast Grating
MRR:	Micro Ring Resonator
EO:	Electro-Optic
ER:	Extinction Ratio
C-Band:	Conventional Wavelength Band (1527 to 1567 nm)
L-Band:	Long wavelength band (1567 to 1607 nm)
TE:	Transverse Electric (polarization)
TM:	Transverse Magnetic (polarization)
DC:	Direct Current
AC:	Alternating Current
DI:	De-ionized (water)
EOE:	Electrical-Optical-Electrical
DUT:	Device Under Test
FSR:	Free Spectral Range
ICP:	Inductively Coupled Plasma
OADM:	Optical Add-Drop Multiplexer
RIE:	Reactive Ion Etching
SEM:	Scanning Electron Microscope
EBL:	Electron Beam Lithography

RIE:	Reactive Ion Etching
WDM:	Wavelength-Division-Multiplexing
EAM:	Electro Absorptive Modulator
ERM:	Electro Refractive Modulator
TW:	Traveling Wave
CPW:	Co-Planner Waveguide
FKE:	Franz-Keldysh Effect
QCSE:	Quantum Confined Stark Effect
MUX:	Multiplexer
PRBS:	Pseudo-Random Binary Sequence
NRZ:	Non-Return to Zero

List of Symbols

n: Refractive index

neff: Effective refractive index

Λ: Pitch or Period

ϵ: Permittivity

q: Charge of electron

Z_0: Intrinsic Impedance

γ: Propagation Constant

α: Attenuation Constant

β: Phase Constant

V_π: Half wave Voltage

Φ: Phase of the electro-magnetic wave

R: Resistance

L: Inductance

C: Capacitance

V_{pp}: Peak to peak Voltage

Γ: Overlap integral coefficient\

c: Speed of light

e: Electron

h: Hole

k: Wavenumber

Chapter 1 Introduction to integrated photonics

Integrated photonics is an emerging branch of photonics in which waveguides and devices are fabricated as an integrated structure onto the surface of a flat substrate. As a result of integration, complex photonic circuits can now process and transmit light in similar ways to how electronic integrated circuits process and transmit electronic signals. In this chapter, we discuss the fundamental limitations of the electronic-based structures and evolution of integrated photonics to enhance the computational capabilities of the system. We also discuss the guiding mechanism of the light signal in various silicon-based optical structures and the importance of optical modulation in photonic electronic integrated circuits.

1.1 Background and Motivation

Progressively more and more transistors are incorporating into a single chip to enhance the computational capabilities of the modern electronic system. In recent years, progress in the direction of achieving the smallest feature size on the chip is one of the top research topics. In this regard, VLSI industries are continuously looking forward to the lower technology node. At present,

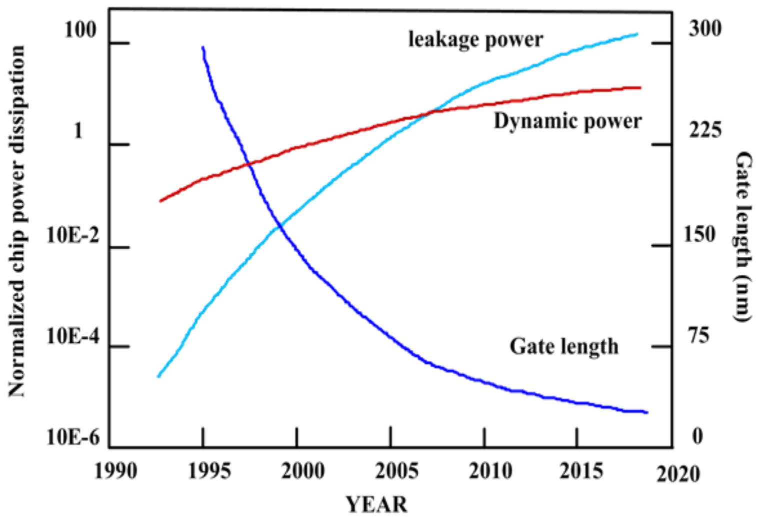

Figure 1.1 International Technology Roadmap for Semiconductor (ITRS) based static and dynamic power dissipation trends in chip [5].

semiconductor manufacturing process industries like Intel, Samsung, TSMC are presently working on 7 nm node technology[1,2] using the Extreme Ultraviolet Lithography (EUV) technique and it is expected to replace it by 5 nm technology node by 2021-22. Advancement with each technology node enables the placing of more number of transistors in a given area. For example, transistor density in the “Apple-A13” phone has reached 863 million per cm^2 using a 7 nm technology node[3,4]. This number is expected to increase by several folds in the coming years. The performance of the electronic chips has been improved tremendously with a heavily dense integrated circuit. However, it is not as simple to increase the computational capabilities with highly dense CMOS circuitry, especially when feature size is less than 100 nm. It is because of two major challenges that arise with each advance technology nodes: The power dissipation and the interconnect delay. With each advanced technology node, leakage power in the chip increases rapidly compared to the active power [5] as shown in Fig. 1.1.

The interconnect delay is another serious issue in the electronic integrated circuits. It causes an increase in the RC time constant and delays in the transmission line with a smaller technology node. The delay is mainly due to the long global metallic interconnections within the IC. The interconnect delay of these metallic wires is near to 150-250 ps which further increases with the length and finer wires. It limits the bandwidth of the system and thus it becomes difficult to achieve high performance integrated circuits [6,7]. The abovementioned drawbacks of electronic chips make it inadmissible for the future communication system and therefore smart systems are needed to enhance capabilities of an integrated circuit by reducing leakage power dissipation and interconnect delay. Moreover, the CMOS fabrication platform is adequately developed, and it has captured a big market due to its cost-effective and large-scale production capabilities.

The real motivation behind this work is to overcome the issue of high interconnect delay and power dissipation on the same CMOS compatible fabrication platform. It can be done with the use of photonics. Photonics is the science and technology where generation to harnessing of a photon with means of electronic medium is studied. The high-frequency range of the light signal (in THz) imparts inherently high bandwidth to the photon-based devices. It enables numerous high-performance applications that are currently playing a big role at a verity of places like telecommunication, health care, aerospace, environmental monitoring, etc.

1.2 Silicon Photonics

There is a wide range of materials that are utilizing for the realization of multiple functionalities in photonic based devices. However, most of the materials are not compatible with CMOS fabrication platform, thus it becomes difficult to integrate devices made up of those materials on highly dense integrated circuits. To achieve CMOS compatible fabrication flow, devices made of Si is completely integrable with the pre-existed electronics integrated circuits and offers highly compact and cost-effective devices. It became possible with the invention of a fortunate low optical loss window in silica that centered near to 850 nm, 1310 nm, and 1550 nm wavelength and gave birth to "Silicon Photonics" [8,9]. It opens the opportunity to utilize the same material in the optical regime. Fig. 1.2 shows the loss spectra of the silica fiber[10], the main cause of optical losses is Rayleigh scattering, absorption through various metallic impurities, tiny water droplets in the fiber, and silica molecule itself. The Rayleigh scattering loss is minimum for the longer wavelength as it decreases

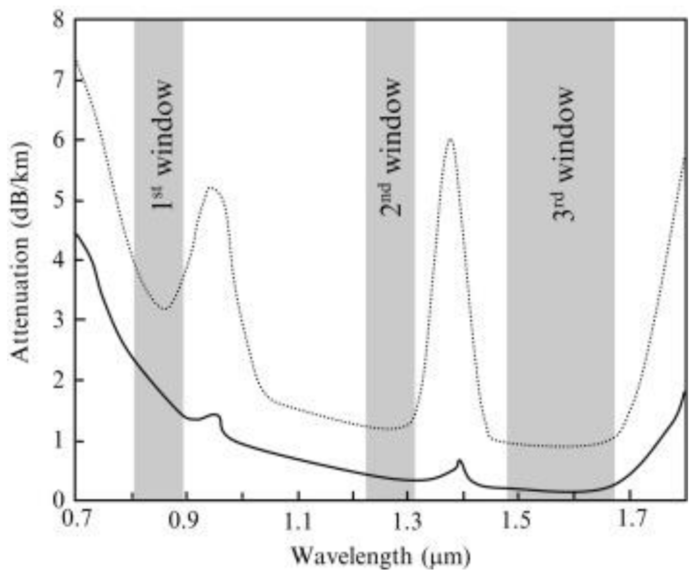

Figure 1.2 Transmission Spectra of old (in dotted line) and new (in solid line) silica fibers. Three low-loss communication windows are shaded. [10]

with free-space wavelength ($\propto 1/\lambda^4$). Moreover, improved fabrication technology for silica fiber governs a heavy reduction in the transmission losses as compared to silica fiber used earlier. The value of Group Velocity Dispersion (GVD) is nearly zero at λ=1310 nm, it is very important from a communication perspective. Despite the advantage of zero group velocity dispersion at 1310 nm, 1550 nm is widely explored and known as the telecommunication window. It is due to the invention of components like EDFA that imparts amplification in a range of 1530-1610 nm and gives an edge to this window, thus 1550 nm is globally accepted as a telecommunication window.

1.2.1 Integrated Silicon Photonics

In the past few decades, Electronic-Photonic Integrated Circuit (EPIC) has emerged as the prominent candidate to get rid of conventional limits of the electronic integrated circuits. Integrated silicon photonics refers to the integration of waveguide and functional devices on the monolithic silicon platform and it offers high EPICs with energy-efficient and cost-effective short-range optical interconnect solutions [11–14]. Silicon photonics does not only improve the behavior of devices at high microwave frequencies but also impart much larger bandwidth as compared to electronic integrated circuits.

Apart from these advantages of silicon phonics, it is also immune to electromagnetic interference (EMI) which is one of the critical issues in the conventional electronic system at high bandwidth operation. EMI typically destroys the electrical signal through neighboring traces also known as crosstalk. It can be simply understood by the decaying phenomenon of electron's electric field which is proportional to the square of the distance (∝1/r2). To clarify this point, assume two parallel metallic lines carrying the signal in the form of voltage. If each line is having thickness and substrate dielectric of 1 µm and 4 respectively and placed at a distance of 1 µm from each other, then 32 % of voltage will be coupled from one line to another at a distance of 5 mm. This is a severe issue, especially where thousands of such lines are integrated within a small area of the order of a few cm^2. On another hand, the electric field component of optical signal decays

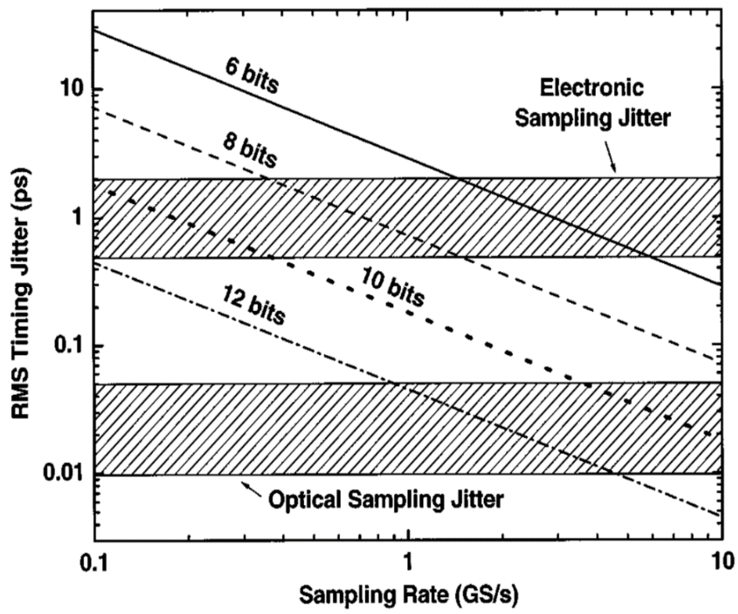

Figure 1.3 Performance dependency of Analog to Digital Converter on aperture jitter when aperture jitter is the only source of the noise. [15]

exponentially with the distance ($\propto e^{-\alpha r}$, where α is the decay coefficient in the cladding region of the optical waveguide). It allows a dense packing of several optical waveguides together with minimal crosstalk. Another advantage of photonics is low-jitter offered by femtosecond mode-locked erbium-doped fiber (Er-fibre) lasers[15,16] which are about two to three times better than electronic-based device as shown in Fig. 1.3.

Silicon is the most popular and widely explored material in the microelectronic industry. Its abundance and low-cost fabrication make silicon an attractive choice for the optoelectronic field where low energy photons (less than bandgap energy) are guided and manipulated using the applied electric field to achieve various functions. Apart from these advantages, Si has high quality in comparison to the other materials like GaAs, InP, Ge, etc. Si has very high thermal conductivity and high optical damage threshold which is about 10 times better than devices based on GaAs. It also attributes high 3rd order nonlinear optical effects like Raman effect and Kerr effect those are several times better than standard fiber [17]. Moreover, silicon-on-insulator (SOI) material offers a high difference in material refractive index (Si-SiO_2) which is advantageous to guiding the signal in a highly compact optical structures to achieve numerous functional devices and promising for better integration of the chip. Silicon

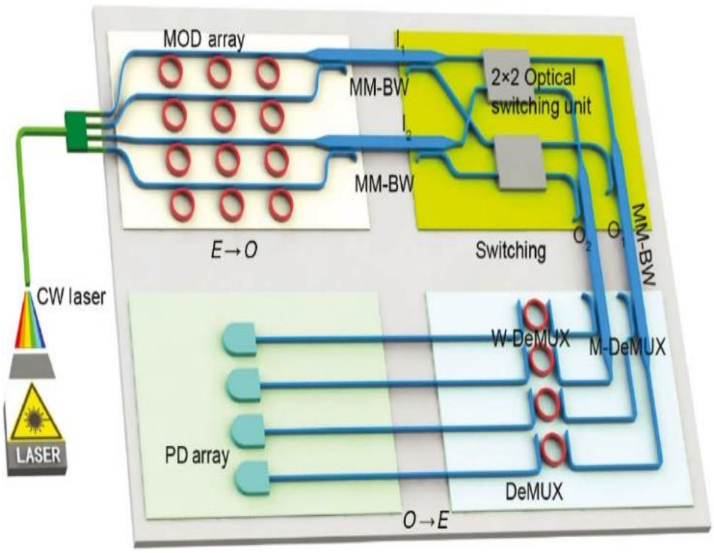

Figure 1.4 WDM-compatible multimode optical switching on-chip system [29]

photonics is not only beneficial to get rid of bottleneck issues of electronic ICs, but also it can be used as a standard highly-dense integrated optoelectronic technology for microwave photonics [18], infrared sensing [19], quantum computing [20], nonlinear optics [21,22], graphene photonics [23,24], transformation optics [25], and many more. These inter-disciplines have shown great potential in the past one decade, For example, in 2013, Massachusetts Institute of Technology (MIT) reported a large-scale array antenna which consists of 4096 units, it consists of a large number of integrated components based on silicon photonic module [26]. It is quite difficult to obtain such a large-scale integration of so many optical units over a monolithic platform. Additionally, researchers are now exploring the capabilities of silicon-based photonics for most advanced quantum communication applications. In the past few years, many groups are working on difficult issues of quantum photonics like quantum entanglement phenomenon and two-photon interference on a silicon photonic chip [27,28]. Thus, we can expect more and more realization of the functional module and complex quantum phenomenon will be implemented on this platform.

The inherent high bandwidth of optical signal compared to a conventional electronic signal allows the loading of a large number of information signals using dense wavelength division multiplexing (DWDM). DWDM is a popular method in the optical communications network which increases the total bandwidth of the system. The same idea is anticipated to be applied in intra-chip for the communication purpose, and in optical analog-to-digital converters[29] as shown in Fig. 1.4. In this figure, an optical link is used to connect all memory elements with the electronic microprocessor in the given intra-chip architecture. The off-chip LASER provides a broad range of wavelength to the various photonic devices. Micro-ring resonators can filter the required wavelength and convert all electronic information into optical form. The optical signal is then processed and can be switched at the desired output destination using optical MUX/De-MUX circuitry. Finally, the optical signal will be converted to a digital signal using an array of the photodetector. This simple example shows the broad view of EPIC, which consists of the number of components like switches, modulator, detector, MUX/De-MUX, sources, filters, etc.

1.3 Overview and design of various optical guiding structures

The fundamental building block of an optical interconnects is the optical waveguide. It offers low loss optical propagation in the optical circuit and connects different components present on the chip. The on-chip optical guidance mechanism in different waveguide structures is mostly based on multiple total internal reflections from the interfaces of the high index material placed in parallel to the optical path of propagation. In this section, we will discuss a distinct optical structure that plays a vital role in the on-chip optical interconnects.

1.3.1 Rectangular dielectric waveguide

It is the most common optical waveguide structure used in numerous device applications. The optical wave propagating in the z-direction of a rectangular waveguide structure can be analyzed according to the scalar wave equation given as

$$\frac{\delta^2 E}{\delta x^2} + \frac{\delta^2 E}{\delta y^2} + [k_0^2 n^2(x,y) - \beta^2]E = 0 \quad (1.1)$$

Where the total number of optical modes are related to V number as

$$V = \frac{2\pi a}{\lambda}\sqrt{(n_{core}^2 - -n_{Clad}^2)} \quad (1.2)$$

Where λ is the operating wavelength, n_{core} and n_{clad} represent the refractive index of core and cladding respectively, a is waveguide core dimension, and β is the phase constant of the optical wave. Depending upon the adopted structure geometry, the rectangular waveguide can be divided into different types like ridge, rib, and slot.

1.3.2 Ridge waveguide

The 3D schematic representation of the silicon photonic ridge waveguide is shown in Fig. 1.5 (a). The ridge waveguide comprises the core of silicon on top of silica-based cladding. To construct functional devices, the waveguide must support only a single mode in the waveguide. To achieve fundamental TE and TM mode, dimensions of the core of the waveguide plays an important role as given in Eq. (ii). When the effective refractive index (n_{eff}) of any optical mode is greater than the cladding index and smaller than the core index, then only it will propagate in the waveguide

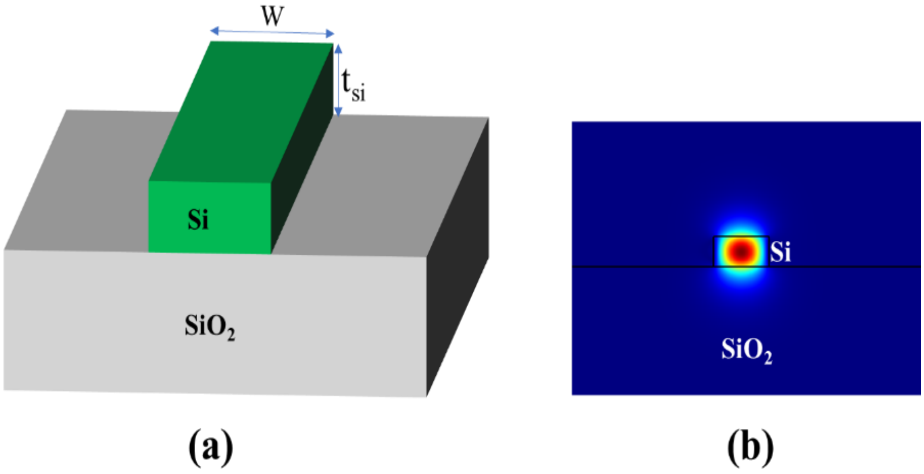

Figure 1.5 (a) Schematic view of Ridge waveguide, w=450nm, t_{si} = 220 nm on top of 2 µm thick SiO_2. (b) Electric field distribution of quasi TE mode in core of Si waveguide.

and mode will not leak out of the waveguide. Confinement of optical mode in the core region will be stronger for the larger value of an effective refractive index.

It should be noted the phase velocity (V_p) of each mode will depend on the value of n_{eff} (V_p=c/n_{eff}), thus all modes travel with the distinct phase velocity in the waveguide. Another important thing is the confinement of mode in the core region, as described earlier mode with the highest value of n_{eff} will have the strongest confinement in the waveguide. As we reach higher-order mode, its n_{eff} becomes weaker and mode starts leaking out of the core region. This phenomenon is important for various applications like sensing, modulation, etc.

1.3.3 Rib waveguide

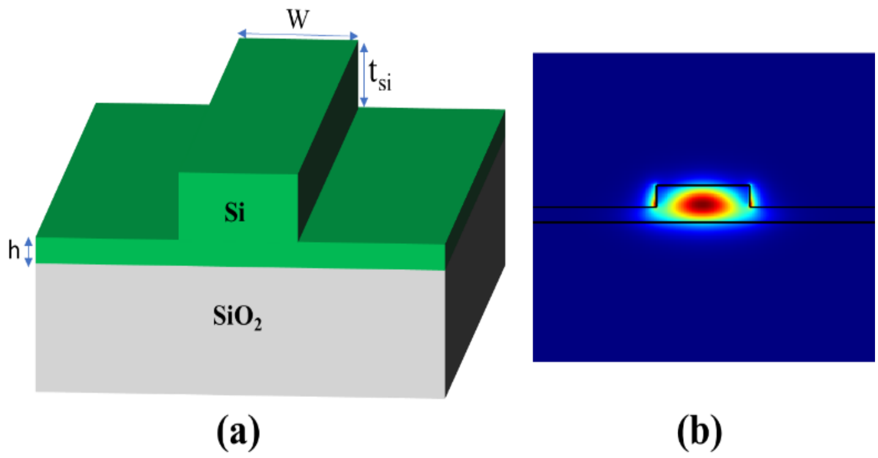

Figure 1.6 (a) Schematic view of Rib waveguide, w=500nm, t_{si} = 220 nm, h = 90nm on top of 2 µm thick SiO_2. (b) Electric field distribution of quasi TE mode in core of Si waveguide.

Fig. 1.6 (a) shows the schematic of the rib waveguide structure. In addition to a simple ridge waveguide structure, it has an extra thin layer below the rectangular strip waveguide. Due to strip loaded geometry, it is not possible to realize single optical mode in rib waveguide. However, it is possible to optimize the rib structure in such that the other mode apart from the fundamental mode will leak out of waveguide at a very short distance and waveguide will remain with fundamental mode only. Rib waveguide structure has a certain advantage over the ridge waveguide like rib waveguide has low loss compare to ridge waveguide. Another advantage is a thin layer below the ridge waveguide offers one more physical dimensions to control the optical signal, for example in case of p-n junction based optical modulator, we provide the electrical contact to that layer (far away from a rib) that isolate the optical signal from lossy metallic contact and ensure the flow of electrical charge. However, one disadvantage of rib waveguide is high bending losses as compared to ridge waveguide.

1.3.4 Slot waveguide

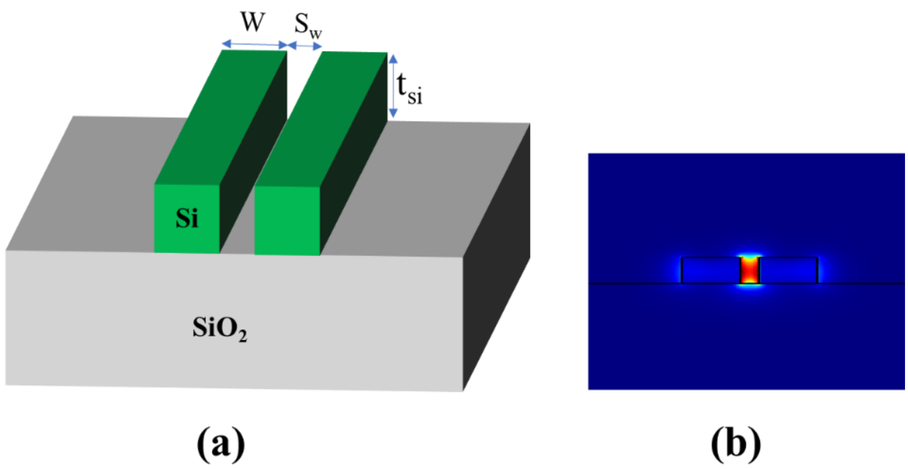

Figure 1.7(a) Schematic view of slot waveguide, w=300 nm, t_{si} = 220 nm, S_w = 100 nm on top of 2 µm thick SiO_2. (b) Electric field distribution of quasi TE mode in the slot region.

In consideration of optimized structure geometry as given in Fig. 1.7 (a), slot waveguides can be formed such that the optical mode carrying very high electric field intensity is confined in the low-index region also known as slot region. It simply can be understood with the electrical boundary condition of the electrical signal at the interface of high index and low index region.

The tangential component of the electric field can be given as

$$E_{t1} = E_{t2} \tag{1.3}$$

Similarly, Normal component of electric field can be written as

$$D_{n1} - D_{n2} = \rho_s \tag{1.4}$$

$D_{n1} - D_{n2} = 0$ for dielectric material ($\sigma = 0$)

$$\epsilon_1 E_{n1} = \epsilon_2 E_{n2} \tag{1.5}$$

Thus, for our case where ϵ_1 and ϵ_2 are the permittivity of silicon and slot region respectively

$$E_{n2} = \frac{\epsilon_1}{\epsilon_2} E_{n1} = \frac{n_{Si}^2}{n_{Slot}^2} E_{n1} \quad (1.6)$$

As given in Eq. 1.6, high discontinuity at the boundary causes a high electric field in the slot region which is proportional to the square of the ratio of refractive indices of the high-index material to the low-index material. Whereas this effect is minimal for the quasi TM mode as the magnetic boundary is continuous at the boundary. The maximum confinement of the optical signal in the slot region can be achieved when the width of the slot region is equal to the decaying component of the electric field across the slot region [30,31]. The key advantage of a slot waveguide is a very high electric field in the slot region which is beneficial for many applications like non-linear optics [32] and sensing [33]. Another advantage of slot structure is the high phase velocity of optical mode (due to low n_{eff}) as compared to the rib/ridge waveguide that offers excellent velocity matching between optical and microwave mode for the high bandwidth application in traveling wave-based modulator [34–36].

1.3.5 Photonic Crystal waveguide

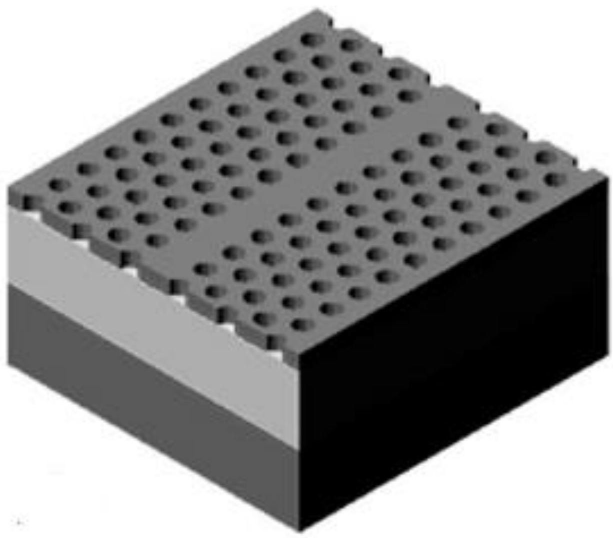

Figure 1.8 A photonic crystal waveguide structure with line defect inserted by removing one array of air holes to guide the optical signal.

The principle of optical guidance in the photonic crystal waveguide is distinct from the conventional total internal based mechanism. Photonic crystal is basically an arrangement of the periodic dielectric structure where a range of “forbidden” frequencies (also known as photonic bandgap) lies in the spectrum.

In such a structure, light is guided when crystal periodicity is disturbed using some defects which causes allowance of some frequencies in the photonic bandgap. For example, if the line defect is properly designed, the resulting guiding mode falls within a photonic bandgap, and light will be highly confined in the defect region. The photonic crystals-based waveguide has numerous advantages over the conventional waveguide. It can be designed such that a slow-light effect can be realized for a certain wavelength, which results in a very strong interaction of light with the matter thus highly compact device can be realized. However, due to the formation of a photonic bandgap, it usually suffers from the narrowband operation. Waveguide made up of photonic crystal can find its application at a variety of places such as nanofluidic tuning, biosensing, RI measurements, optical modulation, etc.

1.3.6 Grating based waveguide structure

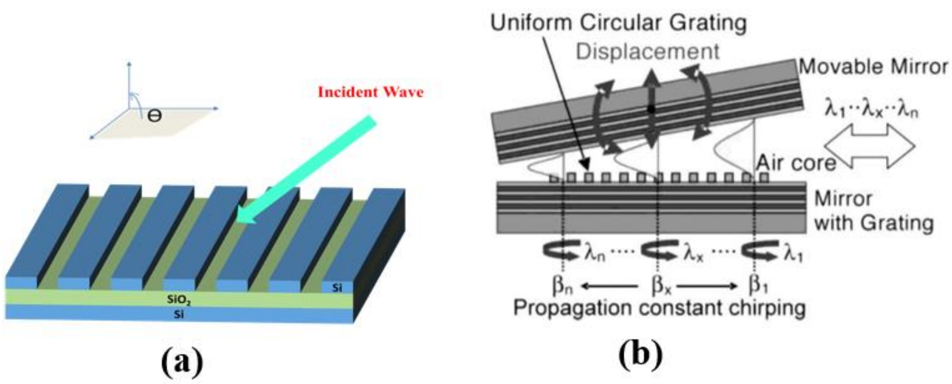

Figure 1.9 (a) Schematic of one-dimensional Si-air grating. (b) Side view of tapered hollow core waveguide, all the layers on top and bottom are quarter wavelength thick [41].

Gating is a periodic structure formed by alternating layers of two different materials having contrast in their refractive indices as shown in Fig. 1.9 (a). It has the capability to reflect the certain wavelength incident on it. One of the examples of grating-based waveguide [37–40] is optical guidance in hollow-core structure[41] as shown in Fig. 1.9 (b). Due to the hollow core of waveguide, it can offer high linearity, negligible thermal dependency, and ultra-low loss characteristics. Researches have extensively used the grating structure in combination with other waveguides like optical fiber, rib waveguide, slot waveguide, etc.

1.4 Electro-Optic Modulator

Rapidly increasing population demanding more and more bandwidth and data-rate which results in network traffic in data communications. It demands cheaper, faster, and more reliable electro-optic modulators and switches. Electro-Optic modulators and switches and are the key components of electro-optic integrated circuits. These devices are used to translate the information contained in the electronic signal into an optical form. It is very hard to modulate light directly from the source because of formation of a cavity in the LASER like distributed feedback (DFB) structure or high contrast gratings (HCG) are usually highly sensitive to external environmental and fabrication error which reduces the reliability of device at high modulation speed. Apart from this, due to indirect bandgap semiconductor material, there is no availability of on-chip silicon laser for EPIC applications [42].

1.5 Performance parameters in plasma dispersion based optical modulator

There are a number of parameters that decide the performance of an optical modulator and some of those are listed as: Modulation efficiency ($V_\pi L$), Insertion loss, Energy consumption, Swing voltage, Modulation bandwidth, Extinction ratio, Modulation Speed, and Footprint area. As most of the parameters are inter-related and have their own trade-off. For this reason, it is not possible to design an optical modulator that has all the merits in the single device. So before designing any modulator, its purpose of the desired outcome must be clear. In this section, we will briefly discuss the performance parameters for plasma dispersion based optical modulator

1.5.1 Modulation efficiency ($V_\pi L$)

In general, modulation efficiency refers to the percentage of total power that carries the information. In the case of a plasma dispersion based optical modulator where a change of the intensity at the modulator's output depends on the change in phase of the optical signal. The maximum change of optical intensity can be achieved when there is a phase shift of π of the optical signal with applying a voltage (typically known as V_π) in an L length of the device. The change in phase of the modulator depends on applying voltage and length of the device simultaneously. One can achieve the desired π phase shift in a short length device with applying high voltage whereas others can achieve the same with low voltage but with relatively longer device length. Due to this reason, the product of both the term i.e. $V_\pi L$ defines the modulation efficiency of such a category of the optical modulator.

1.5.2 Insertion loss

Insertion Loss (IL) accounts for the total loss that appeared in between input power (I_0) to the maximum of the output power (I_{max}) of the device. In the case of plasma dispersion based optical modulator, insertion loss mainly comes through the interaction of optical signal with the doped carriers in the waveguiding region and coupling losses either inside the device (like MZI configuration) and from fiber to device. The mathematical expression for insertion loss cab be given as

$$IL = 10 \log\left(\frac{I_0}{I_{max}}\right) dB \tag{1.7}$$

1.5.3 Energy consumption

Energy consumption per bit (E_{bit}) is usually referred to as drawn energy from the source to charge the electrical equivalent circuit of the modulator. Mathematically it can be expressed as

$$E_{bit} = \frac{1}{4}(CV_{pp})^2 \tag{1.8}$$

Where C and V_{pp} are the capacitance of the device and applied peak to peak voltage, respectively.

1.5.4 Modulation bandwidth

The modulation bandwidth of the optical modulator can be defined as the point where electrical power remains to its half value due to modulate a portion of the optical signal. Fig. 1.10 shows the relation between electrical bandwidth and optical bandwidth when it is plotted as a function of

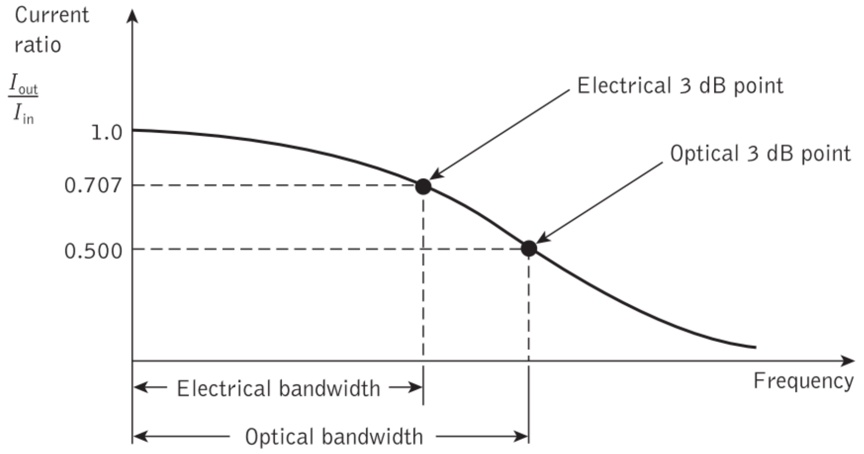

Figure 1.10 Ratio of output to input current as a function of frequency for an optical fiber system. [43]

frequency. Therefore, when electrical power is dropped down by 6 dB, it will be the point where the optical signal will be on its half value (3-dB point).

1.5.5 Extinction ratio

Extinction Ratio (ER) is defined as the maximum depth of intensity at the modulator output with applying a potential. Mathematically it can be expressed as

$$ER = 10\log\left(\frac{I_{max}}{I_{min}}\right) dB \qquad (1.9)$$

Where I_{max} and I_{min} correspond to maximum and minimum intensity level at the modulator output.

1.5.6 Modulation Speed

It is defined as the capability of the modulator at which it can modulate the given bits of signal per unit time. The modulation speed is important parameter in any modulator device and it decides the data-rate transmission capability of the system. In general, modulation speed and extinction ratio are the trade-off quantities which need to be consider carefully while designing the modulator.

1.6 Thesis Outlines

The remaining part of this thesis is arranged in the following way:

In Chapter 2, we explain material based different physical effects for electro-optic tuning that includes Pockels & Kerr Effects, Franz-Keldysh Effect, Quantum Confined Stark effect, Carrier injection effects, and some other effects with a detailed literature review which have been extensively used for manipulation of the light signal with applying an electrical field. In chapter 3, two different grating-based structure is designed and fabricated that can be used to control the path of the optical signal. In the first device structure, a less polarization-dependent broadband reflector is proposed that shows ultra-high reflectivity of >99.99% with the flexibility of shining the light from wider shallow angles. The second device included in the chapter is for off-chip coupling of light from micro-meter size fiber core to nano-mater size silicon waveguide. In order to achieve adequate high coupling efficiency for different cladding materials, various designing parameters of the coupler are optimized using commercially available simulation tool Lumerical-FDTD solution.

In Chapter 4, horizontally aligned p-n junction embedded in the slotted rib structure is presented for high-speed optical modulation using a traveling wave electrode mechanism. This theoretical work explains, how the velocity matching can be improved using the guiding of the optical signal into a low index medium. However moderate modulation efficiency remains an issue in such structure. The problem of moderate modulation efficiency is significantly improved in the next subsequent chapter 5. In this chapter, two electrically isolated vertical p-n junction is formed at each side of the cladding region situated in slot structure. In this device, various performance parameters like modulation efficiency, bandwidth, and insertion loss are investigated for lumped and traveling wave electrodes.

In chapter 6, we proposed the silicon-based comb-like asymmetric grating-based device for tailorable optical characteristics. The device is designed and fabricated with a cavity section introduced between the two grating regions which are deeply etched in the lateral direction to ensure the nonzero coupling of the fundamental and first-order modes in the propagation and counter-propagation direction. The proposed device allows a single narrow passband transmission peak with a large Free Spectral Range (FSR) attributed to the engineered photonic bandgap of two modes present in the waveguide region. However, two different grating periods used at each side of the cavity section increase the fabrication complexity. To ease the fabrication process of the device structure given in chapter 6, a modified device design is proposed in chapter 7. In this chapter, we use the tapered cavity section introduced in between the two sets of grating sections. In the proposed device, parameters for both sets of gratings are kept the same which relaxes the complexity during the fabrication process. The measured optical spectra show a single transmission peak with a wide resonance characteristic at the output. We further investigate the proposed structure to achieve optical modulation using two isolated p-n junctions formed in both the grating sections. Finally, the whole work is concluded in chapter 8. The direction of future research work is also provided in this chapter.

Chapter 2 Optical guidance and modulation in silicon

As discussed in the previous chapter, optical guidance and modulation are crucial because of their important applications. In this chapter, we review the various modulation schemes and the prior arts of silicon-based optical modulators before going through the detailed discussion of the main work. It provides guidance to the proposed designs of silicon-based optical modulators discussed later in this thesis.

2.1 Theory of Electro-Optic Modulator

Electro-optic modulation in different structures and materials have been investigating to achieve electrically controllable optical characteristics. In this section, electro-optic modulation based on various physical effects like Pockels and Kerr effects, Franz-Keldysh effect, Quantum Confined Stark Effect and Plasma Dispersion effect are discussed as follows:

2.1.1 Pockels and Kerr Effects

The electro-optic effects: Pockels and Kerr effect defines the variation in the refractive index of material with applied external potential [43,44]. The dependency of material refractive index (n_r) over the applied field can be described by the summation of linear and higher field-dependent terms as given in below

$$\Delta\left(\frac{1}{n_r^2}\right) = \sum_k r_{ijk}E_k + \sum_{kl} S_{ijkl}E_kE_l + \dots \qquad (2.1)$$

Where electric field components corresponding to different polarization directions are represented by E_k, E_l, it is similar to x, y, and z-direction in the cartesian coordinate system, thus for pockets coefficient for linear electrooptic coefficients are rijk, and Kerr coefficients for quadratic electrooptic coefficients are sijk. Crystals with a lack of inverse symmetry exhibit Pockel's effect like lithium niobite ($LiNbO_3$) and gallium arsenide (GaAs) shows the pockets effect with the coefficient of 3.08×10^{-9} cm.V^{-1} and of 1.6×10^{-10} cm.V^{-1} respectively. Whereas the Kerr effect plays the main role in centrosymmetric materials. Since in both these effects carrier transportation is not involved in the medium, it causes modulators to relay on these effects can achieve high-speed modulation.

Crystalline silicon (c-Si) has an inversion symmetric structure and that is why it does not show any Pockels effect. However quadratic electro-optic Kerr effect exists in the silicon when the electric field of order 10^5 V.cm^{-1} to 10^6 V.cm^{-1} is applied to Si, it causes variation in the refractive index of $\Delta n = -10^{-6}$ to -10^{-4} can be achieved at a wavelength of 1.3 µm (theoretically predicted) [4546]. Beyond this electric field, it is not possible to achieve any change in refractive index due to the dielectric breakdown of silicon near to 4×10^5V.cm^{-1} at carrier concentration of 10^{15} cm^{-3} [47]. To obtain a linear electro-optic effect in silicon, researches are working in direction of intentionally distorted cubit symmetricity of silicon using strain effect [48–50].

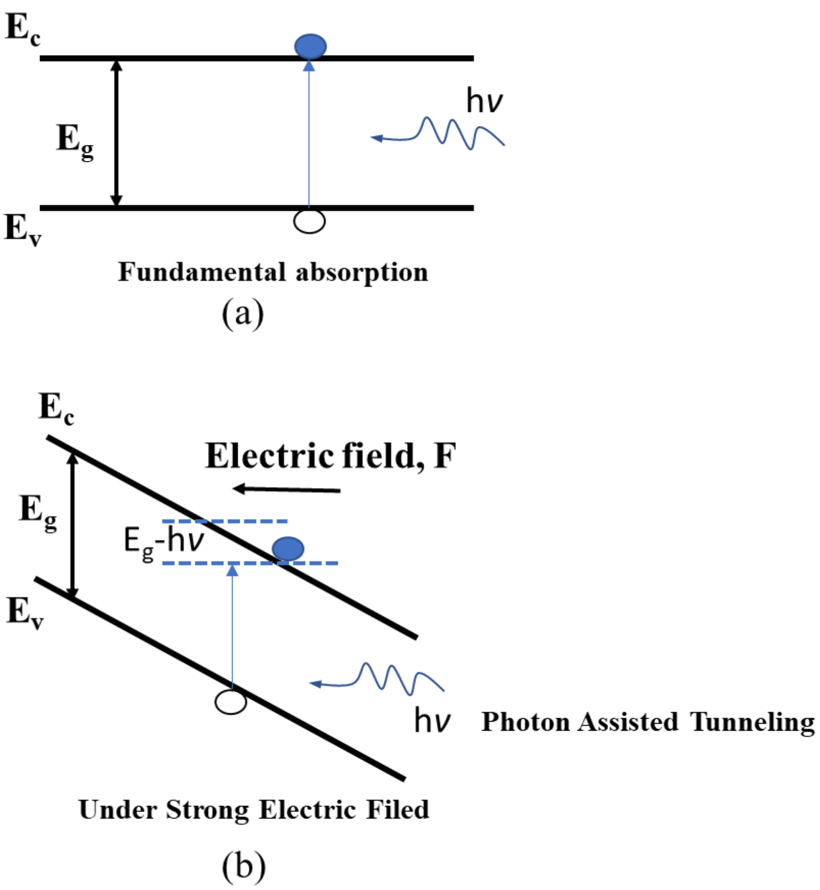

Figure 2.1 Franz-Keldysh Effect (a) Photon Absorption under equilibrium state, (b) Tilting of band and photon assisted tunnelling under influence of strong electric field.

2.1.2 Franz-Keldysh Effect

In direct bandgap bulk semiconductor material, a shift in absorption edge with applying uniform electric field causes sudden variation in the optical loss is known as Franz-Keldysh effect. It is because of the tilting of the energy bands with applying the electric field offer tunneling of electrons in the conduction band (also called photon assisted tunneling). It causes redshift in the absorption spectrum due to the absorption of photons having energy equal to or even less than bandgap energy. As shown in Fig. 2.1 (a), under the thermal equilibrium condition, absorption of a photon of energy hν results in the transition of an electron from the valance band to the conduction band. Fig. 2.1 (b) shows the absorption of photons with energy less than bandgap energy ($E = E_g - h\nu$) due to tilting of the band under strong electric field offers the availability of density of states through tunneling phenomenon by absorbing lower energy photon.

The modulator based on this principle shows a direct change in optical loss and can achieve a high extinction ratio at the modulator output. However, if the incident photon is having energy less than E_g, then change in refractive index is much larger than the change in optical loss thus a modulator can be designed using phase shifter based on the Franz-Keldysh effect. The change in absorption coefficient and material refractive index based on this effect is experimentally

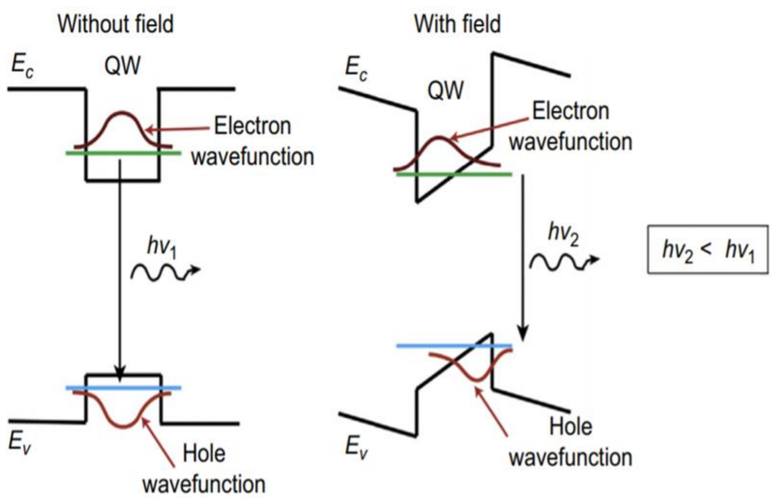

Figure 2.2 Sub-bands and wave-function in potentially restricted Quantum-well structure (a) In thermal equilibrium condition, and (b) in presence of an applied electric field. [48]

measured in silicon [51]. For this, first, the absorption spectra at a wavelength of 1.07 μm are measured, and then using popular Kramers-Kronig relation is used to calculate the change in the refractive index. The change in refractive index is observed that was $\Delta n = +1.3 \times 10^{-5}$ with applied electric field of $E = 0\text{-}10^5$ $V.cm^{-1}$ [51]. In this measurement of change in the refractive index of Si, the value of Δn is primarily due to induced Franz-Keldysh effect and it is because the electro-optic effects produce a very weak change in refractive index $\Delta n = 10^{-6}$ as discussed in the previous section. However, it is also true that the Franz-Keldysh effect is relatively weaker than the plasma dispersion effect in silicon and this is the reason most of the modulators based on Si use plasma dispersion effect.

2.1.3 Quantum Confined Stark Effect (QCSE)

Similar to the Franz-Keldysh Effect in a bulk semiconductor, the QCSE refers to the shift in the absorption spectrum when an external electric field is applied perpendicular to the quantum well structure, as illustrated in Fig. 2.2. In quantum well structure, potentially restricted wavefunction in quantum-confined well structure causes a greater number of available density of states as compared to the bulk semiconductor. The electrostatically bound electron-hole pair in a quantum well correspond to the existence of excitons that offers sharp exitonic peak in QW at low temperature. The electron transition in QW structures can be given by equation [52]

$$hv = E_g + (E_{el} + E_{hl}) - E_{ex} \tag{2.2}$$

where E_g correspond to bulk bandgap energy, E_{ex} is the binding energy of excitons and E_{el}, E_{hl} is zero field energy of electron and hole respectively. The presence of excitons in the structure is not suddenly disassociated even after applying the electric field, it is due to quantum confined wavefunctions of an electron and a hole are compelled to remain in the well. However, electron sub-

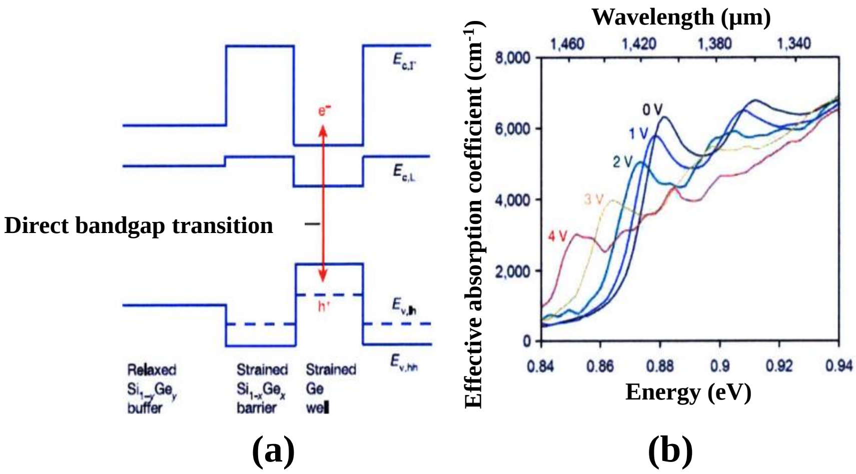

Figure 2.3 (a) Band diagram depicting effect of strained alloy of $Si_{1-x}Ge_x$ and Strained Ge well, (b) Voltage dependent peak shift in effective absorption. [54]

band energy E_{el} reduces whereas the sub-band hole energy E_{hl} increases which lead to a reduction in the overall energy level as $E_{hl}^{el} = E_{el} - E_{hl}$. Resulting in this, the binding energy of exciton E_{ex} also decreases. It causes a redshift of absorption spectra by applying an electric field.

The phenomenon of quantum-confined Stark effect is mostly explored in InGaAs/InAlAs QW structures. It is because it generally has a larger change in refractive index in such QW structures as compared to silicon-based materials. A strong QCSE effect was reported in germanium and silicon-germanium quantum-wells [53,54]. Fig. 2.3 (a) shows the bandgap structure of GeSi/Ge QW whereas measured effective absorption coefficient spectra are shown in Fig. 2.3 (b). The small applied voltage produces a large change in the effective absorption coefficient of 2,800 cm^{-1} at $\lambda = 1.43$ μm under a bias voltage of 3 V. However, structure based on QCSE requires multiple quantum wells to layered and it is also challenging to couple light into the device.

2.1.4 Carrier Injection Effect

The Carrier injection effect is also known as plasma dispersion effect refers to change in material refractive index and optical absorption coefficient when additional free carriers are induced in a semiconductor. Here, first, we mathematically express the plasma dispersion effect as follows [55].

The electron's motion in lattice structures can be written as per Newton's Law,

$$F_{total} = m\frac{dv}{dt} = F_{external} - F_{damping} \tag{2.3}$$

Here total force (F_{total}) experienced by an electron at position r depends on its velocity $v = \frac{dr}{dt}$. The external force exerted by applying electric field E on the electron with charge q can be approximated as $F_{external} = q(E + v\times B) \simeq qE$, the second term can be ignored for v<<c. The damping force $F_{damping}$ is due to resistance for change in the momentum of a band.

$$F_{damping} = \frac{mv}{\tau} \tag{2.4}$$

Where τ is the relaxation time constant. Now, the overall force exerted on an electron can be given as

$$m\frac{dv}{dt} = qE - \frac{mv}{\tau} \tag{2.5}$$

$$qE = m\frac{dv}{dt} + \frac{mv}{\tau} \tag{2.6}$$

Let us consider an exponentially decaying electric field as $E = E_0 e^{-\omega t}$, then velocity of electron can be given as

$$v = \frac{qE}{-i\omega m + m/\tau} \tag{2.7}$$

Now using Maxwell equation

$$\nabla \times H = \frac{\partial D}{\partial t} + J \tag{2.8}$$

$$= -i\omega \in E + Nqv \tag{2.9}$$

$$= -i\omega \in_0 [\in_r + i \in_i - \frac{(\omega_p\tau)^2(\omega\tau)^2 - i\omega\tau}{(\omega\tau)^2(\omega\tau)^2+1}]E \tag{2.10}$$

$$= -i\omega \in_0 \in_r E \tag{2.11}$$

$$\in \equiv (n+ik)^2 = \in_r + \text{i} \in_i - \frac{(\omega_p\tau)^2(\omega\tau)^2 - \text{i}\omega\tau}{(\omega\tau)^2(\omega\tau)^2+1} \tag{2.12}$$

Where ω_p is the plasma frequency $\left(\omega_p = \sqrt{\frac{q^2N}{m\epsilon_0}}\right)$ for an electron with m effective mass, N is the density of the free charge carrier, J is polarization current density, ϵ_r and ϵ_i are the real & imaginary part of relative permittivity ϵ and ϵ_0 is free space permittivity. Now by separating both the real and imaginary part of ϵ we get

$$n^2 - k^2 = \epsilon_r - \frac{(\omega_p\tau)^2}{\omega\tau^2+1} \tag{2.13}$$

$$2nk = \epsilon_i + \frac{(\omega_p\tau)^2}{(\omega\tau)}\frac{1}{(\omega\tau)^2+1} \tag{2.14}$$

The mobility of electron $\mu = q\tau/m$ can be calculated when we setting-down the total force to zero in Eq. (2.5) and (2.7). Substituting $n = n_0 + \Delta n$, $\tau = \mu m/q$ and $k = k_0 + \Delta k$ into Eq. (2.13) and (2.14), we can get expression for change in refractive index and absorption coefficient as

$$\Delta n = -\frac{e^2\lambda^2}{8\pi^2c^2\epsilon_0 n_0}\frac{N}{m} \tag{2.15}$$

$$\Delta\alpha = \frac{4\pi\Delta k}{\lambda} = \frac{e^3\lambda^2}{4\pi^2c^3\epsilon_0 n_0}\frac{N}{m^2\mu} \tag{2.16}$$

Where n>>k, $\tau\ \omega\tau>>1$, and $n_0>>\Delta n$ is considered for infrared frequencies [56]. n_0 and k_0 represent the value of the real and imaginary part of the refractive index in intrinsic condition. When additional free electrons and holes due to external doping are considered Eq. (2.15) and (2.16) can be rewritten as

$$\Delta n = -\frac{e^2\lambda^2}{8\pi^2c^2\epsilon_0 n}\left(\frac{\Delta n_e}{m_e} + \frac{\Delta n_h}{m_h}\right) \tag{2.17}$$

$$\Delta\alpha = \frac{4\pi\Delta k}{\lambda} = \frac{e^3\lambda^2}{4\pi^2c^3\epsilon_0 n}\frac{N}{m^2\mu}\left(\frac{\Delta n_e}{{m_e}^2\mu_e} + \frac{\Delta n_h}{{m_h}^2\mu_h}\right) \tag{2.18}$$

Where Δn_e and Δn_h are the density of free electron and hole, respectively. Mathematical expression for predicting change in refractive index can be derived using experimental electro-absorption data with the help of Kramers-Kronig relation

$$\Delta n(\omega) = \frac{c}{\pi} P \int_0^\infty \frac{\Delta\propto(\omega')d\omega'}{\omega'^2 - \omega^2} = 6.3 \times 10^{-6}\, P \int_0^\infty \frac{\Delta\propto(V')dV'}{V'^2 - V^2} \qquad (2.19)$$

Where c, ω, and V are the speed of light, angular frequency, and energy of the photon, respectively. In 1987, soref et. al. measured electro-absorption as a function of photon energy in heavily doped c-Si and deduce into the simple mathematical function as

When λ = 1.3 µm

$$\Delta n = -6.2 \times 10^{-22} \Delta n_e - 6 \times 10^{-18} \Delta {n_h}^{0.8} \qquad (2.20)$$

$$\Delta \propto = 6 \times 10^{-18} \Delta n_e + 4 \times 10^{-18} \Delta n_h \qquad (2.21)$$

When λ = 1.55 µm

$$\Delta n = -8.8 \times 10^{-22} \Delta n_e - 8.5 \times 10^{-18} \Delta {n_h}^{0.8} \qquad (2.22)$$

$$\Delta \propto = 8.5 \times 10^{-18} \Delta n_e + 6 \times 10^{-18} \Delta n_h \qquad (2.23)$$

It should be noted that the Soref model {Eq. (2.20)-(2.23)} predicts higher change in refractive index due to free holes in comparison with free electrons, whereas according to Drude model {Eq. (2.17)-(2.18)} there is the same level of changes in the refractive index and absorption coefficient for free electrons and holes. Moreover, the Soref model is widely accepted at λ = 1.3 µm and 1.55 µm as it is derived from the experimental data.

2.1.5 Other Effects

Apart from the discussed modulation effect, there some other effects that are promising to realize efficient optical modulation like thermo-optic effect, acousto-optic effect, all-optical modulation effect, and Micro-Electro-Mechanical Systems (MEMS). The thermo-optic coefficient of silicon at room temperature is $dn/dT=1.8\times10^{-4}\ K^{-1}$ which is capable to induce a heavy change in refractive index as compared to the other electrooptic effect like FKE, QCSE, and plasma dispersion effect [57]. In this way, a highly compact device can be achieved by utilizing this effect [58]. The main disadvantage associated with this effect is sluggish modulation response (of ms order) and this is the reason, devices based on this effect only can be used where speed is not the primary concern. Another popular effect in optical modulation is the acousto-optic effect, it induces a change in refractive index by an acoustic wave. In this modulation scheme, the acoustic wave that carries the information signal travel in the waveguide made up of crystal or any polymer that can store the acoustic signal. Due to acoustic signal, there is a periodic variation in the refractive index of the material. When light traveling in the same waveguide interacts with the acoustic signal, due to periodic perturbation induced by an acoustic signal, it also modulates the optical signal accordingly [59]. An all-optical modulator is emerging as a strong candidate as it has the capability to overcome speed limitation induces by electrical circuitry. In such a modulation scheme, a light signal is modulated by the other wavelength light signal (usually known as pump signal). At last, Micro-Electro-Mechanical Systems (MEMS) effect is another category for realizing optical modulators. In this scheme of optical modulation, the moving component of the MEMS system can bring substantial change in the mode profile which in turn can modulate optical loss, polarization, dispersion, etc. However, due to the mechanical moving component (like using piezoelectric material), this effect is very slow and not suitable for high-speed application [60].

2.2 Mach-Zehnder Interferometer (MZI)

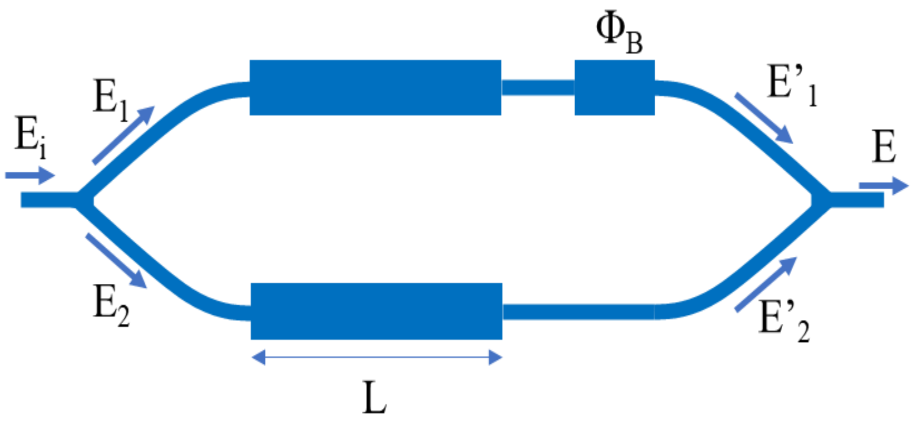

Figure 2.4 The Schematic of optical modulator based on asymmetrical Mach Zehnder interferometer.

The Mach-zehnder interferometer is the most popular configuration that convert phase modulation into intensity modulation. The interference produced at the output arm depends on the relative phase shift between two signals joining at the beam combiner. The basic working principle of MZI is to split the input signal into two parts through the beam splitter and then combined again after some length using beam combiner. Since we know that the intensity of the output signal will depend on the phase at which both the beam will interfere at the combiner. If we somehow modulate the relative phase of the beam at the combiner, the same change will be reflected at the output intensity. In this way phase of the signal can be converted into intensity.

The phase-dependent transmission characteristic of asymmetric MZI can be obtained as follows [61], let us consider the electrical component of the input signal that are having angular frequency ω and is traveling as a function of position (x) and time (t)

$$E_i(x,t) = E_0 e^{-j(kx-\omega t)} \tag{2.24}$$

Where E_0 and k represent the initial intensity of the wave and wavevector, respectively. Now consider the beam is divided into two equal parts E_1 and E_2

Then

$$E_1 = E_2 = \frac{E}{\sqrt{2}} \tag{2.25}$$

Now, the amplitude of the electric field at the end of both the MZI arm can be expressed as

$$E_1' = E_1 e^{-j\emptyset_1 - \alpha L_1} = \frac{1}{\sqrt{2}} E_0 e^{-j\emptyset_1 - \alpha L_1} \tag{2.26}$$

$$E_2' = E_2 e^{-j\emptyset_2 - \alpha L_2} = \frac{1}{\sqrt{2}} E_0 e^{-j\emptyset_2 - \alpha L_2 - j\emptyset_B} \tag{2.27}$$

Here Φ_1 and Φ_2 belong to change in phase in both the arms, whereas αL_1 and αL_2 represent the attenuation of the electric field in both the arms. The extra phase difference in the second arm at the offset point is indicated by the term Φ_B. Therefore the total electric field at the output can be written as

$$E = \frac{1}{\sqrt{2}}(E_1' + E_2') \tag{2.28}$$

Now assume

$\emptyset_{DC} = (\emptyset_1 + \emptyset_2)/2,\ \alpha L = (\alpha L_1 - \alpha L_2)/2, \varDelta\emptyset = \frac{\emptyset_1 - \emptyset_2}{2}$ and $\alpha L_{DC} = (\alpha L_1 + \alpha L_2)/2.$

$$= \frac{1}{\sqrt{2}} E_0 e^{-j\emptyset_{DC} - \alpha L_{DC}} (e^{-j\varDelta\emptyset - \varDelta\alpha L} + e^{j\varDelta\emptyset + \varDelta\alpha L - j\emptyset_B}) \quad (2.29)$$

$$= \frac{1}{\sqrt{2}} E_0 e^{-j\emptyset_{DC} - \alpha L_{DC} - j\emptyset_B/2} (e^{-j\varDelta\emptyset - \varDelta\alpha L + j\emptyset_B/2} + e^{j\varDelta\emptyset + \varDelta\alpha L - j\emptyset_B/2}) \quad (2.30)$$

The normalized transmission expression of the MZI modulator that works in push full configuration can be written as

$$T = \frac{E \times E^*}{E_i \times E_i^*} \quad (2.32)$$

$$= \frac{1}{4} e^{-2\alpha L_{DC}} [e^{2\varDelta\alpha L} + e^{-2\varDelta\alpha L} + 2\cos(2\varDelta\emptyset - \emptyset_B)] \quad (2.33)$$

$$= \frac{1}{2} e^{-2\alpha L_{DC}} [\cosh(2\varDelta\alpha L) + \cos(2\varDelta\emptyset - \emptyset_B)] \quad (2.34)$$

The further simplified mathematical expression can be given as

$$T = e^{-2\alpha L} cos^2(\varDelta\emptyset - \frac{\emptyset_B}{2}) \quad (2.35)$$

The above mathematically expression describes a simple transmission function for asymmetric MZI working in the push-pull mode of operation. It should be noted that the given transmission equation does not include other factors like a loss at splitter and combiner that can influence the transmission characteristics.

2.3 Literature Review:

Now, we will review various photonic components that can be fabricated on a CMOS fabrication platform and plays an important role in the growth of EPIC. Liu et. al. demonstrated the first silicon-based optical modulator using Mach-Zehnder configuration that was operated at large bandwidth in the range of GHz [62]. Recently >100 Gbit/s data rate is reported in an article published by mingbo et. al. that shows compact footprint, low cost, high modulation efficiency, and energy-efficient attributes all in a single device [63]. The photodetector is a key component that converts the optical signal into an electrical signal. Ge-Si based photodetector has been widely explored as it attributes high-performance capabilities like high responsivity and high bandwidth operation [64,65]. The most important things with Ge photodetectors are its CMOS compatible fabrication flow that makes its fabrication possible on the same chip. Laser sources are also an integral part of the communication system. However, due to the indirect bandgap of silicon material, it is not possible to fabricate LASER using Si only. Researchers from Intel demonstrated an on-chip LASER by the bonding of III-V material to silicon waveguide (butt coupled) at a low temperature so that performance of other electronic circuits should not affect adversely [42]. In his work, some other devices which are the imperative part of the photonic integrated circuit like optical filter using a ring resonator, MRR based modulator, and on-chip fiber coupler have been demonstrated on the same chip. All these highly efficient and CMOS compatible photonic structures have made it possible to incorporate photonics and electronics on to the monolithic chip at a low cost.

Among many components of the photonic integrated circuit, the EO modulator are the key device for several optical functions such as high-speed optical interconnects, photonic transceiver, deflector, etc. To date, the light modulation processes can be categorized mainly into three different categories, (i) plasma dispersion effect, (ii) electro-absorption effect, and (iii) other effect. Further discussion is directed mainly into two sections. In the section 2.3.1, we will mainly focus on the plasma dispersion based optical modulator and in the section 2.3.2, other modulation effects than the plasma dispersion effect will be discussed.

2.3.1 Optical Modulators based in plasma dispersion effect

In this paragraph, we will introduce the plasma dispersion effect based on optical modulation. Since it is hard to achieve direct modulation response in c-Si due to centrosymmetric crystal structure [66] that causes absence of any linear EO effect like Pockel's effect and very weak Franz-Keldysh Effect (FKE). The Plasma dispersion effect is the most investigated in the last two decayed due to its fully CMOS compatibility. In 1987, Soref with his colleague demonstrated the change in refractive index (Δn) and absorption coefficient ($\Delta\alpha$) for c-Si with applied electric field [67]. The change in carrier

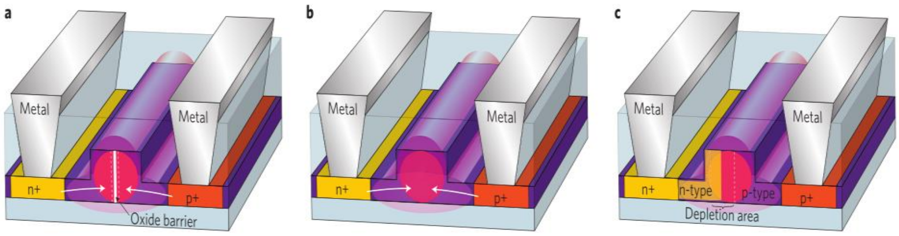

Figure 2.5 3D-view of three kind of structures with different mechanisms, (a) Carrier accumulation structure; (b) carrier injection, (c) carrier depletion mode.[69]

concentration with applied bias modulates the local refractive index of the material that causes variation in the phase of the guided optical wave. As shown in Fig. 2.5, plasma dispersion effect based optical modulator can be categorized mainly into three parts: carrier injection effect, accumulation effect, and depletion effect respectively [68].

The carrier injection type optical modulator is mainly realized with p-i-n junction embedded in the waveguiding region. When the positive bias is supplied to junction through ohmic contact, a large number of electrons and holes will be injected into the intrinsic region, resulting in a change in the real and imaginary part of an effective refractive index. However, the imaginary part that corresponds to optical loss does not show adequate changes that can be used in the direct optical modulation. Therefore, change in the imaginary part of ERI that corresponds to the phase change is utilized to form a modulator using MZI. In the early stage of silicon photonics, an injection type modulator is mainly used. It requires small forward bias and exhibits very high modulation efficiency [69,70] but it suffers from limited modulation bandwidth due to long lifetime of minority carriers and large RC time constant because of large diffusion capacitance at the junction. To improve the dynamic response of the injection type modulator, the pre-emphasis technique was proposed. After this, the number of high-speed devices (in a few Gbit/s) was reported [69,71]. In an accumulation type modulator, a thin layer of the insulating layer (also known as a barrier layer) is formed into a waveguiding region. When the electric field is applied to such a modulator, free carriers accumulate on both sides of the insulating layer. It is similar to the accumulation of carriers in the capacitor. In this category of modulation process, the device is not limited by the lifetime of the minority carrier. Since the change of carrier concentration is primarily across the insulating layer, it is more efficient than an injection type modulator. Intel first demonstrated the optical modulator based on the accumulation type effect that has a bandwidth in the range of GHz [72]. However, complex structural geometry used in the work requires a large number of fabrication processes involved, for example, the oxidation process required to form an insulator layer in the silicon waveguide.

Carrier depletion type modulators are generally based on the reverse bias p-n junction. Similar to the accumulation type modulator, modulation bandwidth in a depletion-based modulator is also not limited by the carrier lifetime effect. The simple structure of this type of modulator includes a p-n junction in the optical waveguiding region, it causes the carrier to interact with the light and increases the effective refractive index (real part) of the optical mode with an increase in reverse bias. The first theoretical modeling of depletion type modulator was presented by Gardes et. al. in 2005 [73]. Later in 2007, Liu et. al. demonstrated a similar type of modulator that exhibits data transmission rate up to 30 Gbit/s [74]. Later, the same group demonstrated the high-speed data rate of 40 Gbit/s in the same structure. After that, the carrier-depletion silicon optical modulator has been widely explored with numerous structural geometries. For example, a Modulator based on a micro-ring resonator is promising for the realization of high-speed operation with a low $V\pi L$ (modulation efficiency) [75,76]. However, a high-temperature sensitivity of the ring resonator is problematic, which causes additional power to compensate for a shift in resonance. Another approach to get an efficient electro-optic modulation is resonant photonic structures [77,78] which in principle, increases the optical group index and exhibits slow light characteristics, resulting in a very low $V\pi L$. The high light-matter interaction in such a structure results in high transmission losses. In 2009, Gardes et. al. demonstrated a ring resonator-based optical modulator operating under depletion mode in an asymmetric p-n diode structure. The measured static extinction ratio of 5 dB is demonstrated at a reverse bias of

10 V, and successfully obtained 3-dB bandwidth of 19 GHz in a highly compact device [79].

In 2010, an idea of improved waveguiding structure based on pipin junction is reported to the obtained best trade-off between optical loss, modulation efficiency, and 3-dB bandwidth [80]. Later the same group demonstrated an optical modulator based on pipin junction with a high extinction ratio of 8.1 dB at 10 Gbps data rate in 2011 [81]. In the same year, Thomson et. al. demonstrated a 40 Gbps data rate using a traveling-wave modulator with a high extinction ratio of 10 dB [82]. In 2012 number of research articles were reported based on depletion type modulators. In this year, Xu et. al. proposed an interleaved junction structure to enhance light material interaction. They reported a high data rate of 40 Gbps with improved modulation efficiency of 1.5-2 V.cm [83]. In order to achieve a low energy consumption device with high-speed operation, Baehr et. al. demonstrated a dual step traveling wave electrode in depletion type modulator which exhibits a data rate of 20 Gbps operating at just 200 fJ/bit [84]. In 2013, Morini et. al. reported 40 Gbps modulation speed in interleaved p-n junction for two different structures i.e. MRR based modulator and MZM[84]. Xiaoguang et. al. showed a 50.1 Gbps data rate in the rib waveguide structure where the p-n junction is a sandwich in between the intrinsic region [85]. In 2014, Timurdogan et. al. claimed the first modulator device that has achieved high-speed operation of 25 Gbps along with ultralow energy of 0.9 pJ/bit using vertical aligned p-n junction structure [86].

In 2015, Zhang et. al. reported, p-n junction embedded in electrically tunable sidewall Bragg grating-based Fabry-Perot filter where two sets of gratings are separated by the cavity section introduced in between them [87]. In 2016, Ding et. al. showed an analysis to enhance the linearity in depletion type optical modulator by doping control mechanism [88]. In 2017, Maegami et. al. reported vertical aligned p-n junction with high modulation efficiency of 0.8-1.86 V.cm at 28 Gbps data-rate. The low value of $V_{\pi}L$ achieved, in this case, is due to the enhanced interaction of optical signal with the vertically aligned junction [89]. In 2018, Yao et. al. demonstrated p-n junction embedded reconfigurable waveguide Bragg grating that has the capability to use as an optical modulator for DWDM application [18]. In the same year, Yong et. al. demonstrated U shaped p-n junction-based device which exhibits extremely high modulation efficiency of 0.46 V.cm at $\lambda = 1.31$ µm. However, the data rate performance is limited to 28 Gbps due to the formation of large capacitance area [90]. In 2019, Deng et. al. a proposed mechanism to achieve pure phase modulation using configurable modulator circuit which is implemented as MZI with a Plasma dispersion modulator and tunable couplers [91].

2.3.2 Other electro-optic modulators

The thermo-optic effect can be utilized to induce a large change in the refractive index even without having much change in an optical loss via heating elements [92,93]. Although modulators/switches based on this effect have several limitations like poor transition time and huge power consumption. The Electro-absorption device shows a sudden change in the absorption spectrum with the application of the electric field, usually, such devices are based on reverse p-i-n configured quantum-confined Stark effect (QCSE) [94–96], or the Franz–Keldysh effect (FKE) [97,98]. The QCSE based EO effect can be observed in quantum well structure when absorption edge shift with applied potential and tilting in-band spectrum causes photon assisted tunneling of the electron, it plays important role in interaction of electrons and photons. Such a device is formed by sandwiching the multiple layers of small bandgap material in between a larger-bandgap material. The biggest issue with QCSE based modulator is the deposition of multiple quantum wells (typically more than 50 periods) and its complicated structure.

In contrast to QCSE based structure, FKE is observed in the bulk semiconductor material. Due to the easy fabrication process and simple structural geometry, FKE based modulators have been widely explored by the researchers. The EO modulation based on FKE in Ge and Si waveguide shows optimum modulation efficiency at 1.6 µm and 1.07 µm respectively [67,99–102]. However, these wavelength ranges are quite far from our desired communication window of 1.55 µm. To achieve efficient optical intensity modulation at telecommunication wavelength i.e. near to 1.55 µm, bandgap engineering is needed. In this context, for the first time Liu et. al. mixed a small fraction of Si (0.75%) with Ge to make waveguide having an apparent bandgap of 0.8 eV and butt-coupled it to silicon waveguide [97]. They reported high 3-dB bandwidth of 50 GHz with an extinction ratio of 10 dB at $\lambda = 1.55$ μm. Afterward, the same group demonstrated optical modulation up to 40 Gbps data-rate with an extinction ratio of 10 dB for a small footprint area of 30 μm^2 only [103]. Mastronardi et. al. reported low power EAM in epitaxially grown Si/SiGe hereto-junction on top of 800 nm thick SOI which exhibits a high data rate of 56 Gbps with an extinction ratio of 5.2 dB at $\lambda = 1.566$ μm [104].

Apart from fully CMOS compatible structures, there are several reports in a hybrid silicon-based modulator structure. To achieve efficient modulation at desired telecommunication wavelength, graphene has been widely used in combination with silicon due to its extraordinary properties, especially in the electronic and optical regime. When single-layer carbon atoms are strongly connected using σ bond in a hexagonal arrangement, it forms a graphene layer. The ultrahigh carrier mobility of 200,000 $cm^2/(V.s)$ at room temperature makes it unprecedented for high-speed applications [105]. Moreover, graphene also shows a wide optical spectrum due to constant absorption of $\pi\alpha = \approx 2.29\%$ ranges from visible to infrared wavelength spectrum where $\alpha^2 = e^2/(\hbar c)$ [106]. Electronically controlled light manipulation in the graphene is possible with sp^2 hybridization of carbon atoms. In the unique electronic structure of graphene, the conduction band and valance band meet like a two cone at its sharp edge as shown in Fig. 2.6 [107,108].

The optical modulation of graphene is mainly achieved by controlling chemical potential μ (Fermi level E_F) by applying a voltage on electrical gating. In 2016, Hamed et. al. demonstrated athermal and broadband optical modulation using a double-layer graphene structure where high-speed data rate up to 35 GHz was demonstrated for a wide temperature range of 25-145°C [109]. In most of the structures based on graphene, TM mode is preferred over TE mode due to the better modulation depth of ≈ 0.1 dB/μm. However, given modulation depth is not good enough when highly compact devices are needed. To get rid of this issue, Bloch modes supported by plasmonic waveguide is used such that it shows the improved modulation depth of 4 dB/μm at 1.65 μm wavelength [110]. Despite all given extraordinary properties, fabrication of a single atomic thick graphene layer is difficult to achieve, and if somehow bi-atomic thick graphene layer is deposited, it will behave differently compared to a single atomic thick layer. Another issue with the graphene-based optical modulator is its non-combability with the CMOS fabrication flow which makes it

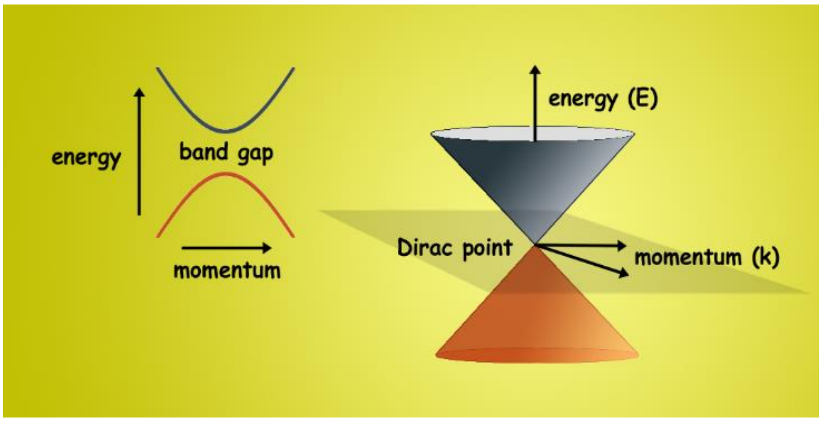

Figure 2.6 The band structure shown in left with parabola shape is for three-dimensional ordinary semiconductor material, bandgap energy lies in between the Ec (lower energy level of conduction band) and Ev (higher energy level of valance band). The band structure of two-dimensional graphene is given in the right side, it shows smooth-sided cones that joins at the Dirac point.[23]

inadmissible for an integrated photonic circuit.

Hybrid silicon optical modulator based on the electro-optic polymer is emerging as a new class of devices. In such devices, electro-optic activity mainly depends on the non-linearity coefficient (r_{33}) of the material. Polymer-based optical modulators have two key benefits over the convention silicon-based devices, one of them is the very fast E-O response and another is the negligible velocity mismatch between the optical and RF modes. The dependency of velocity mismatch on modulation bandwidth (f) can be given as follows [111,112],

$$f_{3\,dB,max} \propto \frac{c}{4(n_m - n_o)}\ (GHz) \tag{2.36}$$

where n_m and n_0 represent the microwave effective index and optical group index of the RF mode and optical mode, respectively. As given in eq. (2.36), if the mismatch between these two indices is nearly zero, it results in the ultra-high bandwidth that can be achieved ideally. However, it is not only the factor which limits the bandwidth of the modulator, some other factors like microwave loss, interaction length, impedance mismatch also responsible for limited bandwidth. The conventional inorganic materials like $LiNbO_3$, $LiTaO_3$, $KNbO_3$, etc. are not capable to overcome such issues found in the EO modulator. The low voltage required to achieve the phase shift of π is another key advantage of the polymer-based EO modulator, it is due to very high nonlinear coefficient of the EO polymers (that can be more than 2000 pm V^{-1}) [113] which inversely depends on the half-wave voltage: $V_\pi = \frac{\lambda h}{n_0^3 \gamma_{33} L}$. The first EO polymer used for EO modulation was 4-dimethylamino4'-nitrostilbene (DANS), it showed the small Non-linear coefficient of 6.1 pm V^{-1} at $\lambda = 1310$ nm [114]. In 1994, an electro-optic polymer-based modulator demonstrated by Chen et. al. shows 3-dB bandwidth of more than 100 GHz can be obtained using poled PUR-DR19 as active core and Epoxylite 9653 as the cladding material.

The polymer-based EO modulator discussed till now was designed as a multi-layer structure. In these structures, cladding material is chosen such that most of the optical power is confined in the core region. To control the excess optical loss and to improve insertion loss, electrical contact like metal or Indium Tin-Oxide are placed in such a way that it should not have any contact with the optical signal traveling in the core region. However, it will limit the modulation efficiency (V_π L) of the device. To improve the $V_\pi L$ and to make CMOS compatible structure, a slot-based structure in the silicon was proposed. It resolves the issue of cladding material and the high electric field can be generated in the slot region due to the discontinuity of the normal component of the electric field in the slot region. It causes strong optical power confined in the small area [36,115]. The first slot-based silicon-polymer hybrid modulator attributing 100 GHz 3-dB bandwidth was demonstrated by the Alloatti et. al. in 2014. They showed a modulation efficiency of 1.1 V.cm using the non-linear polymer (M3) with $r_{33} = 18$ pm/V [36]. In 2018, Clemens et. al. demonstrated ultra-high modulation efficiency of only 0.032 V.cm using EO chromophore JRD1 [113]. Apart from all these advantages, a polymer based EO modulator severely suffers from various issues like thermal instability, high transmission losses, deterioration with time, and high-temperature sensitivity which need further development in such kinds of modulators.

Chapter 3 Silicon-based grating structures for integrated photonic devices

The grating is a periodic perturbation of material index often in either one or two directions. Optical gratings are the most basic building blocks in the optics. Gratings can be broadly diversified into three different categories: the diffraction regime, deep-subwavelength regime, and near-subwavelength regime (also known as a subwavelength regime). In the diffraction regime, the period of the grating is greater than the wavelength of the incident optical signal, whereas in deep-subwavelength regime the grating period is much less than the incident wavelength [116,117]. Among these two regimes, if the grating period is in between the wavelengths inside the grating material and its surrounding media is called near the subwavelength regime. Many extraordinary features can be achieved by covering the high-index grating material with the low-index medium. For example, one can design the grating to achieve extremely high reflectivity (>99.9%) whereas it also can be designed to obtain very high-quality-factor ($Q > 10^6$) by choosing the appropriate grating parameters [40,118–120]. In the past few decades, gratings engraved on silicon have been promising due to its unique optical characteristics and easy fabrication process that are fully compatible with matured CMOS platform. There is a long list of applications that can be realized with the grating structures such as high reflective mirror, optical filtering, off-chip coupling, sensing, etc. In this chapter, we have discussed designed, fabricated, and characterized mainly two grating structures which are off-chip grating coupler and highly reflective broadband mirror for on-chip applications. The same off-chip grating coupler designed and fabricated in this chapter is also been used with other devices as discussed in chapters 6 and 7.

3.1 Subwavelength grating coupler for off-chip fiber coupling

There are two major challenges in the efficient coupling of light from optical fiber to Si waveguide. One challenge is the mode mismatch between micro-meter size fiber core to a few hundred nano-meter sizes Si waveguide, whereas another challenge is due to large index mismatch between low index silica fiber

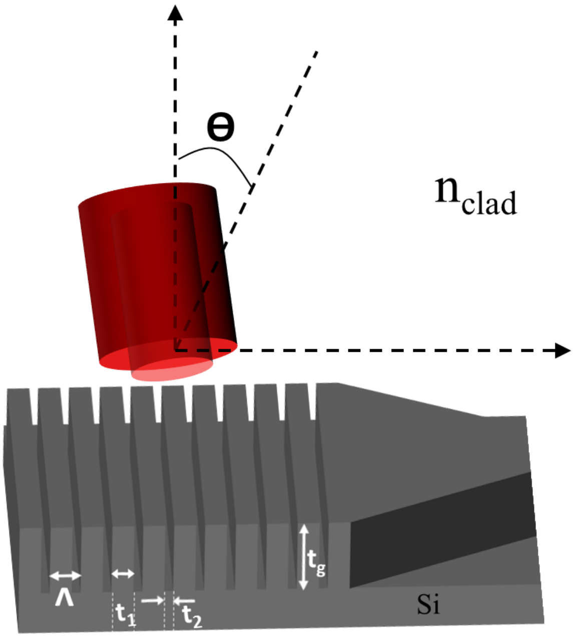

Figure 3.1 3D-schematic of grating coupler (in grey color) with tapered rib geometry (at the right) to scale down the optical mode at nano scale. The figure in red color shows the fiber with its core and cladding, the fiber is θ degree tilted with respect to vertical direction.

and high index Si waveguide. If we couple of lights directly from fiber to Si waveguide, it will result in high coupling loss which increases the insertion loss undesirably. To get rid of these issues, a number of research groups have demonstrated a polymer cladded inverted taper structure that exhibits a coupling loss of less than 2 dB [121,122]. The problem with the inverse-tapered structure is placing a device that must be at the edge of the wafer. Coupler based on grating structure offers the flexibility of device positioning anywhere on the chip and it does not require any edge polishing as well. There are a number of reports that shows different kind of coupler design for efficient coupling of light into the device [123–125]. The grating coupler used in this work is similar to the previously reported work [126,127]. However, its parameters are optimized in such a way that it efficiently couples light in presence of different cladding material surrounding to the device like air, water, and SiO_2.

3.1.1 Coupler design and Efficiency optimization

The schematic of the grating coupler is shown in Fig. 3.1. The grating Coupler is designed and simulated on a 220 nm thick SOI wafer. A fixed number of rectangular grating teeth arranged in the periodic form with connected spot size converting tapered geometry is used in the coupler design. Initially, the grating period (Λ) is kept at $\Lambda = \lambda/n_{eff}$ for off-chip coupling from fiber to chip, where λ and n_{eff} are operating wavelength and effective refractive index (ERI) of the optical mode, respectively. Apart from the grating parameters, there are a number of factors that need to be considered for efficient coupling of light at the desired wavelength such as cladding material and angle of incidence. For example, in the case of the vertically incident optical signal on gratings, the coupler will produce second-order diffraction and thus light will reflect into the waveguide. To avoid this undesirable second-order diffraction, incident light is coupled to grating at a small angle from the vertical direction. First, we will discuss the optimization for grating device dimensions followed by the fabrication and measurement process.

To calculate the maximum coupling efficiency, optimization of the grating period (Λ), duty cycle (DC) ($\eta = \frac{t_1}{t_1+t_2}$) and etch depth ($t_g$) is done by considering the SiO_2 as a top cladding material and angle of incidence (θ) is fixed at 10°. Device simulation is performed using the commercially available simulation package “Lumerical” [46]. The 3D Finite Difference Time Domain (FDTD) method is used for the simulation that mimics the practical device behavior. However, for the fast calculations, initially, we have used a 2.5D FDTD method for the optimization which gives a better approximation of the various device parameters. The auto nonuniform mesh of 0.25 nm step is used in the simulation to provide the high accuracy of results with less computational time and memory. The device is surrounded by a PML (Perfectly Matched Layer) boundary condition that allows the absorption of optical waves with minimal reflections.

First, the optimum position of the fiber over the input grating coupler is simulated with initial grating parameters that do not require optimized grating parameters. The average transmission (T_{net}) is calculated over the wavelength

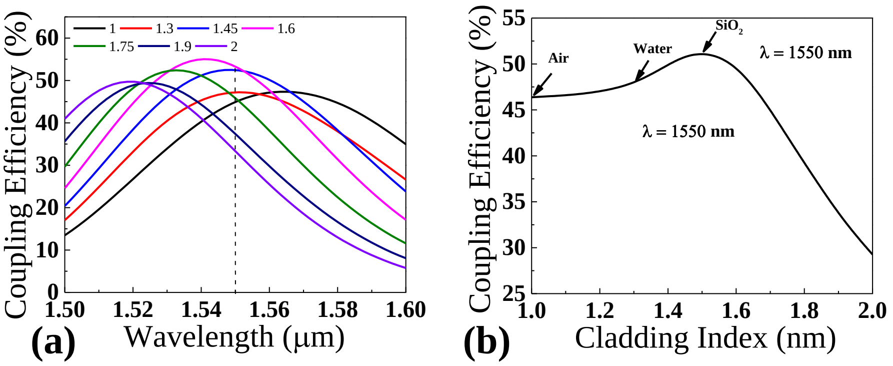

Figure 3.2 (a) Coupling efficiency in presence of varying cladding index from 1 to 2, vertical dashed line represents the scale at telecommunication wavelength. (b) Coupling efficiency as a function of cladding index at λ = 1.55 µm.

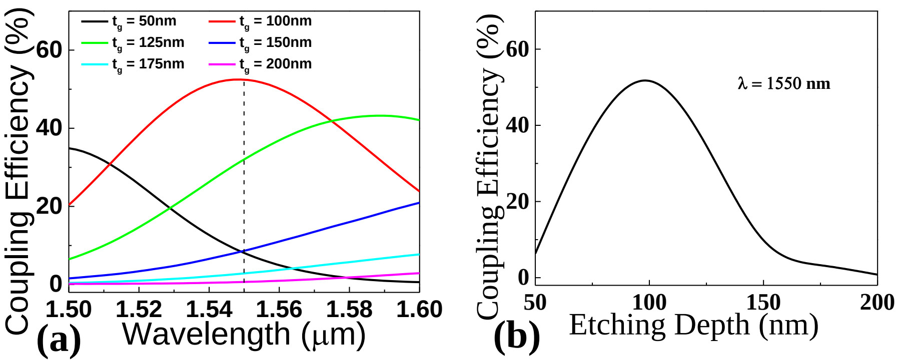

Figure 3.3 (a) Coupling efficiency with varying Etching depth from 50 nm to 200 nm, vertical dashed line represents the scale at telecommunication wavelength. (b) Coupling efficiency as a function of etching depth at λ = 1.55 µm.

range of 1.5 µm to 1.6 µm to find the best coupling efficiency at the telecommunication wavelength of 1.55 µm. A particle swarm algorithm with a maximum generation rate of 40 is used to optimize all three grating parameters: Λ, η and t_g. The optimized value of coupling efficiency is 52.5% with grating parameters as follows Λ = 0.66 µm, η = 61% and t_g = 100 nm.

In order to analyze the device behavior with different cladding material, simulation is performed for varying cladding refractive indices (n_c) as plotted in Fig. 3.2, it shows that coupler can be used with different cladding material but with compromised coupling efficiency. Coupling of light with different cladding material is important especially when such coupler is used to feed the device that can have different analytes on its top. We have also

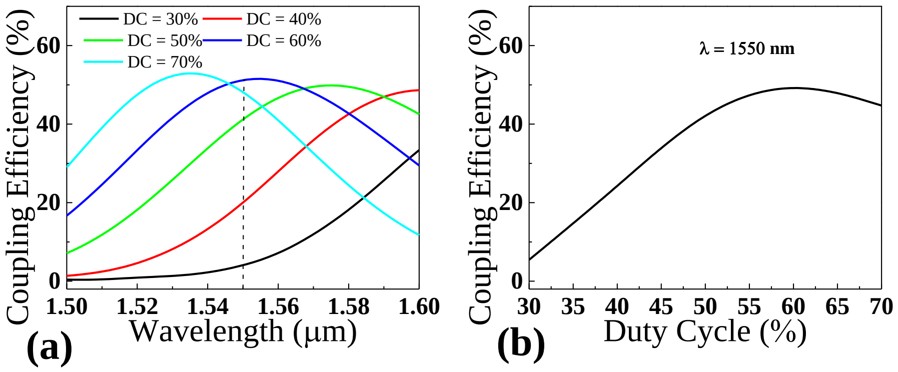

Figure 3.4 (a) Coupling efficiency with varying Duty Cycle from 30% to 70%, vertical dashed line represents the scale at telecommunication wavelength. (b) Coupling efficiency as a function of duty cycle at λ = 1.55 µm.

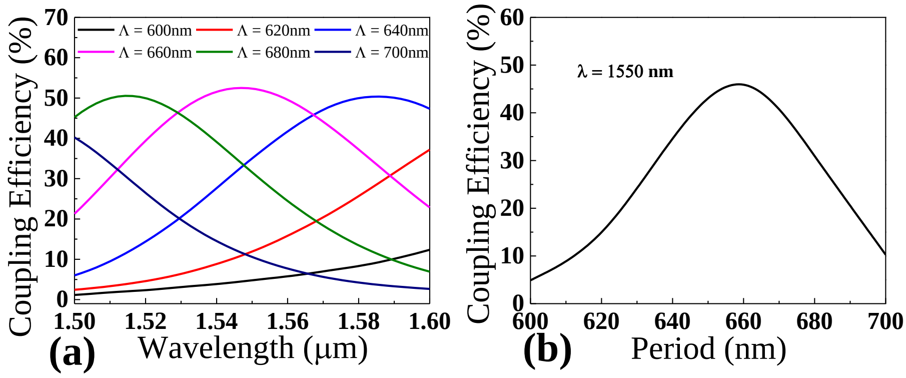

Figure 3.5 (a) Coupling efficiency with varying grating period from 30% to 70%, vertical dashed line represents the scale at telecommunication wavelength. (b) Coupling efficiency as a function of duty cycle at λ = 1.55 µm.

calculated the coupling efficiency with varying grating parameters that gives a better estimation of fabrication tolerance of grating coupler. Fig. 3.3 (a) shows the variation in etching depth over the optimized period and duty cycle which is fixed during the calculations. It gives an idea of the coupling efficiency when the device is opted to some other etching depth or to analyze the fabrication tolerance behavior of the device**.** As we know the designed coupler is intended to have the best performance at telecommunication wavelength. Therefore Fig. 3.3 (b) represents the coupling efficiency for different etching depth at a fixed wavelength of 1.55 µm, which proves that the best efficiency can be obtained when opted at t_g = 100 nm. It gives a tolerance value of ≈65 nm from the optimized depth where coupling efficiency will remain half of its peak value. Then after computation is performed by sweeping the duty cycle from

30% to 70%. It shows a blue shift in the transmission spectrum with an increase in the duty cycle as plotted in Fig. 3.4 (a). The coupling efficiency plotted in Fig. 3.4 (b) indicates that a higher value of duty cycle exhibits better tolerance as compared to the lower value of the duty cycle from the optimized value. Finally, the coupling efficiency analysis for the varying grating period is done by sweeping the period from 0.6 µm to 0.7 µm. It shows the redshift of transmission spectra as given in fig. 3.5 (a), and then coupling efficiency at 1.55 µm is plotted in Fig. 3.5 (b). The tolerable variation in the grating period is near to 66 nm for having at least 3 dB coupling efficiency at the output from its maximum value.

3.1.2 Fabrication

In this section, we include the detailed fabrication process of the designed grating coupler which is divided into following steps:

3.1.2.1 Cleaning of sample

The sample of ~ 2 cm × 2 cm was first cleaved out of a wafer and then it was sonicated in isopropyl alcohol (IPA) for 10 min followed by the nitrogen plunge. Dry sample was dip inside piranha solution (H_2SO_4:H_2O_2::1:3) to remove any organic traces from the surface. Then the sample was dip inside hydrofluoric acid (HF) for 20 sec to remove the native silicon dioxide layer. The sample was cleaned and ready for further fabrication processes. The partial fabrication work of resist Coating and Lithography process is performed under Nanoscale Research Facility at the Indian Institute of Technology Delhi.

3.1.2.2 Spin coating of electron beam resist

The cleaned sample is ready for the lithography process. The thin layer of negative tone HSQ resist was spin-coated on the top Si surface in the 2 steps:

Table 1 Coating parameters for layering 80 nm of HSQ resist on Si

Step	**Time**	**Acceleration**	**Speed**
1	10 sec	100 rpm/sec	500 rpm
2	45 sec	1500 rpm/sec	4500 rpm

3.1.2.3 Electron Beam Lithography

The spin-coated sample was first prebaked for 1 min 30 sec at 180°C for making uniform resist over the silicon surface. Then, Electron beam exposure using Raith pattering system was used to pattern the grating coupler. The EBL writing was performed at aperture size of 10 µm, Voltage:10 KV, Beam Current: 23.04 pA, and Area Does: 360 µC/cm^2, After patterning the resist, 4 min development process followed by the rinse in DI water removes the unexposed soft resist from the sample surface. The SEM view of the developed sample is shown in Fig. 3.6 (b).

3.1.2.4 Etching

The open silicon surface was etched using Advanced Vacuum's Vision 320 RIE system. The etching depth up to ~ 100 nm is achieved using fluorine-based chemistry where the following parameters are used for the etching process: chamber pressure- 15 mT, flow rate- SF_6 : CHF_3 :: 6 sccm : 20 sccm, plasma power- 1000 W, operating temperature - 18° C, and forward power - 30 W. The microscopic view and SEM view of an etched sample are shown in Fig. 3.6 (a) and (c) respectively.

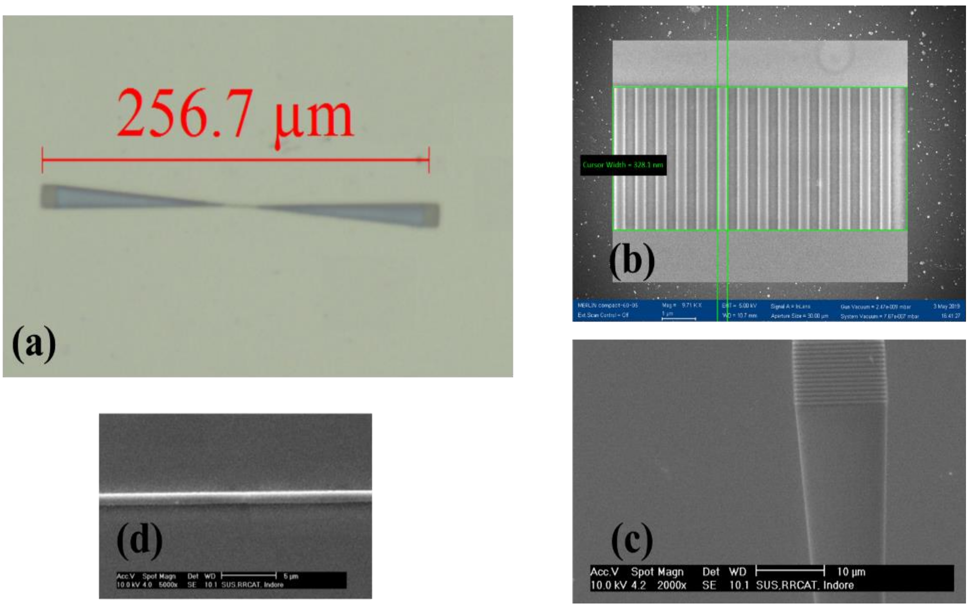

Figure 3.6 (a) Microscopic view of fabricated coupler, 22 pair of gratings on both side of 100 µm long tapered section. (b) The 5 µm wide and 50 µm long rib connects both side of coupler, (c) SEM view of coupler teeth after development process, (d) SEM view after dry etching process using fluorine-based chemistry.

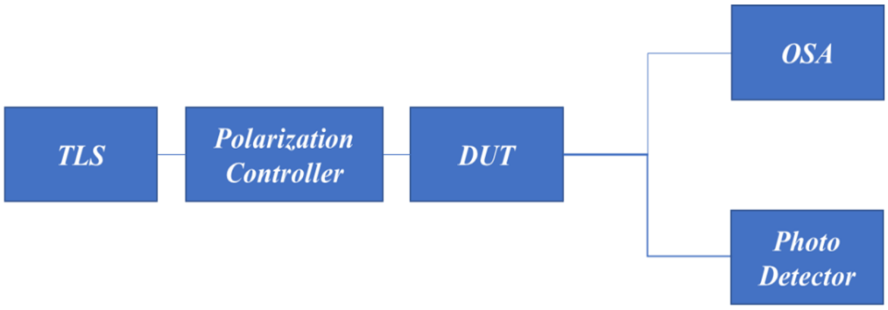

Figure 3.7 Block diagram representation of experimental setup used for optical measurement.

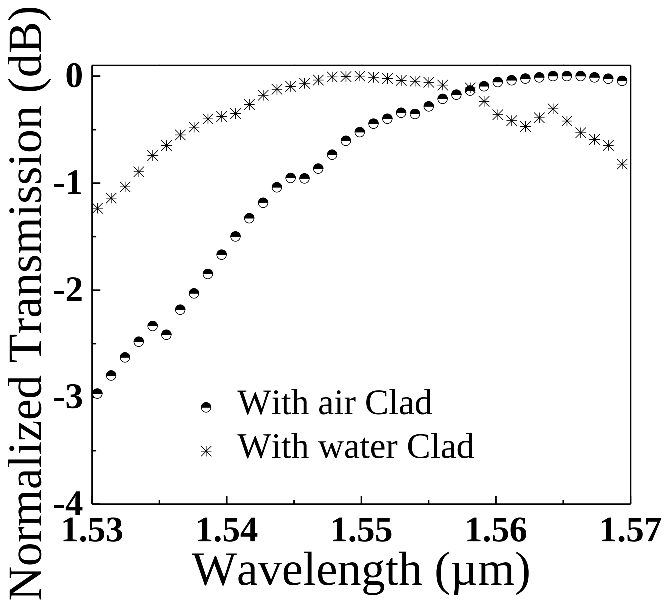

Figure 3.8 Measured normalized optical transmission characteristics under two different cladding on the top i.e. air and water.

3.1.3 Experimental setup and measurement

the Experimental setup for characterizing the fabricated grating coupler is shown in Fig. 3.7. A system controlled Tunable Laser Source (TLS) (Make: keysight, Model: N7711A) with Optical Spectrum Analyzer (OSA) (Make: Anritsu, Model: MS9740A) is used for the optical measurement. The output light from the TLS (1530 nm < λ_0 < 1570 nm, Power - 30 mW) is first set to have maximum current at the photodiode when light is passed through the polarization controller (set to pass only TE mode). However, it should be noted that the coupler is designed to support only TE mode thus previous steps can be avoided during the measurement process. Now, the light is fed to input grating coupler at a 10° angle with respect to the surface normal direction. This 10° angle is fixed by the 3D printed piece of plastic material with no sharp corners. The output light is collected through signal mode bare fiber at the second set of gratings which is further connected to OSA for analyzing the optical spectrum. The measured optical characteristics for two different cladding materials are shown in Fig. 3.8. The 40 sampled data point is observed in the range of 1.53 µm to 1.57 µm, which is the maximum possible range with available OSA. This graph shows the broadband spectral characteristics for both the cladding i.e. air and water. As expected from the simulation, the peak of the transmission for air cladded grating is centered near to 1.563 µm whereas for water cladded grating exhibit transmission peak near to 1.551 µm. Here it should be noted that the spectral response due to 100 µm long rib will be nearly linear for the given coupler thus the spectral response is only due to the coupling of light in both the set of gratings of the coupler. The given coupler has been realized with other devices discussed in chapters 6 and 7.

3.2 Broadband Reflector for on-chip photonic devices

A High-Contrast Grating (HCG) in the sub-wavelength regime has opened new avenues for a variety of applications including VCSEL, Beam steering, grating coupler, hollow-core waveguide, etc. [37,41,119]. With an outstanding property of HCGs, it can be used as a highly reflective mirror in optical waveguides. In this work, HCG of Si-Air in the subwavelength regime is designed that exhibits high reflectivity (>99%) for both TE and TM modes in a broad range of wavelengths from 1.41 µm to 1.7 µm. Hollow-core waveguide made up of these highly reflective mirrors is designed such that it efficiently guides the optical signals lies in the hollow core region. Due to the highly reflective nature of the designed mirror, the proposed waveguide shows ultra-low loss optical characteristics. The proposed device also shows a high value of numerical aperture as it offers a high degree of freedom for light incident at wider shallow angles in the hollow core-region of the waveguide. The proposed device is fully compatible with existing CMOS fabrication technology. This broadband reflector type hollow-core waveguide has the potential to function as a basic module in the number of on-chip integrated photonic circuits that enables many applications in optical fiber communications, optical interconnects, delay lines, and optical sensors.

3.2.1 Reflector design, fabrication and theoretical analysis

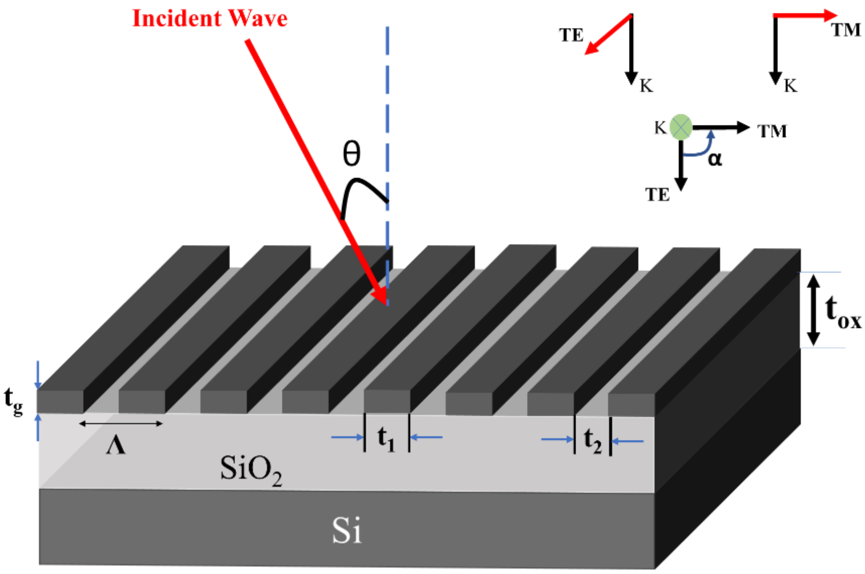

Figure 3.9 Schematic of broadband reflector based on Si-air grating on top of SOI, the arrow shows the incident wave on the gratings at an angle Θ. Figure in right side shows the polarization direction for transverse electric and magnetic field with associated wave direction k. Symbol α defines the polarization states for the mode; α = 0 for pure TE wave and α = 90 for pure TM. The optimized parameters are Λ = 700 nm, DC = 50%, t_g = 658 nm and t_{ox} = 1 µm.

The schematic of the broadband reflector is shown in Fig. 3.9. The reflector is designed as Si-air HCGs on top of SOI that work as a high reflective mirror for a broad range of wavelength and offers the flexibility of shining light from wider shallow angles. The fabrication of the designed reflector starts with the deposition of a 50-80 nm thin chromium layer over the cleaned Si surface. For this, DC sputtering with a highly pure Cr target (99.99% pure) is used where sputtering is performed at 70 mA current for 1 min. In the next step, ≈a 100 nm thin layer of 1% PMMA (in anisole) is spin-coated in the following two steps: (i) speed: 500 rpm, acceleration: 100

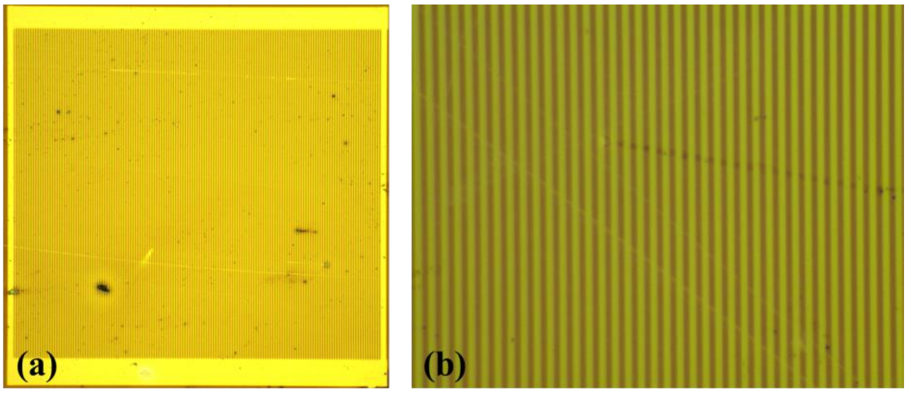

Figure 3.10 (a) Microscopic view of grating after the development process. The yellow colour in the figure is Cr and centre dark colour in the grating is PMMA (b) microscopic image after the Cr etch, silicon surface is shown by light yellow strips whereas brown colour represents the PMMA.

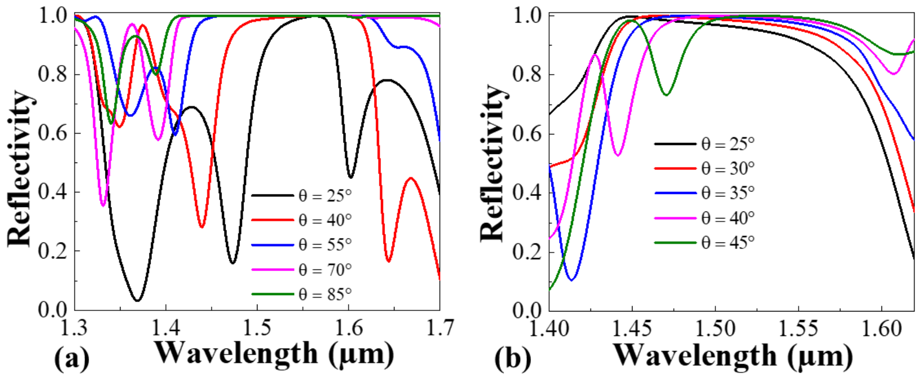

Figure 3.11 Reflectivity as a function of wavelength for (a) TE mode (α = 0°) (b) and TM mode (α = 90°).The width of the reflectance spectra for TE mode increases for larger values of incidence angles with respect to vertical axis, whereas it decreases for TM mode.

rpm/sec, time: 10 sec. (ii) speed: 5000 rpm, acceleration: 700 rpm/sec, time: 50 sec. The coated sample is pre-backed on a hot plate for 30 min at 180°C. Then, EBL is performed at an aperture of 30 μm with an accelerating voltage and beam current of 30KV and 0.38 nA respectively. The optimized area does is 180μC/cm^2 that governs beam speed of 6.6 mm/sec. In the next step, the sample is developed for 55 sec in a solution of MIBK:IPA::1:5 followed by the gentle rinse of the sample in IPA. Till now, the pattern of PMMA is transferred over the Cr layer on the sample. Then, Cr is etched in NaOH:$K_4Fe(CN)_6$::1:3 solution for 3 min. It removes the chromium from the open surface and finally sample is cleaned with the acetone to have grating of Cr over the Si sample. The microscopic image of the sample is shown in Fig. 3.10. Finally, RIE is performed with the following parameters: chamber pressure- 15 mT, flow rate- SF_6 : CHF_3:O_2 ::: 5 sccm : 20 sccm: 5 sccm, plasma power- 1000 W, operating temperature - 15° C, and forward power - 30 W.

The computational analysis of HCGs for high reflectivity is done using Rigorous Coupled Wave Analysis (RCWA)[128]. RCWA is a popular semi-analytical method in which the diffraction grating is distributed along the propagation path where the perturbation is considered periodic in nature. In this method, the electromagnetic field propagates through each layer, and solve the optimum solution for Maxwell's equations. The proposed reflector is designed in such a way that the ultra-high reflection for a wide range of oblique angles is achieved for both the TE and TM modes. The Fig. 3.11 (a) and (b) shows the reflection spectra for both the TE and TM modes respectively. The TE mode shows high reflectivity of greater than 99% for a wide range of angles as compared to the TM mode. It should be noted that the designed reflector includes the telecommunication wavelength i.e. λ = 1.55 µm in both the cases.

The polarization dependence behavior of the mirror is plotted in Fig. 3.12. The plotted contour shows the polarization-independent nature of mirror for 23°>θ>52° & 70°>θ>90°. It signifies that the designed reflector

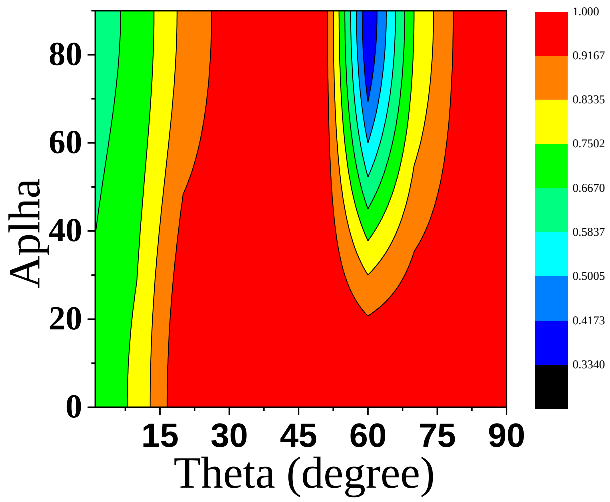

Figure 3.12 Polarization dependency of optical wave over the incidence angles at λ = 1.55 μm.

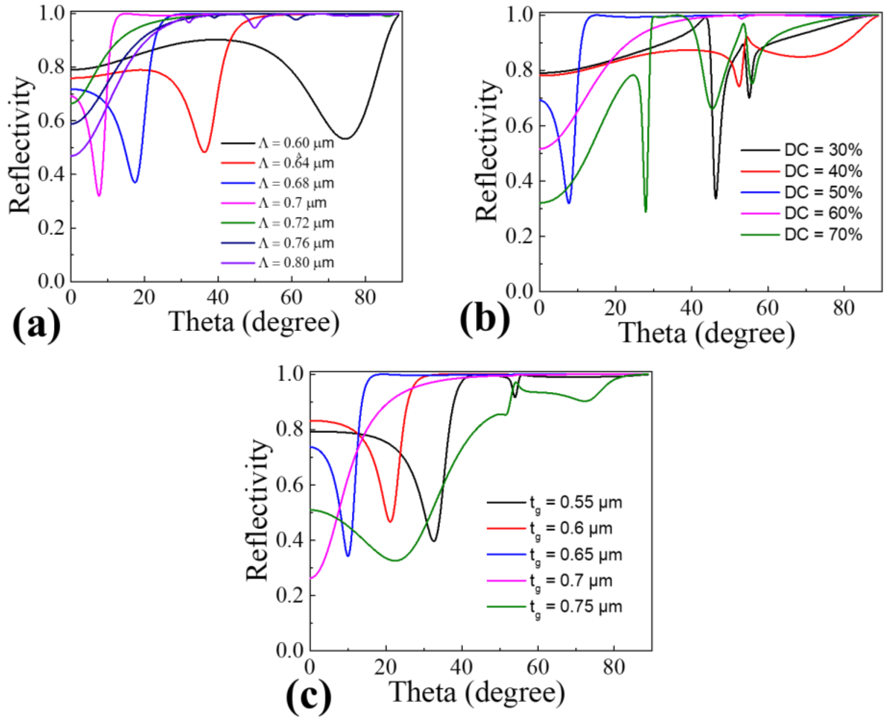

Figure 3.13 Analysis of fabrication tolerance at fixed λ = 1.55 µm. Reflectivity as a function of incidence angle for (a) distinct values of grating period. Dip in the reflectivity curve shift toward lower incidence angle with increase in grating period. (b) variation in duty cycle from optimized value of 50% causes unwanted variation in reflectivity curve. (c) High fabrication tolerance with varying etch depth is attributed by the reflector.

shows polarization-independent behavior in the given range of angles. Since periodic structures are always sensitive to its designing parameters, thus we have calculated the reflectivity of the mirror for possible error during the fabrication. First, we have simulated the reflectivity at λ = 1.55 µm (for TE mode) for different grating periods as shown in Fig. 3.13 (a). It shows that the high reflectivity can be achieved even if large variations of nearly ± 80nm present in the grating period. A similar analysis is computed for values of duty cycle and etch depth as shown in Fig. 3.13 (b) and (c) respectively. The duty cycle found to be the most sensitive parameter for the proposed reflector as the lower reflectivity is observed when the duty cycle is less than the optimized value, whereas the higher value of duty cycle exhibit unusual peaks at a distinct incidence angle. High tolerance behavior for variation in etching depth is observed.

3.2.2 Optical guidance in the hollow-core waveguide

The high reflectivity (>99%) observed in the proposed mirror for a broad range of wavelengths with polarization-independent attributes is highly desirable in the optical waveguide for efficient guiding mechanism. Following the same, we have designed a hollow-core waveguide by placing it as a mirror on the top and bottom of the waveguide as shown in Fig. 3.14. The principle of guiding light in the hollow-core region is different from conventional silica-based fiber where the condition of total internal reflection (TIR) must be satisfied to keep light into the high index core region. With this limitation, waveguide based on TIR cannot achieve a high value of the numerical aperture. In contrast to this situation, the proposed hollow-core waveguide works on the principle of Bragg reflection which bounces back the light from both the top and bottom mirror, and light can

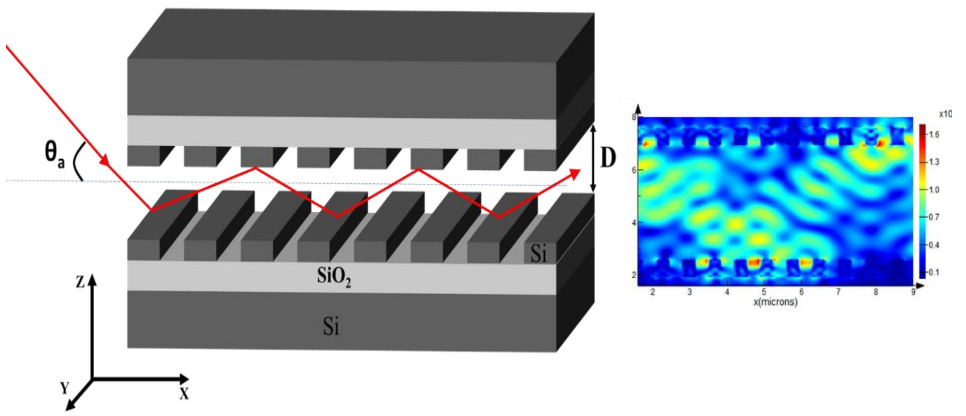

Figure 3.14 3D schematic view of hollow core waveguide (in the left), red line shows the incident light signal which propagate in the direction of grating period of waveguide. Right figure shows the propagation of light at λ = 1.55 µm in 4.5 µm thick air core using FDTD method.

propagate in the low-index region.

The guiding mechanism is illustrated in fig. 3.14 (b) where the light signal of 1.55 µm wavelength is incident at an angle of 45^0 from the left and it continuously propagates in the hollow-core region with discussed reflection mechanism. In such a guiding mechanism, the propagation loss of the signal depends on two factors: (i) reflectivity, and (ii) incidence angle. The value of optical loss can be given as[129], α (dB/m) = -10 $\frac{tan\theta_a}{D} logR$, where θ_a and D represents the angle of incidence and height of the hollow core region respectively, whereas R refers to the value of reflectivity at a given value of θ_a. The minimum value of the optical loss is observed at $\theta_a = 54°$ which is 0.013 dB/cm for 4.5μm thick air-core region. Such ultra-low loss characteristics are prerequisites for long-distance communication. We have also calculated the numerical aperture (NA = sin θ_a) of the proposed hollow-core waveguide for both the TE and TM modes. As shown in Fig. 3.15 (a), a very high value of NA that reaches up to ≈ 0.95 is achieved for TE mode at telecommunication wavelength. The value of NA is significantly high as compared to the standard silica fiber that has its value around ≈ 0.3 when a signal incident from air to silica fiber [130]. Moreover, the TM mode propagates in the waveguide also exhibits a high value of numerical aperture ≈ 0.8 but at a higher wavelength around 1.68 μm, whereas the calculated value of NA at λ = 1.55 μm is ≈ 0.31 which is comparable to the value of silica fiber.

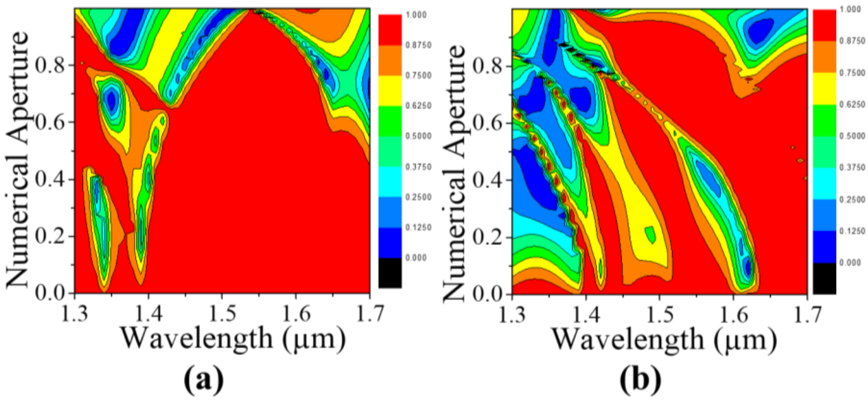

Figure 3.15 (a) Numerical aperture as function of wavelength exhibit highly reflective TE mode, the high value of numerical aperture with high reflectance >99% achieved at λ = 1.55 μm. (b) Calculated reflectivity for TM mode exhibit numerical aperture for broad wavelength range.

Summary

In this chapter, CMOS compatible optical structures for efficiently guiding and coupling of light into silicon waveguide using two different grating-based devices are presented. In the first device structure, we have designed, and fabricated the grating coupler for efficient coupling of light from off-chip optical fiber to on-chip Si waveguide and offers great flexibility to the measurement process. In this structure, we have discussed various optimization parameters and fabrication tolerance behavior of the coupler. We have shown optical measured characteristics in the presence of two different cladding materials i.e. air and water. In both cases, we have demonstrated efficient coupling of light into the device with broadband optical characteristics. The designed grating coupler has been used with other devices which are discussed in chapters 6 and 7 of this work. In another structure design of this chapter, broadband reflector made up of Si-Air high contrast grating is designed and fabricated. The highly reflective (>99.99%) broadband characteristics are obtained when light is incident at wide angles with respect to a horizontal plane. A hollow core waveguide based on such a highly reflective grating mirror is designed and investigated for guiding the light into the air-core region. The proposed hollow-core waveguide shows ultra-low loss characteristics along with a very high value of numerical aperture for TE guided mode. The device also shows polarization-independent behavior for a certain degree of angle ranges. The polarization independent nature of the proposed waveguide with broadband and ultra-low loss characteristics makes it a strong candidate for a verity of on-chip applications.

Chapter 4 Silicon-based slotted-rib waveguide for electro-optic modulation

4.1 Introduction

Silicon-based on-chip photonics has emerged as a key platform to integrate various high-performance optical devices with cost-effective CMOS fabrication technology [24,67,131–134]. In recent years chip-level high-quality data communication with optical interconnects using couplers, polarizers, optical modulators, multiplexer, demultiplexer [135–144] is widely studied. Optical modulation in silicon has been attractive for integrated silicon photonics. Several techniques with different structures have been pursued to achieve efficient electro-optic modulation. The modulator based on the micro-ring resonator is promising for the realization of high-speed operation with a low $V\pi L$ (modulation efficiency). However, a high-temperature sensitivity of the ring resonator is problematic, which causes additional power to compensate for a shift in the resonance. Another approach to get an efficient electro-optic modulation is resonant photonic structures [77,78] which in principle, increases the optical group index and exhibits slow light characteristics, resulting in a very low $V_\pi L$. The high light-matter interaction in such a structure results in high transmission losses. The PN junction under reverse bias can be used to achieve high operational bandwidth due to low RC time constant but at the cost of poor modulation efficiency [74,145]. On the other hand, small forward bias PIN-based devices exhibit very high modulation efficiency [69,71] but it suffers from low bandwidth due to large RC time constant because of large diffusion capacitance at the junction.

In order to eliminate RC time constant limitation imposed by lumped design and to increase the modulation bandwidth, modulator based on Traveling Wave (TW) electrodes is preferred [84,112,146]. A silicon-based electro-optic modulator based on the TW electrode configuration usually works in a depletion mode of operation. Some of the major issues with such modulators are the higher microwave loss and the high velocity/index mismatch at higher RF frequencies which limits the 3dB response of the device [112]. A previous study shows that any effort which reduces the microwave loss causes more index mismatch and vice-versa [26]. Optical guidance and control in a core of low index material have opened up a new class of optical functions in integrated photonics which includes devices like hollow-core waveguides, slot waveguide, etc. [41,147–149]. Incorporation of TW electrodes with low-index waveguides can enable tailorable electro-optic coupling to provide efficient optical modulation in silicon. Slot-waveguide based electro-optic modulator having the electro-optic polymer in slot region exhibit high modulation efficiency and small footprint [36,111]. Thermal instability, high transmission losses, deterioration with time, and high-temperature sensitivity are some concerning issues of polymer-based electro-optic modulators.

In this work, an engineered slotted-rib is used to guide the light in a slot region. Strong optical confinement with acceptably low loss is realized in the slot region. Traveling wave electrode with slotted-rib design offers efficient optical modulation in silicon. In the proposed device structure, PN junction is formed in one of the silicon ribs which is driven by applying reverse bias. The modulation of light in the slot region is observed due to the depletion of carriers in the cladding of the waveguide which leads to a change in an evanescent wave coupled in the slot region. An improved coupling between optical and microwave mode at the higher RF frequencies is observed without affecting the microwave loss. It is due to the low optical group index in the slot region does not require to have a smaller width and height of the electrode to achieve a high value of RF effective refractive index. This improvement in coupling is achieved due to the excellent velocity/index matching between these two modes using the engineered slotted rib structure. The high-speed operation of 70 Gbps with an extinction ratio of ≈ 4.9 dB is achieved at a low driving voltage of 3 Vpp. However, the moderate modulation efficiency of >2V.cm is still an issue in such type of modulator. The low insertion loss of 3.1 dB with VπL of 2.1 V-cm is numerically calculated at a reverse bias of 4 V. The computations are performed at an operating wavelength of 1550 nm. Since the bandwidth of TW based modulator is not limited by RC time constant, an optimized TW slotted-rib structure can be used to achieve a higher data-rate with a high extinction ratio. Applications of such a device can be found where a high data rate is required such as optical interconnect in data centers.

4.2 Device design and optimization

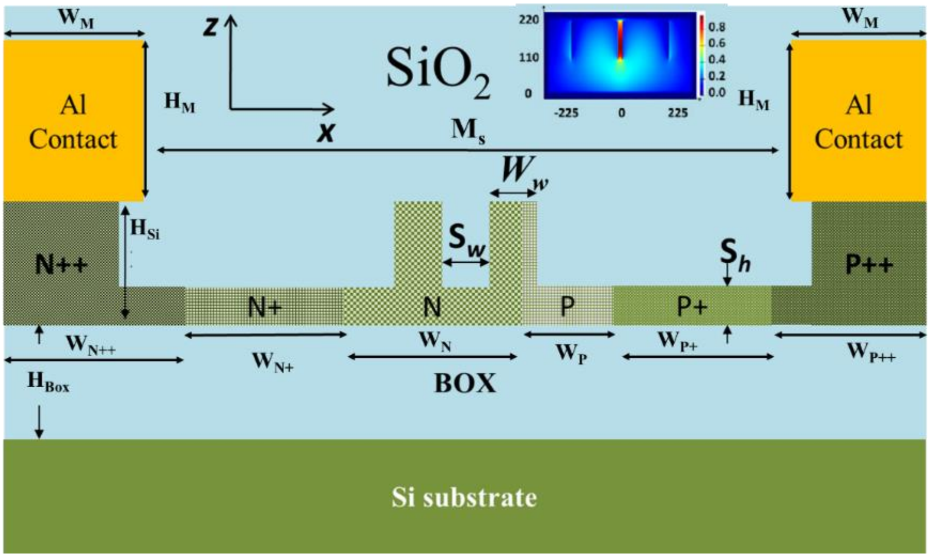

Figure 4.1 The schematic of the slotted-rib electro-optic modulator with aluminium electrodes on 220 nm SOI wafer and top of the device is passivated with a thick oxide layer, different coloured strips indicating different doping concentration level, the inset shows surface electric field distribution of the optical mode in the x-direction (Ww = 200 nm, Sw = 50 nm, Sh = 80 nm).

Optical modulation based on the plasma dispersion effect is mainly due to electrically induced change in the free carrier concentration that interacts with the optical wave. If we go deeper into the modulation process, according to the Soref model [67] changes in hole concentration dominantly affect the optical modulation but at the same time, it also increases the optical loss. Overall, the modulation efficiency and the optical loss are the tradeoff quantities therefore it needs to be considered carefully while designing the modulator. In the past one-decade different doping-based geometry in the waveguide has been proposed. Based on that, it can be mainly divided into three types: 1. Horizontally doped p-n junction, 2. Vertically doped p-n junction and 3. Interleaved p-n junction.

Table 2 Summary of designing parameters for proposed slotted-rib optical modulator

Parameters Name	**Description**	**Optimized parameter/Value**
W_w	rib width	200 nm
S_w	slot width	50 nm
D_{P++}	Doping concentration of p++ region	10^{19} /cm^3
D_{N++}	Doping concentration of n++ region	10^{19} /cm^3
D_{P+}	Doping concentration of p+ region	7×10^{17} /cm^3
D_{N+}	Doping concentration of n+ region	5×10^{17} /cm^3
D_P	Doping concentration of p region	9×10^{17} /cm^3
D_N	Doping concentration of n region	7×10^{17} /cm^3
D_{ref}	Reference concentration level	1×10^{6} /cm^3
W_{p++}/W_{n++}	Width of p++ and n++ region	5 µm
W_{p+}/W_{n+}	Width of p+ and n+ region	1 µm
W_p	Width of p region	1.125 µm
W_n	Width of n region	1.375 µm
W_{dep}	Depletion layer width	110 nm
H_{Box}	Height of oxide thickness	3 µm
H_{Si}	Height of Device layer	220 nm
S_h	Strip height	80 nm

In this theoretical work, horizontally aligned p-n junction is considered due to its easy fabrication process and simple metal contact arrangement. Doping in the waveguide region is optimized such that the best possible modulation efficiency is obtained with the acceptable optical loss for high-speed data rate operation. For this, the proposed device is designed on 220 nm thick top silicon of SOI as shown in Fig. 4.1, the inset shows the mode-field distribution of the optical wave in the slot region. A 3 µm thick Buried Oxide (BOX) is chosen to suppress the coupling of optical mode from the slotted-rib waveguide to the silicon under the oxide layer. Silicon rib in the device structure is partially etched, to create slotted-rib, with an etch-depth of 140 nm. The remaining silicon under the slot is used to provide a channel for the charge carriers to flow between the two electrodes. The strip load thickness of 80 nm is chosen such that it does not affect the high-speed operation of the device and maintain adequate confinement in the slot region.

The rib width (W_w) and slot width (S_w) are 200 nm and 50 nm respectively. The peak doping concentration of silicon near both the Al contacts is kept at 10^{19} cm^{-3} that ensures ohmic contact at the junction and reduces the excess resistance. A PN junction is formed on the right side of the slotted-rib while the left side is completely defined with the lightly doped N-type material. We chose a doping concentration of 7×10^{17} cm^{-3} for P-type and 9×10^{17} cm^{-3} for the N-type region. Moderately doped $P+$ and $N+$ region are defined between heavily doped silicon near metal–silicon junction ($P{++}$ and $N{++}$) and lightly doped P and N region in waveguide region. The full list of device parameters and the constants used in the simulation are summarized in Table 2.

Since the proposed structure is symmetrically transverse in the y-direction, to obtain the modulation of charge concentration with applied electrostatic potential, 2-D model in the y-normal direction is used. This model solves the drift diffusion equation and the Poisson's equation simultaneously. The changes in the effective index can be approximated using the expression as follows

$$\Delta n_{eff} = \iint |\Psi(x,z)|^2 \Delta n(x,z) dxdz \qquad (4.1)$$

where $|\Psi|^2$ and Δn represent the normalized optical intensity and modulation of the refractive index of the material, respectively. After calculating the index modulation, optical and RF characteristics are determined using the commercially available simulation tool [46]. Finally, the dynamic response of the device is calculated which actually signifies the device performance for high data rate applications.

The fabrication process of the proposed device can be done in the following steps. However, it should be noted that the work shown here is fully based on theoretical analysis. The proposed device design is compatible with the mature CMOS process. The SOI wafer is taken in the first step of the process. To form the silicon rib of 450 nm on the 220 nm thick top silicon, photoresist can be patterned at the center (without slot) and at both sides of the device using optical lithography followed by the development process. Either the wet or the dry etching (RIE) can be used to achieve the required etch depth in the silicon. Doping is the most important part of the process which needs selective opening of the mask having sufficient thickness over the sample. When the sample is bombarded with desired doping atoms, only the opened area will be doped, and the remaining portion will be protected by the thicker mask layer. Practically when this process is performed, the thick layer of SiO_2 is taken to isolate the area where doping is not required. By repeating this step number of times, different doping profiles can be achieved in a single device. Slot formation can be done with proper alignment of the device electron beam lithography process followed by the dry etching process. In the next step, the sample is passivated with the thick layer of oxide and finally, metal contact can be formed after etching the oxide layer.

4.3 RF characteristics

The proposed TW electrode is designed as a coplanar waveguide such that the RF mode is tightly coupled with the optical mode. The coplanar electrode is designed by considering the following criterion to achieve efficient optical modulation in the waveguide:

• To achieve maximum interaction between optical and microwave waves they should travel with the same velocity (optical group index should be equal to RF effective index). As we know that the actual velocity of the optical wave can be taken as the optical group index and velocity of the RF signal which have the information signal in the electrical form can be in either group velocity of the RF mode or in-phase part of it (Real part of effective refractive index). If someone wants to modulate the intensity of the optical signal directly with the RF signal, then the group velocity of the RF signal must be matched with the optical group velocity. Whereas if someone wants to achieve a phase modulator first then the optical group index must be the same with the real part of the effective refractive index which will have an information signal. Any velocity mismatch between these two modes can produce inter-symbolic interference that can degrade the performance of the modulator.

• In order to avoid reflection at the input and output, all impedances i.e. source impedance, output impedance and the characteristic impedance of loaded transmission line should be the same at the desired operating frequency. Impedance matching will ensure the maximum power transfer to the device.

• To improve dynamic modulation depth of TW modulator, microwave losses should be as low as possible. It is the most crucial parameter as I will heavily affect the electrical bandwidth of the loaded transmission line. Apart from the dimensions of the electrode, microwave loss heavily depends on the doping concentration and resistance of the device. The offered low optical group index in this work enables us to have low microwave loss with better index matching of the optical and RF signal.

The optimized designing parameters for the traveling electrode and some constant are given in table 3.

The RF characteristics of the loaded transmission line are simulated by designing the equivalent circuit model as shown in Fig. 4.2. This model represents the classical model of the transmission line with the embedded device parameters like resistance and capacitance.

The propagation constant ($\gamma = \alpha + j\beta$) for a given transmission line can be simplified as follows [150]

$$\propto = \frac{1}{2} R_T \sqrt{\frac{C_D + C_T}{L_T}} + \omega^2 C_D^2 R_S \sqrt{\frac{L_T}{C_D + C_T}} \tag{4.2}$$

$$\beta = j\omega \sqrt{L_T (C_D + C_T)} \tag{4.3}$$

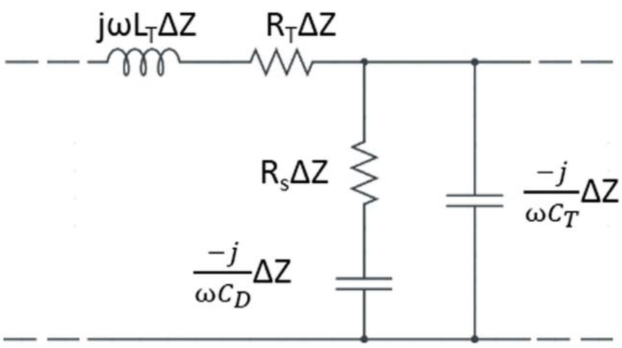

Figure 4.2 Equivalent circuit model of the loaded transmission line. To integrate behavior of modulator with the unloaded classical transmission line model, depletion capacitance (C_D) in series with strip load resistance (R_S) is kept in parallel with classical transmission line capacitance (C_T).

Table 3 Summary of various designing parameters of transmission line

Parameters Name	**Description**	**Optimized parameters/value**
W_M	Width of metal electrode	3 μm
H_M	Height of metal electrode	2 μm
M_S	Spacing between metal electrode	8 μm
ε_0	Permittivity in vacuum	8.85×10^{-12} F/m
μ_0	Permeability in vacuum	$4\pi\times10^{-7}$ H/m
ε_{Si}	Relative permittivity of silicon	11.9
ε_{SiO2}	Relative permittivity of SiO2	1.56
K_{al}	Conductivity of aluminium electrode	3.8×10^{7} S/m
ρ_{sub}	Resistivity of silicon substrate	750 Ω.cm
ρ_{Si}	Resistivity of top silicon layer	10 Ω.cm

where L_T , C_T, and R_T are inductance, capacitance, and resistance of unloaded transmission line respectively, whereas R_S and C_D represent strip load resistance and depletion capacitance between two metal lines respectively. The dependency of R_S and C_D on attenuation constant (α) is shown in Eq.

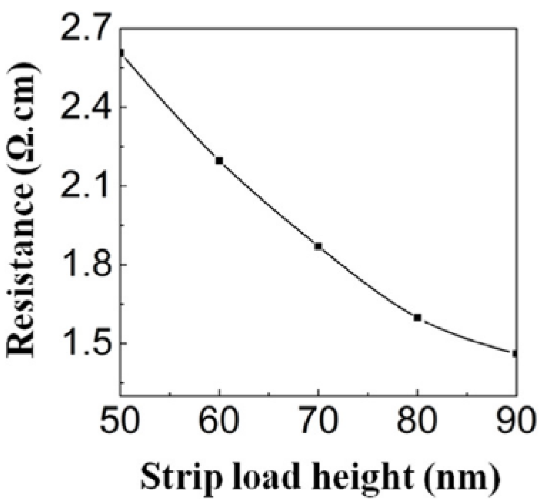

Figure 4.3 Effect of change in strip load height (S_h) on resistance (R_S), for a proposed device parameter. At S_h = 80 nm, value of the strip load resistance is 1.6 Ω cm.

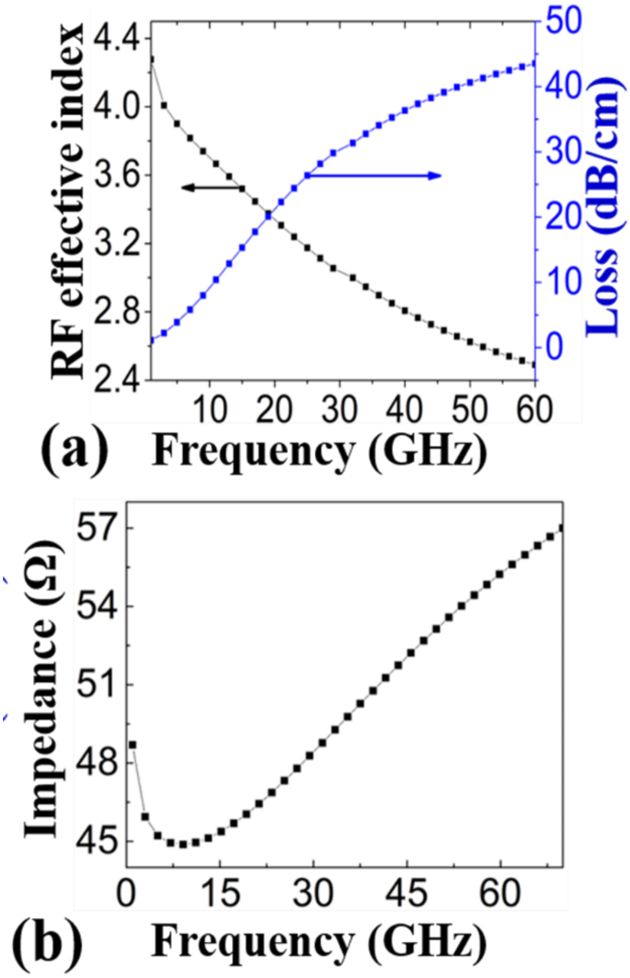

Figure 4.4 The dependency of RF parameters on microwave frequency at $V_R = -4$ V. (a) Variation of the real part of effective index and loss, the value of the effective index is 2.93 at 35 GHz and (b) impedance as a function of frequency.

(4.2). Attenuation can be reduced by decreasing R_S and C_D, which is the primary concern in order to reduce microwave loss. Moreover, in contrast to Eq. (4.2), improvement in phase constant (β) can be achieved with a larger value of C_D as indicated in Eq. (4.3). From both the equations, we concluded that the low value of R_S is needed to access high bandwidth operation. However, the value of C_D needs to be carefully chosen as we need its high value to achieve efficient phase modulation but at the same time, it adversely affects the microwave loss. The value of the depletion capacitance can be controlled by choosing a moderate/light doping profile in the p–n junction. Higher doping levels will result in a high value of C_D which increases the microwave loss and limits the high-speed operation of the device. Fig. 4.3 shows the dependency of

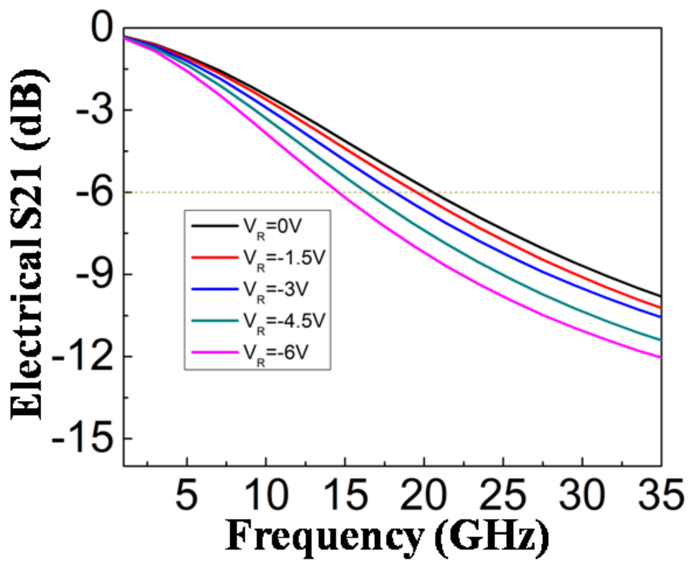

Figure 4.5 Electrical S21 parameter as a function of frequency under different reverse bias voltage. 6 dB bandwidth of 22.4 GHz is achieved at $VR = -6$ V.

strip load resistance on its thickness, it can be seen that thicker strip loading is favorable to reduce resistance, but at the same time, thicker strip loading can result in weak optical confinement in slot region which creates a trade-off in the selection of strip load height (S_h). A S_h of 80 nm is chosen such that it provides strong optical confinement and a low microwave loss. Fig. 4.4 (a) shows the dependency of RF effective index and loss on microwave frequency, RF losses increase, and RF effective index decreases with an increase in microwave frequency. This decrease in effective index creates a velocity mismatch in the silicon-based rib waveguide structures. The optical group index of a silicon-rib lies near 4 whereas RF effective index is much lower than this value at higher microwave frequencies.

To overcome this mismatch issue and to improve the dynamic response of the modulator, the slotted-rib structure is employed in the proposed device design. Fig. 4.4 (b) shows the frequency dependence of the RF impedance of the transmission line equivalent (shown in Fig. 4.2) of the proposed device. Impedance first decreases up to 11 GHz of frequency because of the dominance of capacitive reactance. Impedance starts increasing as inductive reactance dominates over the capacitance beyond 11 GHz. At 35 GHz microwave frequency, the Characteristic Impedance of loaded transmission line and RF effective index are 49.72 + 3.32i Ω and 2.93 respectively. In the proposed device structure, the optical group index of 2.91 is calculated for the given device parameters, which is close enough to the RF effective index at 35 GHz. It enables efficient coupling between optical and microwave mode. Finally, the electrical S parameter is calculated by studying the impulse response of the loaded transmission line as shown in Fig. 4.5. It is clear from the figure that 6 dB bandwidth is in excess of 22 GHz which is sufficient enough to operate the device at a higher data-rate.

4.4 Electro-optic characteristics

In this section, modulation characteristics of the proposed device under static and dynamic conditions are studied which are as follows:

4.4.1 Static characteristics

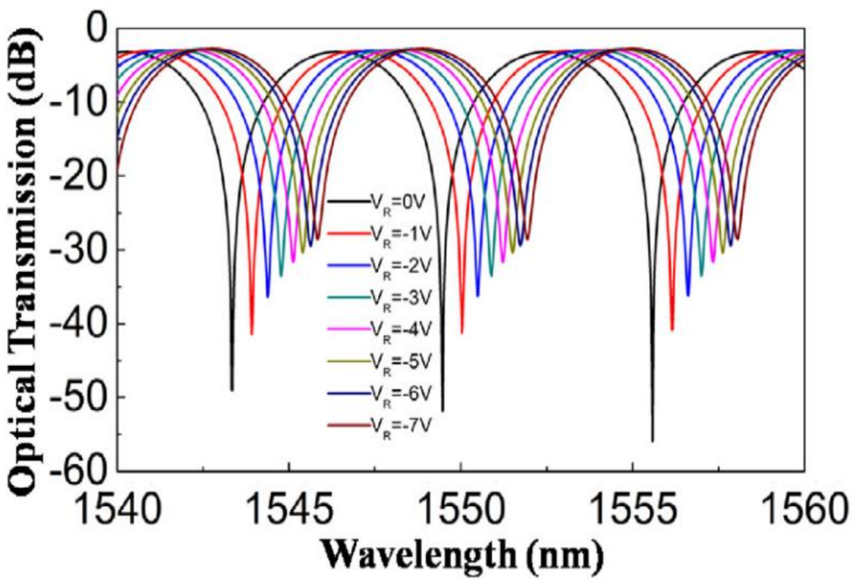

Figure 4.6 (a) The optical transmission spectra of 4 mm long Mach Zehnder Interferometer (MZI) under different bias voltage. The voltage is applied to one arm of MZI and another arm is kept at zero potential.

The proposed device enables efficient optical phase modulation under the application of different reverse bias voltages. The optical mode is confined in the 50 nm wide slot region. The slotted-rib is optimized such that it provides strongly coupled optical and microwave modes with, nearly, the same velocities. In Fig. 4.6 optical transmission spectra of 4 mm long MZI (Mach Zehnder Interferometer) is plotted as a function of wavelength under different reverse

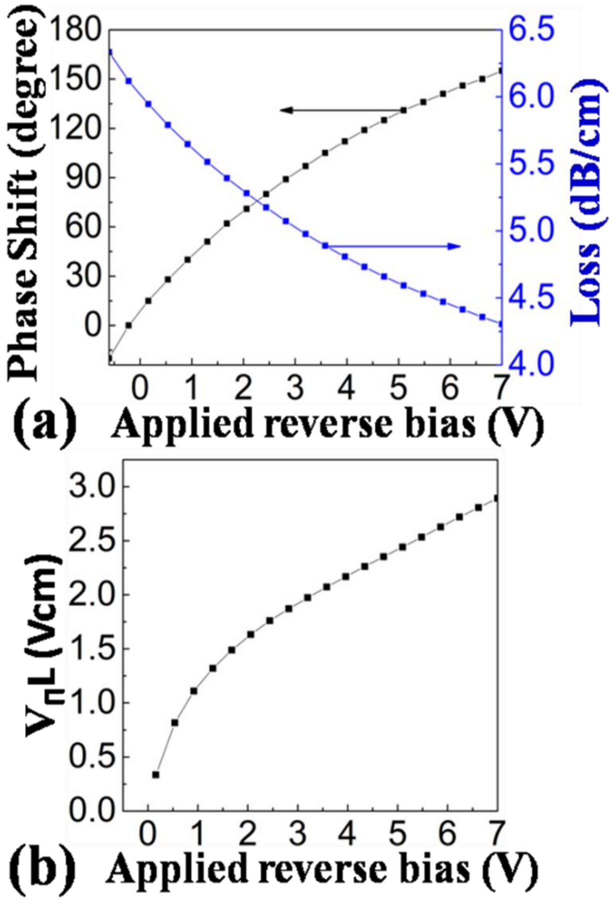

Figure 4.7 (a) Relative phase shift and the optical transmission loss under a different reverse bias voltage. Phase shift of 180◦ is found at reverse bias of 7 V. (b) $V_{\pi}L$ is equals to 2.1 V-cm at $VR = -4$ V for a 4 mm long device.

bias voltage (length of both the MZI's arms is intentionally mismatched by 100 µm). The spacing between successive optical fringes is reduced as the reverse bias is increased. This is due to the fact that the free charge carriers in the PN junction deplete continuously with an increase in applied reverse voltage, thus the interaction between optical wave and the free charge carriers becomes weak. These changes in the interaction alter the effective refractive index of the silicon accordingly. Similar changes are reflected in the evanescent wave coupled in the slot region. Here, it is also important to note that the static extinction ratio is decreasing with an increase in the reverse voltage. It is because of a change in the respective optical loss between the two MZI arms.

To obtain the maximum static extinction ratio, it is important to have an equal loss for both the MZI arms which will produce the highest difference in constructive and destructive interference with a change in respective phase at the MZI output. The variation in the effective refractive index of the optical mode confined in the slot region strongly depends on the slot width. Since our active region is situated in one of the device widths thus optical mode must have efficient coupling with those areas. The calculated insertion loss (i.e. peak value of transmission spectra) and FSR @ 7 V are 3.1 dB and ~ 6 nm respectively. For further calculations of relative phase shift and corresponding $V_{\pi}L$, the

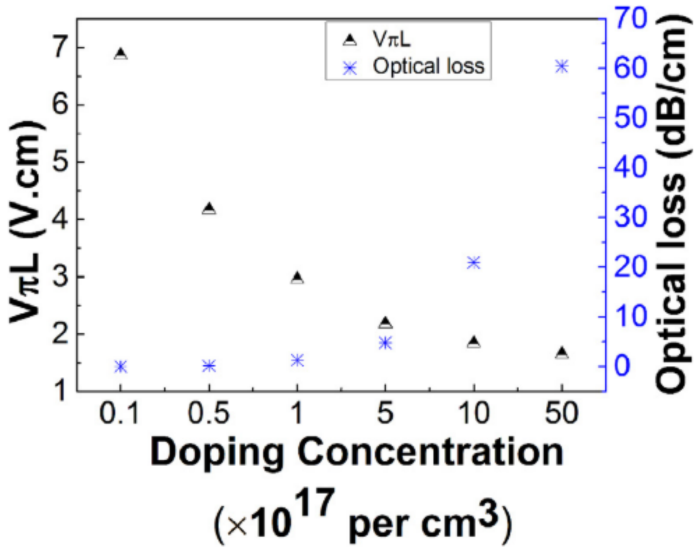

Figure 4.8 $V_{\pi}L$ and optical loss as a function of doping concentration at λ = 1550 nm optical wavelength.

following relations are used as given below.

$$\Delta\emptyset = 360\frac{\Delta\lambda}{FSR} \tag{4.4}$$

$$V_{\pi}L = \frac{V_R L}{2\Delta\lambda}FSR \tag{4.5}$$

where $\Delta\lambda$ is a shift in wavelength due to a varying reverse bias voltage (V_R) and L is the length of phase modulator arm. Fig. 4.7 (a) shows the relative change in phase ($\Delta\phi$) and loss with applied reverse bias. Lightly doped PN junction in one of the ribs near the slot region results in the optical propagation loss of 4.7 dB/cm at a reverse bias of 4 V which is acceptable for millimeter long practical devices. Modulation efficiency ($V_{\pi}L$) under varying reverse bias voltage is plotted in Fig. 4.7 (b). $V_{\pi}L$ of 2.1 V-cm is achieved at a reverse voltage of 4 V which can be further improved by increasing the doping in the

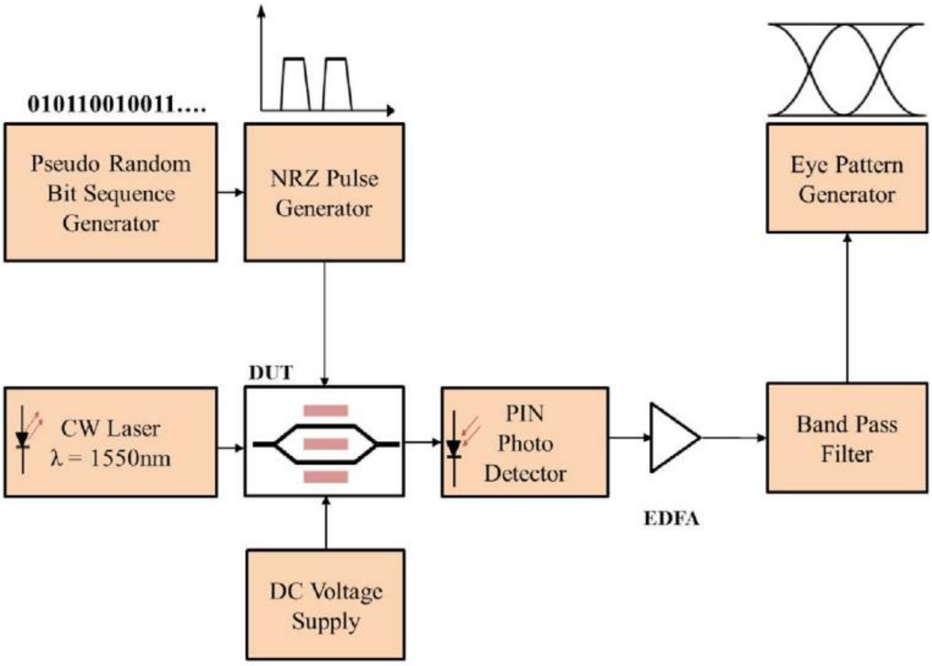

Figure 4.9 The block diagram for speed performance analysis of the proposed device.

PN junction but at the cost of increased optical losses. Fig. 4.8 shows the dependency of modulation efficiency and optical loss on the doping concentration. Optical loss increases drastically with an increase in doping concentration whereas improvement in the $V_\pi L$ can be seen simultaneously. The doping concentration near to 7×10^{17} per cm^3 is found the best trade-off quantity to achieve acceptably low optical loss with better modulation efficiency. It is also important to note that the interaction of the optical wave with the cladding material is inversely proportional to the optical confinement in the slot region. In order to increase the modulation efficiency, one can opt asymmetric slot structure where rib with embedded PN junction with has wider width with respect to others.

4.4.2 Dynamic characteristics

The dynamic behavior of the optical signal at MZI output is studied by applying the AC signal (V_{pp}) along with the DC voltage supply. The simulation setup for analyzing the speed is shown in Fig. 4.9. Pseudo-Random Binary Sequence (PRBS) with NRZ technique is used to generate digital data sequence to feed signal at the electrode. The optical signal of

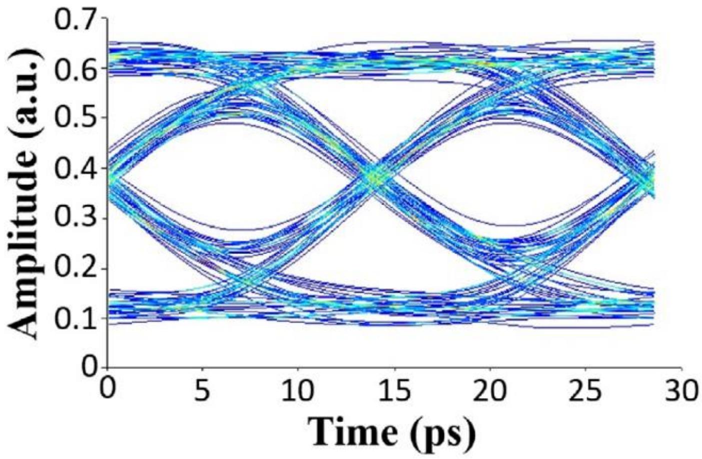

Figure 4.10 Eye diagram at 1550 nm wavelength, eye opening exhibit extinction ratio of ≈ *4.9 dB with* $Vpp = 3$ *V at* $VR = -4$ *V.*

0.5-Watt power at 1550 nm is given to the input arms of MZI. The value source and termination impedance are kept at 50 Ω which is the globally accepted standard value. The modulated optical signal is converted into electrical form at PIN photodetector. The interference pattern is measured at the output after amplifying the optical signal by 3 dB using EDFA (Erbium-Doped Fiber Amplifier). A clear eye-opening at 70 Gbps is achieved with an extinction ratio of ≈ 4.9 dB with 3 V_{pp} and 4 V of reverse bias is shown in Fig. 4.10. The eye-opening can be further improved with the further amplified optical signal using EDFA, but it introduces non-linearity at the output signal. On the other hand, one can use a larger value of swing voltage which can improve the dynamic response but at the cost of excessive power consumption per bit. The speed performance is also observed after including some major practical imperfectness (of about 5%) including change in doping concentration, the resistivity of the material, slot width, and rib width of the structure, which is expected during the fabrication process. ER varies in between 4.9 dB to 4.5 dB with these changes in parameters which is practically acceptable.

Summary

In summary, a silicon-based optical modulator with an engineered structure is presented in this chapter. The guidance of optical mode in the low index slotted-rib region causes velocity matching between optical and microwave modes resulting from matched optical group index with RF effective index. The proposed electro-optic modulator not being limited by RC time constant provides a high modulation speed up to 70 Gbps with a high extinction ratio of ≈ 4.9 dB at a driving voltage of $3V_{pp}$ and a reverse bias voltage of 4 V. An insertion loss of 3.1 dB is obtained for a 4 mm long device. The optical group index can be further tuned by varying rib width, slot width, and strip load height. It gives flexibility in modulator structure design to operate at the desired operating frequency. To further improve the performance of the proposed modulator, the parameters of the transmission line i.e. microwave loss and characteristic impedance can be optimized. The proposed slotted-rib waveguide used with TW based coplanar waveguide structure has the potential to achieve better velocity matching condition, which can be used in high-speed on-chip optical interconnects. The value of modulation efficiency

Chapter 5 Laterally Split Vertical p-n Junction for efficient optical modulation

5.1 Introduction

Photonic-electronic signal processing is an essential building block for the optical communication system [151–155]. As discussed in the earlier chapter, Si photonics offers a cost-effective and complementary metal-oxide-semiconductor (CMOS) compatible fabrication platform and thus it opens avenues for the integration of electronic and optical components on the monolithic platform [132,134,135]. To establish a high-speed link between the electronic and optical components, Electro-Optic Modulator (EOM) can play a vital role in a variety of applications including telecommunication to on-chip optical interconnects [69,136,142]. Due to absence of strong EO effect like Pockel's effect, moderate free-carrier effect (also known as plasma dispersion) effect and weak Franz-Keldysh effect in crystalline silicon at telecommunication wavelength, other advanced materials like graphene, Indium Tin Oxide (ITO) and EO polymers have been widely explored in silicon-based hybrid modulators [24,36,40,156–159]. The outstanding proprieties of these advanced materials like high mobility in graphene, Epsilon Near Zero (ENZ) in ITO, and large EO coefficients of EO-polymers (r_{33}) enhances the modulation efficiency with many folds. However, non-compatibility issues of these materials with the CMOS fabrication platform makes it a difficult choice for highly dense integrated photonic IC's. With the above-mentioned fact, devices based on the doped silicon are the most suitable choice for a fully CMOS compatible fabrication platform. Such devices rely on the plasma dispersion effect that allows the adequate index modulation with the application of applied external bias [67]. Several structures based on doped-Si have been pursued to achieve efficient optical modulation in silicon.

Depending upon the adopted structure geometry and design parameters, desirable optical characteristics can be achieved in resonator-based structures like Micro-Ring Resonator (MRR), Bragg grating and photonic crystal, which exhibit low power consumption and small footprint area [78,160–164]. Slow light effect in such structures results in enhanced light-material interaction, thus various modulation parameters can be improved. In consequence of this slow light effect, second-order dispersion also increases which leads to narrow the resonance peak at the output. Apart from these advantages, resonant structures are complex to fabricate and show narrow bandwidth operation that results in very high-temperature sensitivity of these structures and makes it inadmissible for many on-chip applications.

In order to achieve thermally stable and wide optical bandwidth modulation characteristics, p-n/p-i-n junction-based devices have attracted much interest over the few decades. Forward bias operated injection-type EOM shows extremely low $V_{\pi}L$ (high modulation efficiency), but the drawback with such modulator is its limited 3-dB bandwidth [69]. This is due to the long free-carrier lifetime and large diffusion capacitance at the junction. In contrast to this situation, the depletion type optical modulator is promising for the realization of high data rate performance [74,145]. It is because the devices which are operated in depletion mode are not limited by the free carrier lifetime and exhibits low depletion capacitance at the junction. High reverse bias or long arm length requirement (to achieve π shift) are the major issues with this mode of operation which prohibit the device to achieve high modulation efficiency. However, the overall performance of the depletion type modulator depends on the number of parameters like doping concentration and junction orientation. In depletion mode operation, lateral and vertical junction orientations are the two most explored configurations. To achieve high 3dB bandwidth, a laterally oriented p-n junction is preferred over the vertical junction. It is because of the large depletion capacitance formed in the vertically doped junction as compared to the laterally doped junction adversely affects the RC time constant and thus degrade the dynamic response of the modulator. The VπL which is another crucial performance parameter for such class of electro-optic modulators is much better in the case of the vertical p-n junction (VπL< 1 V-cm) as compared to the laterally oriented junction (VπL> 2 V-cm). From the above discussion, it is clarified that the modulation efficiency and 3-dB bandwidth are the two trade off quantities between vertically and laterally oriented p-n junctions. This work is intended to break this trade-off using the engineered structure and show significant improvement in performance metrics.

Recently, we have reported effective modulation of the optical signal in the silicon-slot structure using the p-n junction situated in the cladding region. In the reported work, we achieved a high-speed data rate due to strong coupling between optical and RF modes, although the moderate modulation efficiency remains an issue [35]. In order to overcome the same, the proposed structure is designed such that high 3-dB bandwidth along with high modulation efficiency is obtained simultaneously. Vertically oriented p-n junction in the silicon ridge is laterally separated into two independent electrically isolated junctions using the slot structure. The creation of a slot region in the silicon ridge causes a common optical mode in between these two junctions. Optical index modulation which primarily depends on the light-material interaction is improved using the vertically aligned p-n junction with an appropriate doping profile. However, laterally separated p-n junction not only provide low depletion capacitance and resistance but also maintain the strong light-material interaction simultaneously. High modulation efficiency of 0.74 V-cm with 3-dB intrinsic bandwidth of ≈ 58 GHz is obtained without any TW electrode configuration. The data rate of 25 Gbit/s is observed with an Extinction Ratio (ER) of 2.6 dB in this case. To further improve the device performance, the TW electrode is introduced as a coplanar waveguide. With the advantage of proposed structure geometry, the optical group index of 3.3 is achieved that matched well with the RF effective index at higher microwave frequencies. A high data rate of 100 Gbit/s is achieved with 2.4 dB ER for an applied bias of -2 V and 5 V_{pp}. The high-speed performance with the inherent wide optical bandwidth makes the device useful for applications like optical coherent systems, data centers, etc.

5.2 Device Design

The 3D-view of the proposed phase shifter arm is shown in fig. 5.1 (a). The device is designed on the 220 nm thick top silicon of SOI which is the foundry standard for CMOS fabrication platform. Light-matter interaction is improved with an increase in the active p-n junction area that interacts with the optical

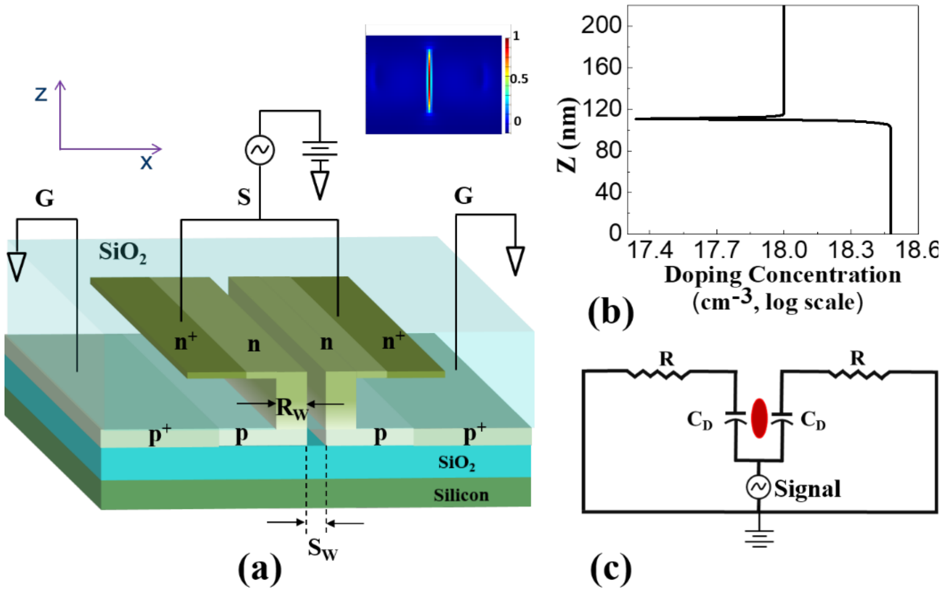

Figure 5.1 Schematic of the proposed phase modulator where y is the direction of propagation and p-n junction is aligned in the z direction. Top and slot of the device is covered with a 2 μm thick SiO2 layer. Inset shows the electric field distribution of the optical mode in the slot region at λ = 1550 nm, b) Optimized doping profile of the silicon rib in the vertical direction, c) simplified RC equivalent model of the device, where R represent the resistance between the ground to signal electrode and CD represents the depletion capacitance of individual junction.

mode. However, splitting of the junction in lateral direction helps to reduce capacitance and resistance of the individual junction. The slot and rib width of the wave-guiding arm are 50 nm and 200 nm respectively. The thickness of the silicon pad is 80 nm for the ground electrode and 50 nm for the signal electrode contacts. In Fig. 5.1 (b) doping concentration of the silicon rib is plotted in the vertical z-direction. The p-type region is doped with a maximum doping concentration of 3×10^{18} cm−3, whereas the doping concentration of the n-type region is kept at 1×10^{18} cm^{-3}. To ensure an ohmic contact, and to reduce the excess resistance of the device, peak doping concentration of silicon near metal contact is 10^{20} cm^{-3} for both p^+ and n^+ region. The RC equivalent lumped circuit of the proposed structure is drawn in Fig. 5.1 (c). The common optical mode characteristics in between both p-n junctions can be tuned with the applied external bias. For the synchronous operation of both p-n junctions, the common signal electrode is applied across both n^+ regions, whereas the other two electrodes are kept grounded. This arrangement of two insulated p-n junctions reduces the capacitance and resistance of the device, which in turn reduces the overall RC time constant. This enables the high-speed operation of the device along with the strong light-material interaction. Another advantage of the proposed structure is the broadband operation of the device. It is simply due to a non-resonant device structure that doesn't form any resonance peak at the device output. However, one big issue with the non-resonant structure is the requirement of a long waveguide to produce an adequate phase shift which further can be converted to intensity modulation using Mach Zehnder interferometer configuration.

Soref and Bennett [67] experimentally demonstrated the change in the material refractive index for a wide range of wavelengths. They also represented the dependency of refractive index (Δn) and absorption coefficient ($\Delta\alpha$) over free electrons concentration (Δn_e) and free holes concentration (Δn_h) at $\lambda = 1550$ nm through the mathematical expression as follows:

$$\Delta n = -[8.8 \times 10^{-22} \Delta n_e + 8.5 \times 10^{-18} \Delta n_h^{0.8} \quad (5.1)$$

$$\Delta\alpha = \quad 8.5 \times 10^{-18} \Delta n_e + 6 \times 10^{-18} \Delta n_h \quad (5.2)$$

it suggests that the holes are dominantly responsible for bringing changes in the material index, i.e. why the concentration of p-type doping is kept higher than the n-type region. In order to achieve maximum changes in the material index, the width of the depletion region should be extended as maximum possible in the waveguide region. It increases the interaction of the optical wave with an active p-n junction. To achieve this condition, the n-type doping concentration is kept at a lower level so that the depletion width can extend deeper across the junction. The charge transportation behavior and optical mode analysis of the device are performed using the Lumerical Device and Mode solution respectively [46].

5.3 Device Analysis

The electrically tunable optical characteristics of the proposed device are observed in this section. Further analysis of device is divided into three parts where the effect of external electric field either with DC voltage or in conmitnation with swing voltages are observed here as follows:

5.3.1 Under DC Bias

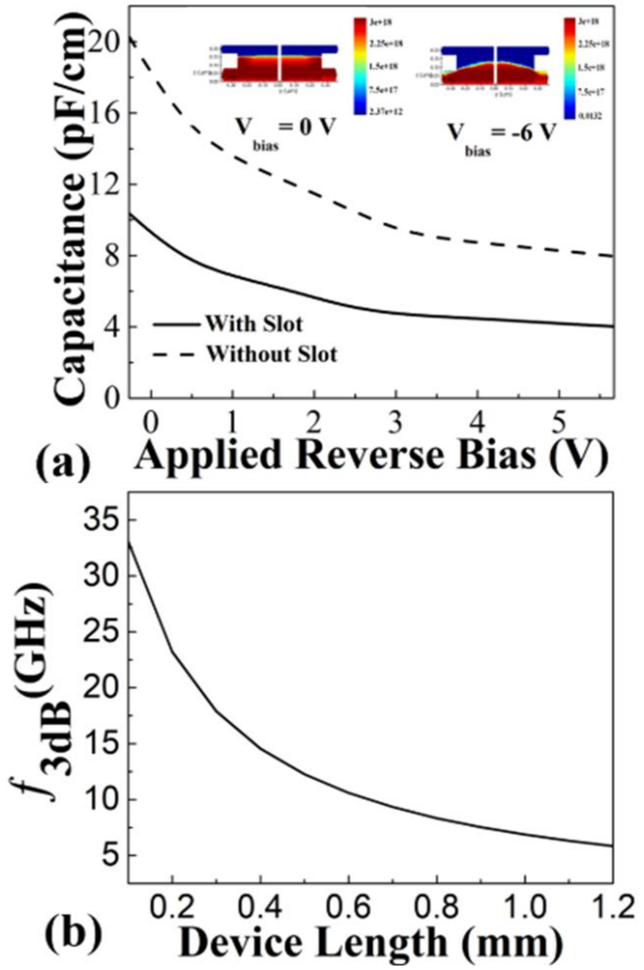

Figure 5.2 (a) Depletion capacitance (C_D) as a function of applied bias. Dash line represents C_D when slot is filled with silicon material; solid line shows capacitance for one of the p-n junctions. Two inset shows the depletion of holes with applied bias of 0 V and -6 V between the signal and ground electrode. (b) Dependency of 3-dB bandwidth on device length at V_{bias} = -6 V and termination impedance of 50 Ω.

Better coupling of optical mode with the active p-n junction can be achieved with the vertically doped junction. It is because the standard CMOS platform use 220-nm thick top silicon and the typical width of conventional silicon waveguide remains near 500 nm to support the single-mode operation of the optical wave. It is clear from the above observation that the waveguide width is approximately 2 times greater than its height, thus we can conclude that the vertical p-n junction can facilitate better light-material interaction as compared to the lateral doped junction as junction width will also be doubled in this arrangement. The efficient optical phase modulation is achieved with the application of the drive voltage. The depletion capacitance is first analyzed for two different cases i.e. without slot and with-slot condition. As shown in Fig. 5.2 (a) depletion capacitance is approximately half for the case of the with-slot condition. It imparts an extra benefit over the conventional vertically oriented p-n structure. The depletion capacitance reduces with an increase in reverse bias voltage. It is because continuous depletion of charges with applied voltage reduces the available free carriers at the junction.

The calculated resistance for the single operated p-n junction is 0.68-Ω.cm and the value of capacitance at 6 V reverse bias reaches up to 4-pF/cm. The intrinsic bandwidth ($f_{3dB}= 2\pi RC_D$) of the proposed phase shifter reaches up to ≈ 58 GHz at 6 V reverse bias. In the ideal condition i.e. with zero termination impedance, the value of RC time constant will not be affected with change in length, it is simply because the overall product of resistance (in Ω.cm) and capacitance (in pF/cm) is independent of the device length. However, in order to mimic the practical device response, we consider a termination impedance which makes this product heavily dependent upon the length of the device. In Fig. 5.2 (b), f_{3dB} bandwidth is plotted as a function of device length when it is terminated with 50 Ω impedance. It shows that high bandwidth can be achieved with shorter device length but at the same time it will degrade the overall device performance (intensity modulation) due to the insufficient relative optical phase shift at the MZI output.

The optical mode characteristic as a function of the voltage at 1550 nm wavelength is plotted in Fig. 5.3. A small forward voltage is applied in such a way that it does not cross the built-in potential of the p-n junctions. It is ensured by calculating the current which is less than 8 µA at a small DC bias of 0.5 V. As given by equation 1 and 2, the optical effective refractive index increases with an increase in reverse voltage. The relative change of the effective index is large for the small applied bias and gradually reduces as we moved to higher

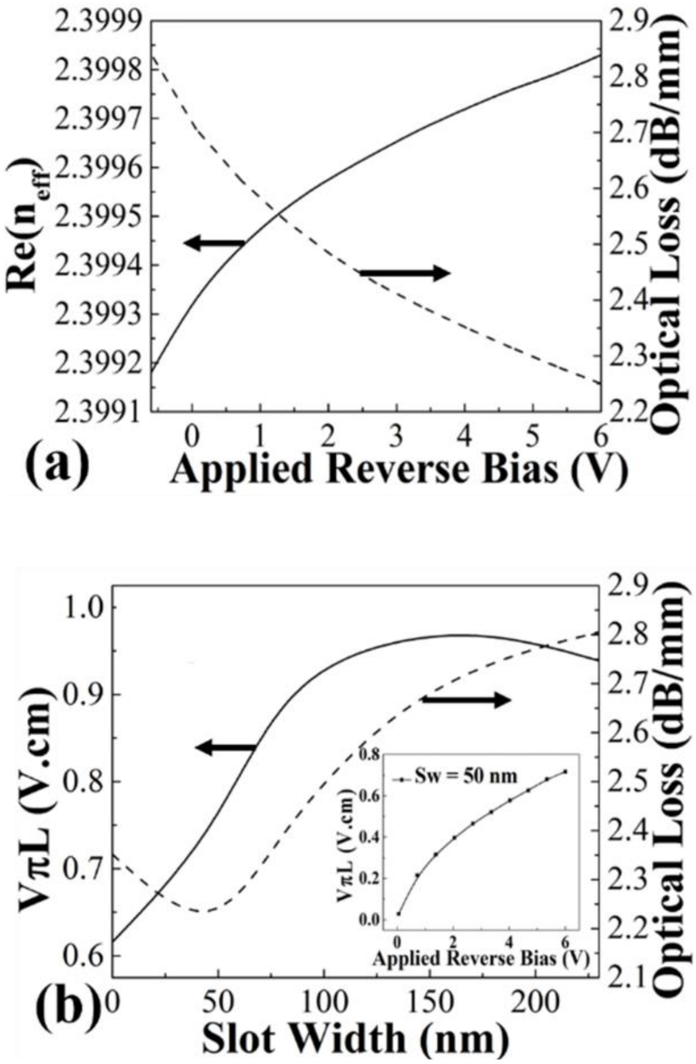

Figure 5.3Optical mode characteristics at 1550 nm for varying reverse voltage, (a) Change in real part of effective index ($\Delta n = 6.5\times10-4$) attributing phase modulation behaviour and acceptably low optical loss of 2.25 dB/mm at V = -6 V. (b) Low value of VπL of 0.74 V-cm with significant relative phase shift of 180◦ is obtained at DC reverse bias of 6 V for 1.2 mm long device length.

reverse voltage. Since the interaction of the optical wave with active p-n junction heavily depends on the slot width of the structure, thus, we have plotted its dependency on modulation efficiency and optical loss as shown in Fig. 5.3 (b). Interestingly, we found that optical loss first reduces for the slot width increment up to 50 nm and after it starts increasing, that is why the slot width of 50 nm is opted to keep the optical loss at its minimum value. The initial reduction in optical loss is due to the free carrier absorption loss reduces as the light starts confining in the slot region. On another hand, VπL contentiously increases up to ≈200 nm slot width, and a thereafter small

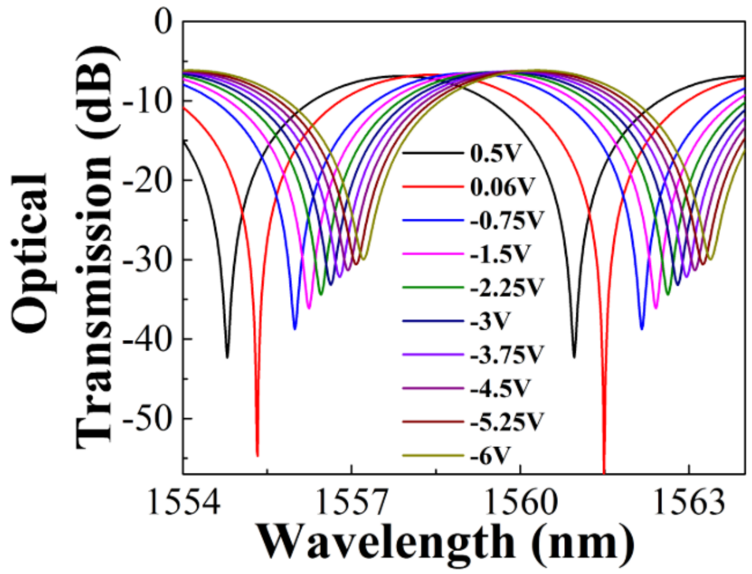

Figure 5.4 Observed red shift in optical transmission spectra for intentionally unbalanced MZI arm for increasing reverse voltage.

improvement in modulation efficiency is observed. This improvement in the modulation efficiency is because optical confinement in both the active region improves slightly after a certain value of slot width. High modulation efficiency of 0.74 V.cm is achieved for the 50 nm slot width at a reverse bias of 6 V as shown in the inset of Fig. 5.3 (b).

To realize the intensity modulation out of this phase shifter, it is incorporated into the intentionally unbalanced MZI configuration where one arm of MZI is 100 µm longer than the other. To obtain the transmission spectra, the long arm of the MZI is connected to the ground whereas a smaller arm is connected to the variable DC supply (from small forward bias to 6 V reverse bias). It causes the appearance of fringes in the wavelength spectrum due to additional path differences in both the MZI arms. Fig. 5.4 shows the optical transmission at the MZI output where maximum Static Extinction Ratio (SER) of 49 dB is observed at a small forward bias of 0.06V. It is simply due to the fact that optical loss in both the MZI arms are equal at this bias voltage. The value of SER reduces to 23 dB when a high reverse bias of 6 V is applied across the junction. The observed FSR (Free Spectral Range) and insertion loss of the modulator are 6.1 nm and 6 dB respectively. The obtained insertion loss also accounts for the coupling loss of 2.5 dB when light couples into the device. However, the value

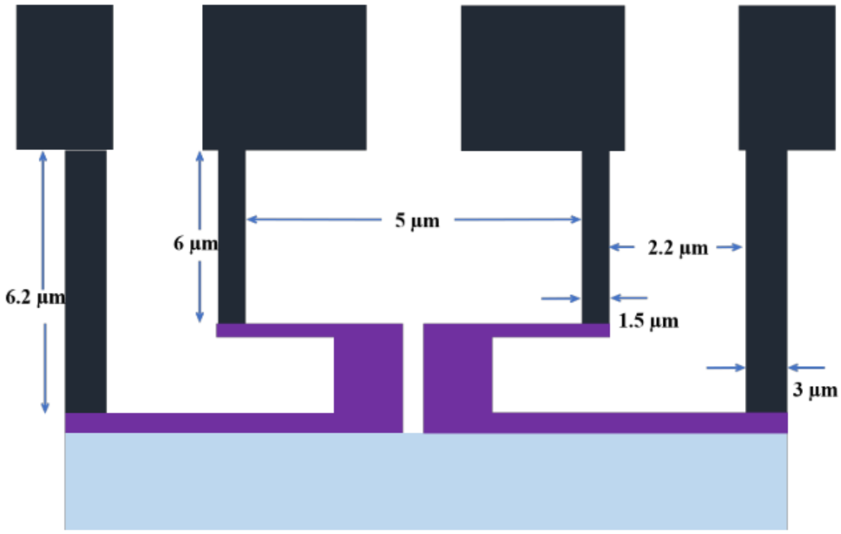

Figure 5.5 Designing of TW electrode for the proposed device on top of SOI, top SiO_2 cladding is not shown for the clear view of electrode designing.

of insertion loss can be reduced to lower values with a light doping profile in the waveguiding region but at the cost of poor modulation efficiency. It is due to the fact that low doping concentration will result in a low optical loss in the modulator and thus low insertion loss can be achieved. [35]

5.3.2 Traveling-Wave Formation

The modulation bandwidth of the TW modulator is mostly affected by the three parameters as already discussed in the previous chapter; 1) Index mismatch between RF effective index (N_{eff}) and optical group index (OGI) (to achieve efficient phase modulation). 2) Impedance matching between characteristic impedance of device with source and termination impedance. 3) and RF loss. Designing of TW electrodes as a co-planner waveguide for the proposed modulator is shown in Fig. 5.5.

Frequency-dependent RF characteristics are plotted in Fig. 5.6. In agreement with the previous studies, microwave effective index (N_{eff}) decreases and microwave loss increases with an increase in RF frequency as shown in Fig. 5.6 (a). It suggests that a lower value of the optical group index is needed to achieve a strong velocity match between optical and RF modes at higher RF frequencies. It is because small index mismatch severely affects the modulation bandwidth as follows $f_{3dB\,(\max)} \propto c/4(n_m - n_0)$. Fig. 5.6

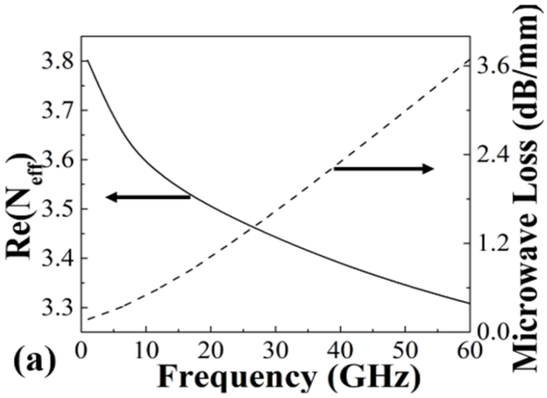

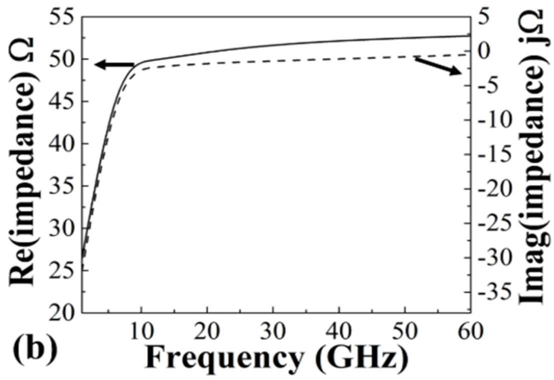

Figure 5.6 Microwave effective index and microwave loss as a function of RF frequency at S_w = 50 nm. (b) Real and imaginary part of characteristic impedance; Impedance lies near 50 Ω at higher microwave frequencies that helps to avoid reflection at the source and termination of the device.

(b) shows device characteristic impedance increases rapidly for lower RF frequencies and later its value remains near to 50 Ω for the given TW electrode configuration. The dependency of OGI on rib width for various slot width combinations are plotted in Fig. 5.7. With the help of engineered device design, the lower value of OGI can be obtained for smaller rib width and wider slot width and it becomes saturated for larger rib width. For the proposed device, OGI of 3.33 at S_W = 50 nm is obtained that matched well with microwave effective index at a higher RF frequency of 48GHz. ere it should be noted that the wider slot width can help in improving index matching between RF and optical modes at higher microwave frequencies but at the cost of poor modulation efficiency.

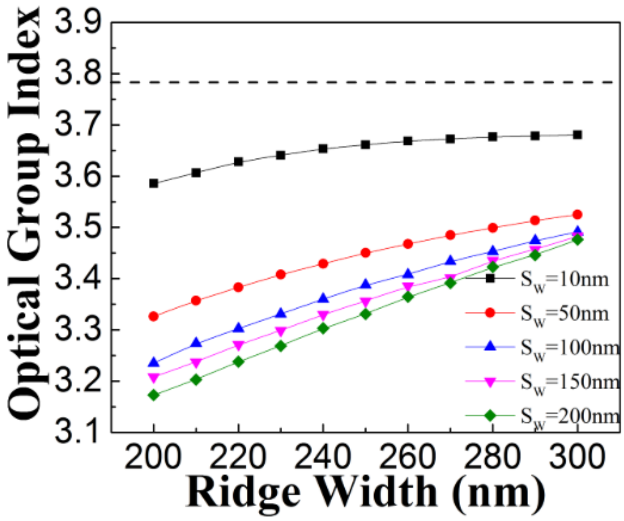

Figure 5.7 Optical Group Index dependency on ridge width for various slot width combinations, dashed line shows the value of OGI for a 500 nm ridge width on 220 nm thick SOI platform.

5.3.3 Speed Analysis

The dynamic performance of the device can be calculated when alternating swing voltage (V_{pp}) is applied in addition with the DC bias to the one arm of MZI whereas another arm is fixed to the forward bias of 0.5 V. High stream data bit sequence is generated using PRBS (pseudorandom bitstream) with a pattern length of $2^{32} - 1$. The dynamic responses are measured for both the cases i.e. without TW configuration and with TW configuration as shown in Fig. 5.8. The data rate of 25 Gbit/s is obtained at a termination impedance of 50 Ω for 600 μm long device without TW

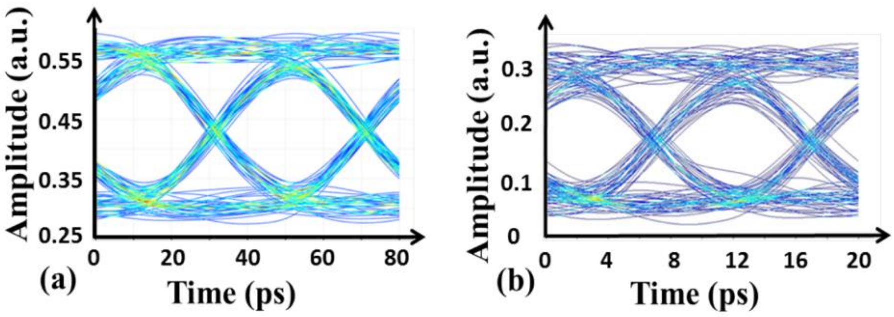

Figure 5.8 Calculated eye diagram at λ = 1550 nm, (a) 25 Gbit/s data rate obtained with lumped electrodes at V_R = -2.5 V and V_{pp} = 6 V, (b) 100 Gbit/s data rate obtained with TW electrodes at V_R = -2 V and V_{pp} = 5 V.

Table 4 Performance parameter comparison of different depletion type Mach-Zehnder Modulator with proposed work

Type of Junction	**λ (nm)**	**Data Rate (Gbit/s)**	**ER (dB)**	**VπL (V.cm)**	**IL (dB)**
Lateral [216]	1550	90	2.7	1.4	5.4
Interleaved [139]	1550	40	4.7	3.1	3.5
U-shaped [91]	1310	24	2.2	0.46	2.7
Lateral [217]	1550	25	4.1	2.4	6.7
Vertical [90]	1550	28	5.8	1.86	4.2
Vertical (This work)	1550	100	2.4	0.74	6

electrode configuration. An extinction ratio of 2.6 dB at a DC reverse bias of 2.5 V and 6 V_{pp} swing voltage is achieved as shown in Fig. 5.8 (a). The reason behind this low extinction ratio is insufficient phase shift (due to short device length) which is required to produce constructive and destructive interference at the MZI output. The estimated value of energy consumption per bit is 4.2 pJ/bit at 25 Gbit/s. Here it should be noted that the DC bias of 2.5 V is applied in such a way that the overall signal doesn't cross the built-in potential of the junction. Moreover, to improve the speed performance and energy efficiency, the TW electrode configuration is considered. By taking the advantage of high index matching between the RF and optical mode at 48 GHz RF frequency, a clear eye-opening with 2.4 dB extinction ratio with energy consumption of 1.3 pJ/bit is achieved for 100 Gbit/s data rate as shown in Fig. 48 (b). This extinction ratio can be improved by applying high amplitude swing voltage but at the cost of additional power consumption. The performance of the proposed modulator is compared with the other reported work as listed in Table.4. The proposed engineered design enables us to achieve high-speed performance along with high modulation efficiency simultaneously.

5.4 Summary

In summary, the improved mode coupling with the vertically aligned active p-n junction improves the modulation efficiency. On top of that, split p-n junctions in lateral direction enable the two-pronged benefit of reducing RC time constant and improving strong light coupling (due to velocity match) with

RF mode using TW electrodes. The low $V_{\pi}L$ of 0.74 V-cm with an intrinsic bandwidth of ≈ 58 GHz is obtained for the proposed phase modulator without any TW configuration. The data rate of 25 Gbit/s with an extinction ratio of 2.6 dB is reported using a lumped electrode connected to the device. Further improvement in the high-speed operation is obtained with the application of the TW electrode which is not being limited by the RC time constant. Confinement in the low-index region gives the extra privilege to match the velocity between RF and optical modes at higher microwave frequencies. With the given advantage of engineered modulator structure, a high data rate of 100 Gbit/s is obtained with an extinction ratio of 2.4 dB using the TW electrode. The proposed modulator with its engineered structure in Si can find applications in optical fiber communication and optical interconnects.

Chapter 6 Comb-like asymmetric grating for thermally stable integrated photonic devices

6.1 Introduction

Integrated silicon photonics has been playing a major role in a myriad of applications including electro-optic modulation [18,35,36,40,68,90,134], multiplexer/de-multiplexer [144], memory devices [155,165,166] and biochemical sensing [167–170]. Among them, label-free optical bio-sensing on silicon-based CMOS compatible platform is gaining a lot of interest due to its low manufacturing cost, mass production, small footprint area, and high sensitivity [171–173]. Numerous on-chip optical sensors based on various structural geometry and principle have been developed, e.g., Micro Ring Resonator (MRR) [174–176], Interferometry type structure [177], Sub-Wavelength Grating (SWG) based structure [163,178] and photonic crystal-based sensors [179]. An MRR based sensor on silicon is mostly used that has an advantage of high Quality-factor (Q) and smaller footprint area but it usually suffers from the two major disadvantages of high-temperature dependency and small Free Spectral Range (FSR) operation due to the phase-dependent resonating structure [180,181]. However, mode splitting of whispering-gallery-mode along with high Q factor in MRR has shown its potential to be used as less temperature-sensitive for sensing applications [182–184]. Also, Mach Zehnder Interferometer (MZI) based sensor shows wide operational optical bandwidth and athermal characteristics, but at the cost of a larger footprint area that is needed to achieve adequate phase-shift response [177]. Apart from the silicon-based sensor, some advanced materials can also be used to enhance the sensitivity of the device [185–187]. Several ways can be adopted to improve the sensing performance of the device: I) Strong light-analyte interaction helps to improve the sensitivity of the device, II) Q factor significantly affects the device performance; high Q will result in narrow FWHM but device characteristics become vulnerable in presence of external noise or temperature variation. III) The small footprint of the device plays a major role in cost-effective and fast responsive devices and IV) Small value of FSR limits the selection of analyte (for a large change in analyte refractive index) present in the cladding, especially in the case where multiple resonance peaks are present simultaneously.

Unlike the silicon-based MZI and MRR structures, SWG based structure can be designed to achieve desirable optical characteristics due to their arbitrary but controllable properties. In most of the grating-based sensors, the change in the analyte index is calculated by observing the shift in the transmission dip where the center of the dip lies at the Bragg wavelength ($\lambda_B = 2\Lambda n_{eff}$) [188,189]. To achieve the narrowband transmission peak, several millimeter-long devices are required which is not suited for the dense on-chip integration and shows high-temperature dependency as well. Other issues with the conventional grating structures are the multiple side lobes on both sides of the resonance peak that makes filtering unreasonably for sensing applications. To get rid of these issues, various structures on silicon have been investigated to improve the performance of the device that includes quarter-wave gratings, sampled gratings, chirped grating profile, and superstructure gratings. In the past few years, asymmetrical Bragg gratings engraved on silicon have been promising due to their unique optical characteristics. However, such devices still suffer from the narrow FSR issues which limit the sensing capability to detect a variety of material on a single device [178,190,191].

In the proposed work, two different grating periods at each side of the cavity section helps to achieve a single transmission peak with a high extinction ratio of 20 dB. The device design is optimized in such a way that fundamental mode and first-order mode should propagate simultaneously in the partially etched gratings forming two different band rejection windows centered at the distinct positions in accordance with their respective effective refractive indices. The proposed device allows only a small transmission peak of 1.8 nm FWHM in between these two rejection windows for a small footprint area of 18 μm^2 only. Thermal stability behavior of the output characteristic is observed by operating device at different temperature values which shows that the proposed device exhibits satisfactory performance even with typical thermal variations $\approx \pm 15$ K. Our numerical analysis predicts that large FSR characteristics of at least 80 nm are obtained with the proposed approach. Deeply etched gratings in the lateral direction govern the way to achieve strong light-analyte interaction. With the help of strongly coupled fundamental mode and leaky first-order mode, the sensitivity of 352 nm/RIU is achieved for a different concentrated NaCl solution from 0% to 10% in the Deionized (DI) water.

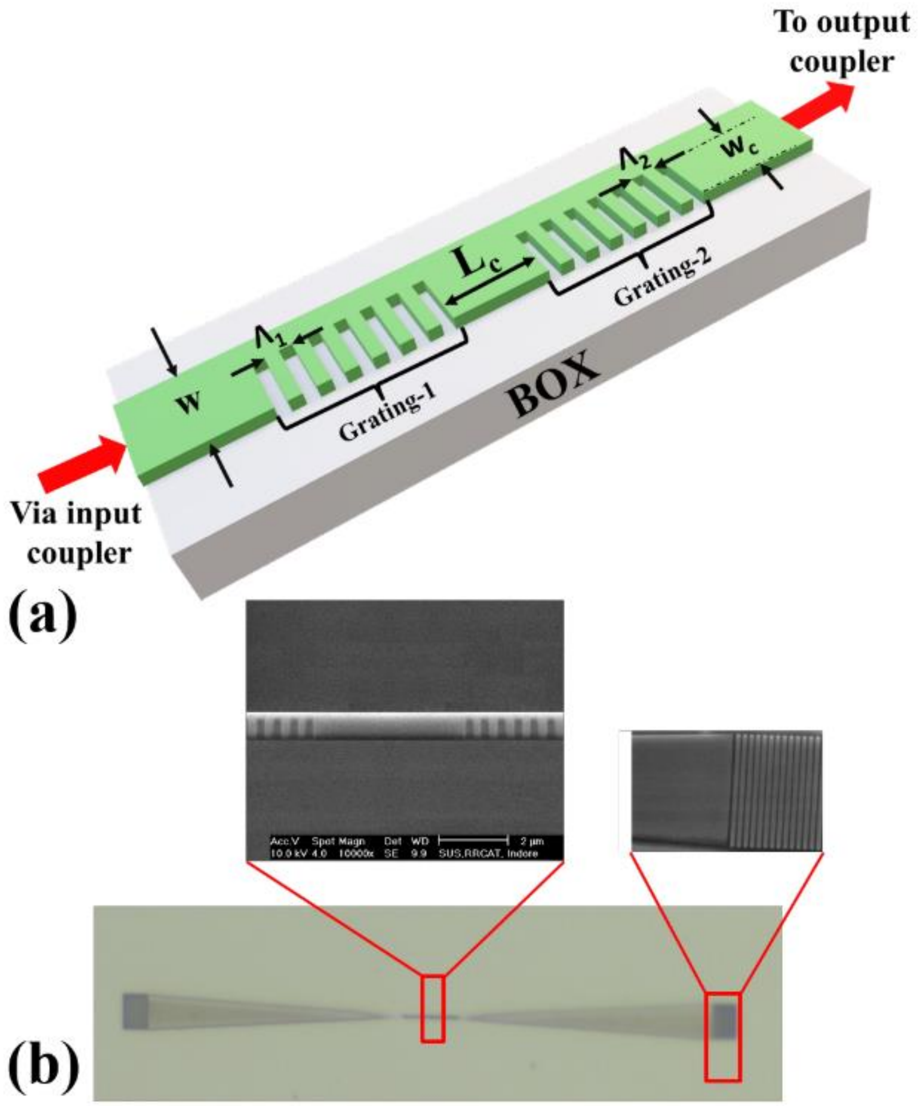

Figure 6.1 (a) Schematic of the device fabricated on SOI wafer of 2 µm thick BOX layer and top silicon thickness of 220 nm. The red arrow shows the in and out coupled light in the device. (b) Optical microscopic view of the device with connected in/out grating coupler; inset shows the SEM view of the gratings, cavity section, and coupler.

6.2 Device design and fabrication

The 3-dimensional schematic of the device is shown in Fig. 6.1 (a). Two sets of gratings having distinct periods are separated by a cavity section. The period of both the gratings and duty cycle are Λ_1 = 380 nm, Λ_2 = 386 nm, and 55% (for both gratings) respectively, whereas the width (w) and corrugation width (w_c) of the gratings are 750 nm and 565 nm respectively. The width of the device is chosen in such a way that it supports at least two modes of operation (fundamental and first-order modes). Single transmission peak in between two photonic band gaps caused by these modes is engineered by varying the grating etch depth in the lateral direction for given grating parameters. The cavity section of length 4.5 μm in between two sets of gratings plays an important role to achieve narrowband spectral characteristics. It is because the efficient coupling of various modes will depend on the incident phase of light at the second set of the grating (after passing it through the cavity section). **The partial etching in the lateral direction is used to break the symmetricity of both the grating sets that offer the enhanced coupling between the fundamental and first order modes.** To ease the measurement process and for efficient coupling of the light into the device, input and output grating coupler is used at both the side of the device. The fabrication of the device starts with the coating of negative tone Electron-beam Lithography (EBL) resist (HSQ-A) over the cleaned top-silicon layer. Electron beam exposure is used to pattern the desired structure. After patterning the resist, 4 min development process followed by the rinse in DI water removes the unexposed soft resist from the sample surface. Fluorine based chemistry is then used to etch the open silicon surface using the RIE process. Fig. 6.1 (b) shows the microscopic (top) view of the full-length fabricated device where inset shows the Scanning Electron Microscope (SEM) image of the selected area.

6.3 Propagation and filtering characteristics

The width of the device is deliberately designed to support fundamental and first-order modes. For this reason, first, we calculated the cut-off values for each mode as a function of waveguide width (w). Fig. 6.2 shows the

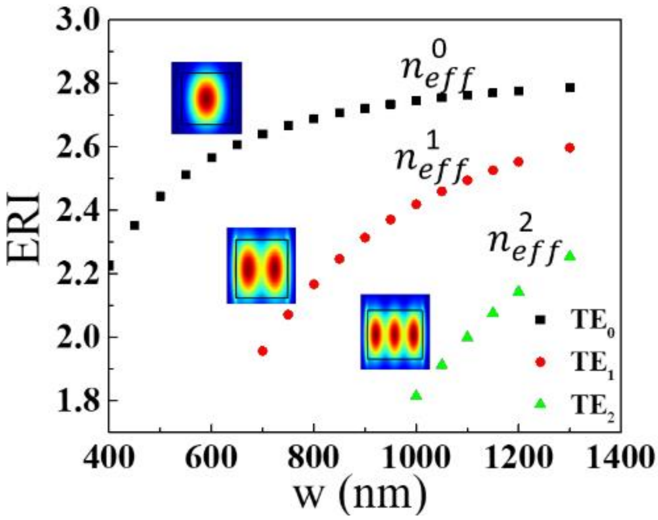

Figure 6.2 Dependency of effective refractive index (ERI) on waveguide width (w) for TE modes only. Optical mode pattern for each mode is shown at λ=1550 nm. n_{eff}^{0}, n_{eff}^{1} and n_{eff}^{2} represents the value of ERI for fundamental, first order and second order modes, respectively.

variation in the Effective Refractive Index (ERI) of various modes as a function of the waveguide width by assuming DI water as a top cladding material. The values of ERI increase rapidly near the cut-off width (for any mode) and later its increasing slope reduces when we move towards wider width dimensions. It is simply because the increase in the device width will result in strong confinement of modes in the waveguide, but confinement will saturate after reaching enough width dimensions. The calculated cut-off value for first-order modes is found near w ≈ 650 nm whereas second-order mode appeared after w≈ 1000 nm. Assume that fundamental mode and first-order mode are having ERI of n_{eff}^{0} and n_{eff}^{1} respectively. As we know higher-order mode has weak confinement as compared to the fundamental mode, it induces small value of ERI for the first-order mode as compared to the fundamental mode in the waveguide (n_{eff}^{0}> n_{eff}^{1}). These different values of ERI will result in the distinct phase velocity of both the modes propagating in the device. When these modes interact with the individual set of gratings, the coupling between the various modes in the propagation and counter propagation direction occurs.

The loss for higher-order mode will be larger as compared to the fundamental mode. The calculated loss for TE_0 and TE_1 modes is ≈ 2 dB/cm and

≈ 6 dB/cm respectively. However, the length of the device is very small that will not affect the overall coupling of the various modes present in the waveguide. In the previous studies of these Bragg grating kind structures, ultra-narrow bandwidth is achieved by utilizing the scattering matrix as [192]

$$S = \begin{vmatrix} \pm r_g & jt_g \\ jt_g & \pm r_g \end{vmatrix} \tag{6.1}$$

where t_g and r_g represent the transmission and reflection coefficient of the perturbation, respectively. However, due to phase-dependent grating attributes (φ_g), it is not possible to achieve large FSR characteristics and such gratings are difficult to fabricate as it needs long uniform structure either using MRR or using FP cavity section. In our proposed design, we have chosen cavity coupled two-period gratings with asymmetrically placed sidewalls that are formed by partial etching of Si ridge in the lateral direction. These comb-shaped gratings not only ease the fabrication process but also makes the device highly compact. To implicit the device working, the transmission spectrum for individual gratings set is calculated by considering that only one set of the grating is present at a time between input and output.

Device simulation is performed using the commercially available simulation package [46]. The 3D Finite Difference Time Domain (FDTD) method is used for simulation because the structure is not symmetric in propagation direction and it gives accurate results that mimic the practical device behavior. However, for the fast calculations, initially, we used a 2.5D FDTD method for the optimization which gives a better approximation of the various device's parameters. Auto nonuniform mesh used in the simulation to provide the high accuracy of results with less computational time and memory. The device is surrounded by a PML (Perfectly Matched Layer) boundary condition that allows the absorption of optical waves with minimal reflections.

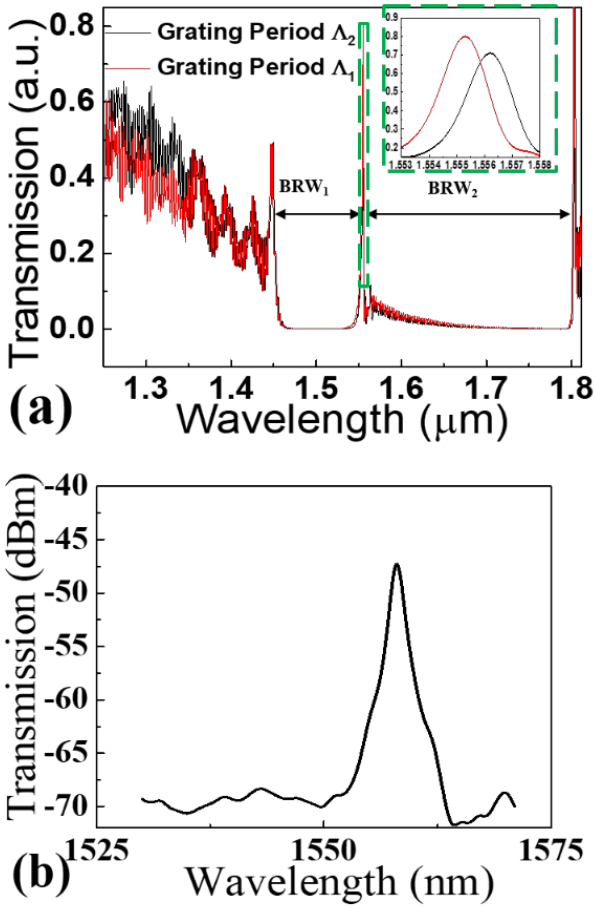

Figure 6.3 Calculated transmission spectra for individual set of gratings at the output of device. Inset shows the magnified view of area given in green dashed box. Shift in the transmission spectra for red and black colors are due to distinct grating periods of Λ_1 = 380 nm and Λ_2 = 386 nm respectively. (b) measured optical transmission of the device with DI water as a cladding material at the room temperature.

In Fig. 6.3 (a) formation of two band rejection windows (BRW_1 and BRW_2) separated by a passband window can be seen due to different value of ERI of both the modes i.e. n_{eff}^{0}, n_{eff}^{1} forming two photonic bandgaps that result in the formation of these BRW in accordance with $\lambda_B = 2\Lambda n_{eff}$. Since the period of the second set of gratings is different from first, shifted response between both the individual transmissions spectra can be observed as shown in the inset of Fig. 6.3 (a). However, when we integrate both the gratings together using the appropriately long cavity section, only the common passband of both the gratings will appear at the output and the remaining signal will be either reflected from the input side or will be radiated to the slab/cladding of the

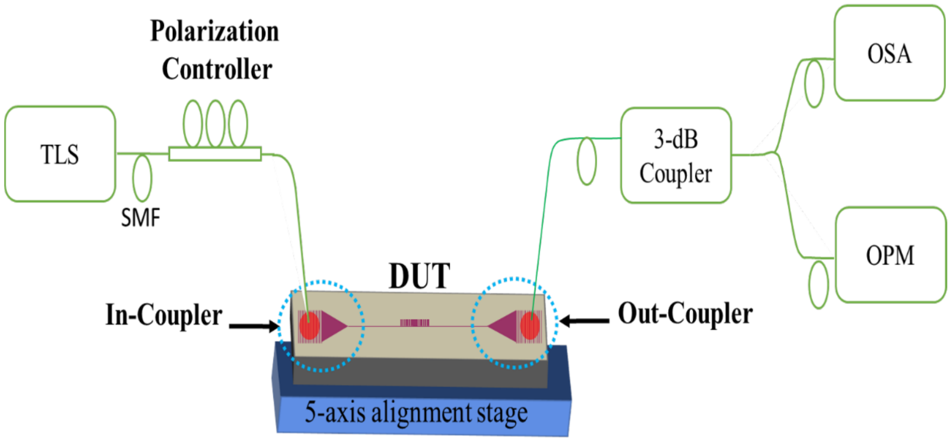

Figure 6.4 Experimental setup to analyze optical spectral characteristics of Device Under Test (DUT). Output power from out-coupler grating is split into two equal parts to feed optical spectrum analyzer (OSA) and optical power meter (OPM) simultaneously.

waveguide. Since both the gratings used in the device will lead to having a different location of the resonance peaks and thus common output from both the gratings have narrow FWHM characteristics which can be tailored by optimizing the different grating periods. Numerical calculation predicts that the proposed device is having large FSR output characteristics due to a wide photonic bandgap of $BRW_1 \approx 80$ nm and $BRW_2 \approx 270$ nm. It implies that a high FSR value up to 270 nm can be obtained with the proposed filter. The introduction of the cavity section in between these gratings plays an important role to achieve a high narrowband transmission peak. It is due to the fact that the appropriate length of the cavity section removes any phase discontinuity at the second set of gratings and thus desired spectral characteristics can be achieved.

The experimental measurement setup is shown in Fig. 6.4. Five-axis alignment stages were used to precisely align the optical fiber with the input and output grating couplers. Light from Tunable Laser Source (TLS) is used to feed optical input to the device through an in-grating coupler after passing it through Polarization Controller (PC). Out-coupler light is collected through the fiber and is connected to the Optical Spectrum Analyzer (OSA) to analyze the output spectral performance. The measured value of the transmission peak is having a high extinction ratio of 20 dB with a narrow

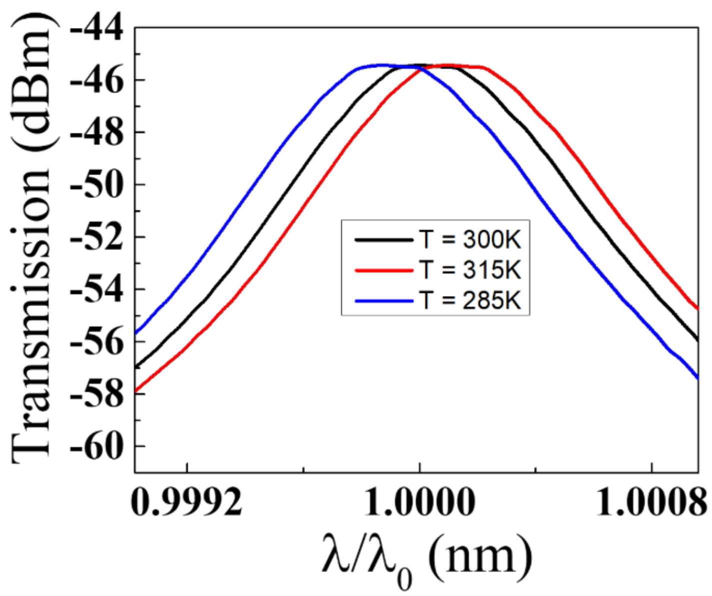

Figure 6.5 Temperature dependent optical characteristics over the wavelength. λ_0 represents the peak resonance wavelength. Maximum permissible thermal variation is obtained in such a way to keep resonance peak intensity constant.

FWHM of 1.8 nm at the output of the device as shown in Fig. 6.3 (b). As compared to the conventional Bragg gratings which require millimeter size device length, the proposed device attributes narrow passband for a small footprint area of 18 µm^2 only. Here it should be noted that further narrower FWHM can be achieved by increasing the number of periods. It is simply because the slope of the edges of the peak increases with an increase in the number of periods but at the cost of degraded FSR and thus poor thermal resistant characteristics.

We have also measured the temperature dependence of optical characteristics as plotted in Fig. 6.5. The device exhibits highly thermal stable characteristics, plotted optical characteristics for different temperature ranges allows temperature variation of ±15 K with respect to room temperature of 300 K. Here, the obtained resonance peak shift is further used to calculate a thermo-optic coefficient for silicon at room temperature. The obtained value of $\Delta n/\Delta T = 0.00017K^{-1}$ is in close agreement with previously reported work [57]. Here it should be noted that the value of n with varying temperatures is considered in

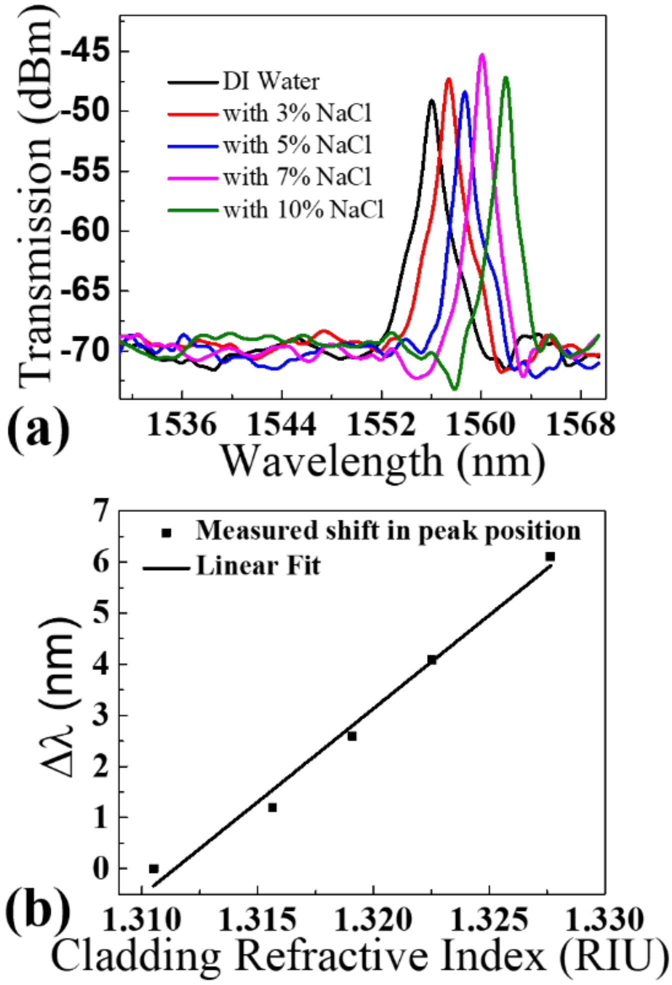

Figure 6.6 Measured optical characteristics of 24 μm long device with top cladding material as different concentration NaCl solution in DI water. Observed wavelength shift of ≈ 6 nm is achieved when NaCl concentration changes from 0 % to 10 %.

accordance with the previous studies [57,193]. To verify the change in the refractive index of the analyte with varying temperature, numerical calculations were performed that uses the resonance peak shift and it matches well with the calculated peak shift for varying temperature values. It does not only make device operation thermally stable but also makes it less dependent on external noise.

6.4 Sensing characteristics

In order to achieve high optical confinement in the cladding region, partially etched gratings in the lateral direction are incorporated in the given

Table 5 Performance parameter comparison of various previously reported sensing device.

Device Type	Active area (in μm2)	Sensitivity	Q value	Sensing material
Racetrack Grating [187]	314	429 nm/RIU	9800	Glycerol
Ring, SWG [167]	114	390.4 nm/RIU	800	NaCl
End-Fire Ring [168]	80	487 nm/RIU	7×10^5	Nanoparticle
Strip, MZI [169]	8000	1730 (2π)/RIU	–	NaCl
Ring, SWG [172]	80	363 nm/RIU	12900	Glucose
This work	18	352 nm/RIU	860	NaCl

comb-shaped grating structure. Strong confinement in the cladding region will lead to a larger wavelength shift with a change in the cladding Refractive Index (RI) and thus enhanced sensitivity can be achieved. The shift in wavelength with a change in cladding RI can be given as [194,195]

$$\Delta\lambda = \Delta n_c \Gamma_c \frac{\lambda_{res}}{n_{eff} - \lambda \frac{\delta n_{eff}}{\delta\lambda}} \tag{6.2}$$

$$\Gamma_c = \frac{\iint_{Cladding} \phi(x,y)dxdy}{\iint_{Total} \phi(x,y)dxdy} \tag{6.3}$$

where Δn_c is the change in cladding refractive index and Γ_c represents confinement of light in the cladding region.

In the proposed device design, higher-order leaky mode privilege device to have strong interaction between optical modes with the analyte. Since device parameters are optimized by assuming DI water as a top cladding material. Hence to simply examine device sensitivity with a change in cladding RI, different concentration of NaCl solution (0%-10%) in the DI water was used as a top cladding material. Fig. 6.6 (a) compares the optical tunable characteristics for different concentrated NaCl solution at room temperature. In this figure, the redshift of resonance peak is observed with an increase in the concentration of NaCl in DI water. The estimated change in RI with NaCl (x%) mix DI water can be calculated mathematically as $n_{eff} = 1.3105+0.0017151\times x\%$. By utilizing this relation, high sensitivity of 352 nm/RIU is measured as shown in Fig. 6.6 (b). A comparison of the sensing characteristics of this work with other studies is presented in Table 5. In comparison to the MRR based structure, the proposed device is fabricated on a smaller footprint area of 18 μm^2 only and demonstrated high sensitivity as well. We also emphasize that unlike the MRR based structure proposed device is free from any FSR limit and shows thermally stable behavior due to low Q value attributed from device characteristics. However, at the same time, low Q value will also bound the smallest possible Detection Limit (DL) which is the trade-off between the DL and thermal stability behavior of device which can be further improved with the more optimized structure geometries. With the advantage of area compact and high-sensing performance, the proposed device is best suited for the highly-dense on-chip integration for the next generation bio-medical sensors.

6.5 Summary

An integrated optical filter based on a comb-like grating structure with a cavity section is proposed, fabricated and measured. Partially etched grating in the lateral direction causes asymmetrically placed sidewall in the grating region that ensures non-zero coupling of fundamental and first-order mode in the co-propagation and counters propagation direction. Narrowband transmission peak of 1.8 nm FWHM for a wide wavelength range is achieved using opted device dimensions that are due to the presence of single passband in between the two band rejection windows. Unlike the MRR based sensors, we have also demonstrated the thermally stable optical characteristic of ±15 K that makes optical characteristic prone to ambient noise and thermal variations. In the proposed device structure, higher-order leaky mode characteristic governs strong coupling between the light and analyte present at the cladding. Sensing characteristics is performed using a different concentration of NaCl solution present in the cladding region of the device. Measured results indicate a high sensitivity of 352 nm/RIU which is 5 times better than the simple strip-type structure. Single transmission peak output of the device makes it apparently free from any FSR limit. The proposed device governs a way to achieve a highly compact on-chip filter with a single peak output characteristic and can be used for a variety of applications in integrated photonics.

Chapter 7 Tapered cavity coupled asymmetric grating for electrically tunable devices

7.1 Introduction

The demand for high bandwidth interconnects at the datacenters has carried out the research and development on terahertz interconnect technologies [196–198]. The CMOS-compatible silicon-based electronic-optic (EO) modulators offer the most viable solutions as they facilitate the integration of area efficient and high-speed optical transmitters and receivers with numerous multiplexing schemes at cheaper price [18,199]. Moreover, the EO-modulator can also be integrated with the dense wavelength division multiplexing (DWDM) technique to enhance the capability of the communication system. In a few past years, a significant amount of work is reported towards improvement in the DWDM techniques that include advance modulation schemes[200], laser-driven photonic transmitters[201,202], low crosstalk AWG network, etc.

Among the various structures' geometry, micro-ring resonator (MRR) based structures are widely used to achieve a multi-resonant optical spectrum with its electrically tunable optical characteristics. There are multiple advantages associated with this resonant structure like narrow spectral resonant width, low power hungriness, and highly compact footprint area that makes it an attractive choice for optical modulator[203,204]. However, several issues also exist with MRR like free spectral range (FSR) bounded spectrum (due to phase-dependent resonance characteristic)[205], high thermal dependency[206] and drift in resonant peak with applied bias[207] that limit the overall capacity of the system when used for the DWDM application. Bragg grating engraved on silicon has been widely explored to investigate tailorable optical characteristics that can be integrated with other on-chip photonic devices to achieve more advanced functionalities[208,209]. The main advantage linked with the Bragg grating structure is its FSR free optical characteristic that cannot be achieved with MRR based resonant structure[180,210]. In most of the Bragg grating-based structures, transmission dip at the resonance wavelength is realized at the output spectrum. The position of the transmission dip depends on the effective refractive index

(ERI) of the optical mode that can be given as $\lambda_B = 2\Lambda n_{eff,}$ where λ_B, Λ and n_{eff} represents the Bragg wavelength, period and ERI of the optical mode respectively. A myriad of functions has been implemented with the Bragg grating-based structure like sensing[163,211], modulation[18], multiplexing/de-multiplexing[212] and beam steering[213,214]. Some disadvantages coupled with the conventional Bragg grating structure are long device length, the formation of sidelobes having significant energy, and high thermal dependency which makes it a difficult choice for a variety of applications[178,215].

Asymmetrical grating based on multimode optical signal has emerged as a promising candidate to obtain desirable optical characteristics due to its arbitrary but controllable optical characteristics[190,191]. Recently, we have demonstrated a novel approach to achieve a narrow transmission peak with large FSR attributes in a dual perturbed Bragg grating structure where both sets of gratings were separated by a cavity section[162]. The proposed device was fabricated on a highly compact area of 18 μm^2 and shows high suppression of side lobes near-resonant peak. However, the fabrication of reported devices was complex due to the presence of two different grating periods with nearly equal values. In contrast to the device reported previously, here we propose asymmetrical grating structure having two sets of gratings with equal parameters (period and duty cycle) which is separated by a tapered cavity section. It makes the fabrication process easy as the width optimization is quite easier as compared to the grating period optimization. The fabricated device exhibits a narrow transmission peak of 1.2 nm FWHM with a high extinction ratio of 14 dB. The numerically predicted value of free spectral range (FSR) is greater than 100 nm that makes the device ideal for wide bandwidth applications for the on-chip integrated circuits. We theoretically investigate the optical modulation characteristics of the device when two isolated p-n junctions are doped into each grating section. We have successfully achieved optical modulation characteristics at a fixed value of wavelength with a programmable set of voltages applied across the two junctions. Such zero drift electrically tunability of optical signal is a prerequisite for DWDM applications that have the potential to use in highly efficient optical interconnect and data centers.

7.2 Device design

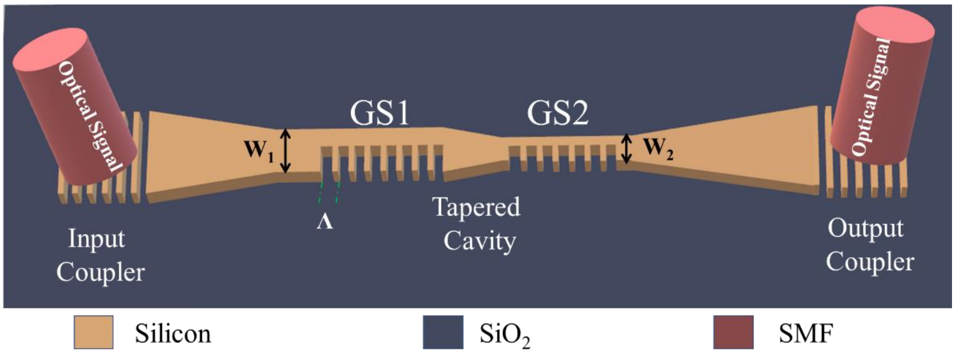

Figure 7.1 Schematic view of tapered cavity coupled asymmetrical grating-based device with input and output grating coupler. The two set of gratings i.e. grating set one (GS1) and grating set 2 (GS2) is coupled with 2 µm long tapered cavity section. The optimized grating parameters for both GS1 and GS2 are Λ = 385 n and, Duty Cycle = 60%. The width of GS1 and GS2 are W_1 = 850 nm and W_2 = 650 nm respectively. Optical signal is feed/collected through single mode fiber as shown in red colour.

The schematic of the proposed device is shown in Fig. 7.1. In order to obtained narrow-band spectral width with a high extinction ratio, the width of both the set of gratings (GS1 and GS2) is chosen such that it allows a shift in the relative spectrum due to distinct ERIs of the optical mode. A small tapered cavity section is introduced in between these set of gratings is beneficial in two ways: (i) it improves the coupling of the optical signal in between two gratings set by avoiding sudden mode mismatch due to distinct width and (ii) its optimized length allows phase matching of the optical signal at the second set of the grating so that single transmission peak can be realized at the output spectrum. The proposed device is partially etched in the vertical direction with an etch-depth of 150 nm, whereas the corrugation width of GS1 and GS2 are 650 nm and 450 nm respectively. The proposed device is designed with a grating coupler at both the side of the device is fabricated that not only offers efficient coupling of light but also ease the measurement process.

7.3 Propagation and filtering characteristics

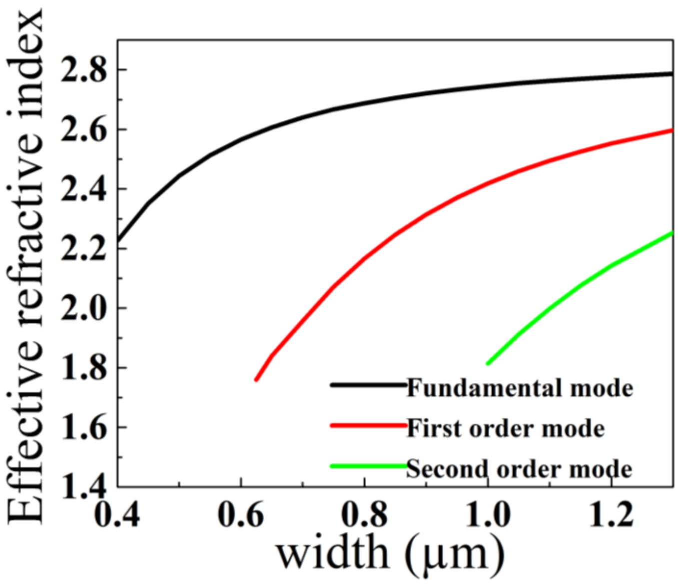

Figure 7.2 Effective refractive indices of optical modes (TE only) as a function of waveguide width of at λ = 1550 nm.

To determine the input width of the device such that it supports at least two distinct modes in the waveguiding region, the number of propagating modes is calculated with varying waveguide width in 220 nm thick silicon waveguide as shown in Fig. 7.2. The appearance of the first-order mode can be seen after the width of 600 nm. It is also clear from the figure that fundamental mode is having the highest value of ERI as compared to the higher-order modes. It is because confinement of fundamental mode is highest in the high index region whereas succeeding higher-order modes becomes more Leakey into the low index media. With the abovementioned reason, the phase constant of these modes ($\beta = \frac{2\pi}{\lambda} n_{eff}$) are different. It results in the distinct phase velocity in the waveguides that causes interaction of these modes in the propagation and counter propagation direction. The position of the fundamental mode and first-order mode is optimized such that it allows a single passband in the spectrum. However, to achieve narrow FWHM with high suppression sidelobes, the second set of grating that has slightly shifted in the transmission spectrum due to smaller width is used.

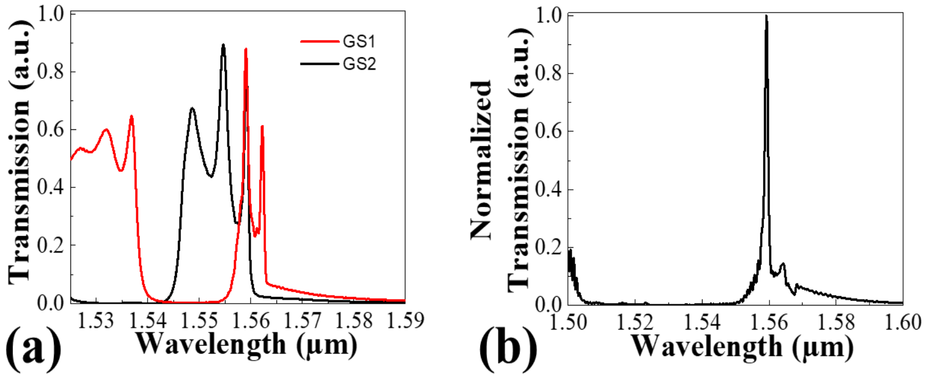

Figure 7.3 (a) Optical transmission for individual set of gratings as a function of wavelength. 2.5D FDTD is used to calculate optical response that gives better approximation of the result with less memory and fast calculation. (b) Simulated optical transmission characteristics for full length device with 3D FDTD method. Single transmission peak observed for wide range of wavelength spectrum.

The simulated optical characteristics are shown in Fig. 7.3. The computation analysis is done using commercially available simulation tools "Lumerical Solution". The behavior of the individual grating set is plotted in Fig 57 (a). As we know that both the set of gratings are cascaded, thus the device will only allow a common optical signal between both the gratings. In Fig. 7.3 (b), normalized optical transmission of the proposed device is plotted. A small bump in the spectrum can be seen at the right of transmission peak. It is due to undesirable overlap between two passband of the transmission spectrum that can be minimized with the more optimized grating parameters.

7.4 Device fabrication and measurement

The fabrication of the device starts with sample cleaning in the piranha solution. Spin Coating of negative tone HSQ resist is performed in two steps: (a) Time: 10 Sec, Acceleration: 100 rpm/Sec, Speed: 500 rpm and (b) Time: 45 Sec, Acceleration: 1500 rpm/Sec, Speed: 4500 rpm. The expected thickness of the HSQ is 80 nm as per the given data sheet with the resist. The coated resist is then prebaked for 2 min at 180^{0}C to smoothen the layer over the sample. Now the sample is ready for the electron beam lithography (EBL) process. The EBL is performed at an aperture size of 10 µm with 10 kV accelerating voltage. The optimized beam current and area dose is 23 pA and 360 µC/cm^2 respectively.

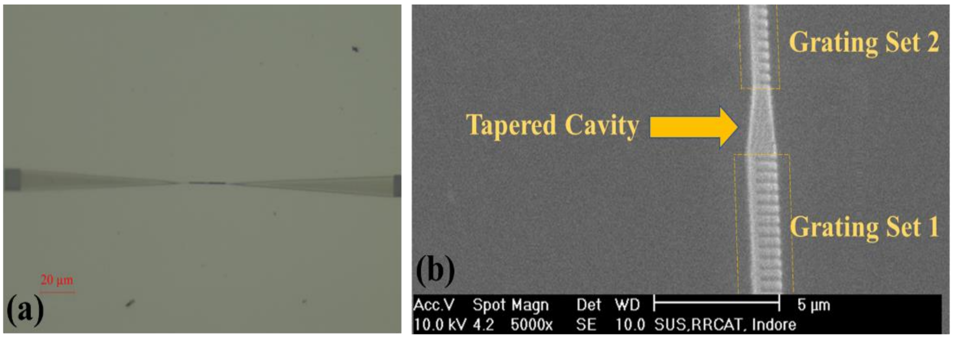

Figure 7.4 (a) Microscopic view of full-length device with connected grating coupler. (b) Scanning electron microscopic view of centre part of fabricated device.

After the 4 min, the development process sample is ready for reactive ion etching. The etching is performed with fluorine-based chemistry with the following optimized parameters: flow rate SF_6:CHF_3::6 sccm:20 sccm, chamber pressure 15mT, forward power 30 W and plasma power of 1000 W. Finally, the hard mask is removed from top Si surface using dip of the sample in a mixture of 3% HF in DI water until the surface is cleaned. Finally, the device is passivated with 2 µm this SiO_2 layer on the top of the device. The microscopic and SEM view of the fabricated devices are shown in Fig 7.4 (a) and (b) respectively.

The real picture of the measurement setup is shown in Fig. 7.5 (a) where inset shows the top view of the device aligned with grating coupler. The optical measurement is performed with a similar setup used in Fig. 6.4 of the previous chapter. The measured optical characteristic of the fabricated device is shown in Fig 7.5 (b). The single transmission peak with a high extinction ratio and narrow FWHM of 14 dB and 1.2 nm is successfully obtained at $\lambda = 1558.3$ nm. The high losses in the spectrum are due to various factors like losses at polarization controller, grating couplers, free space loss, alignment loss, device loss, and losses due to roughness at the fiber tip. The high FSR attributes can be also observed in the measured spectrum in between $1.53\mu m < \lambda < 1.57\mu m$ which is the maximum limit with an available tunable laser source. The measured optical characteristic is in good agreement with the simulated results. However, a small shift in resonance

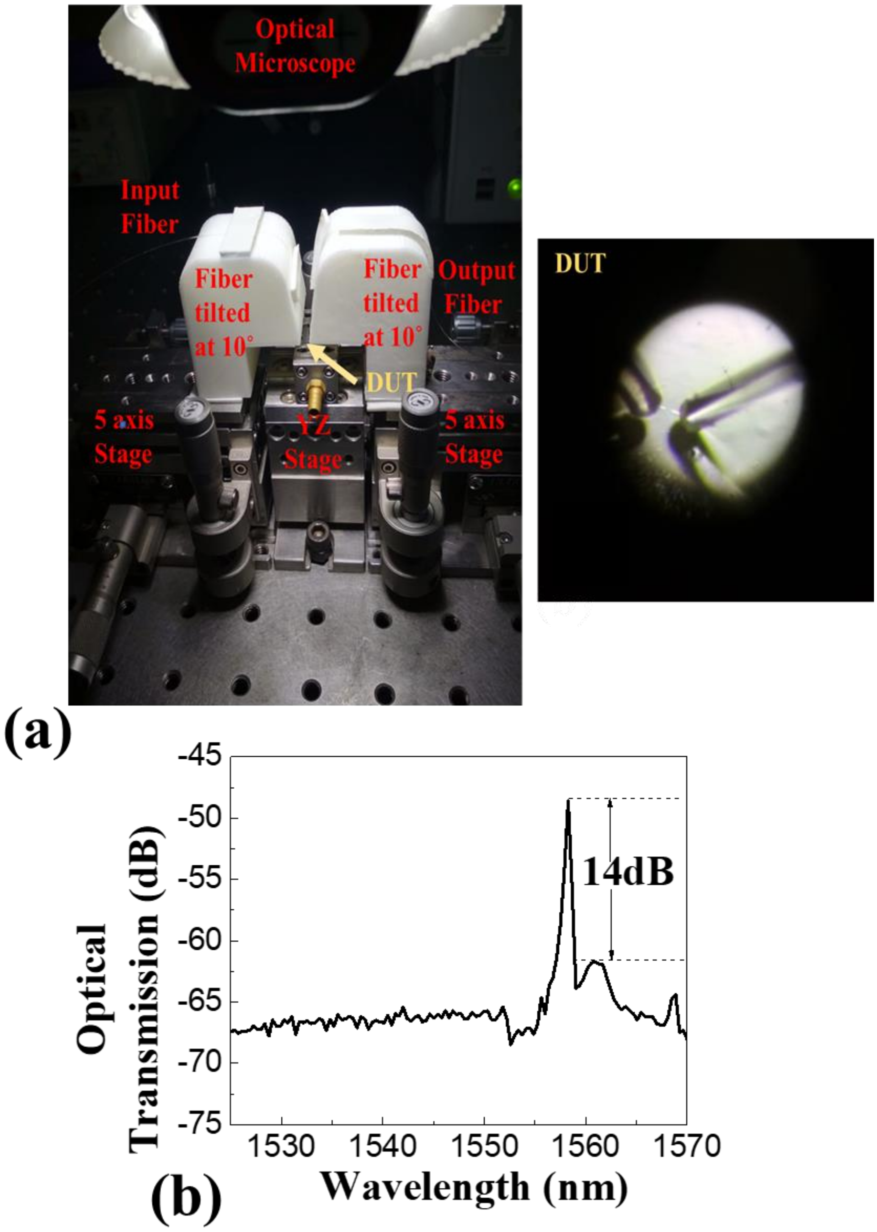

Figure 7.5 (a) Real picture of measurement setup, device is mounted on alignment stages. Optical signal is feed to device at an angle of 10^0 with respect to vertical axis through grating coupler. Inset shows the microscopic view of device and optical fibres aligned across the device. (b) measured optical transmission characteristic of fabricated device in wavelength range of 1.53μm<λ<1.57μm, transmission peak observed at λ = 1558.3 nm.

peak between the simulated and measured characteristics is observed. It may be due to either change in the refractive index of materials as we have taken during the simulation or it may be due to fabrication error such as a change in period or duty cycle.

7.5 Electrical tuning of the optical signal

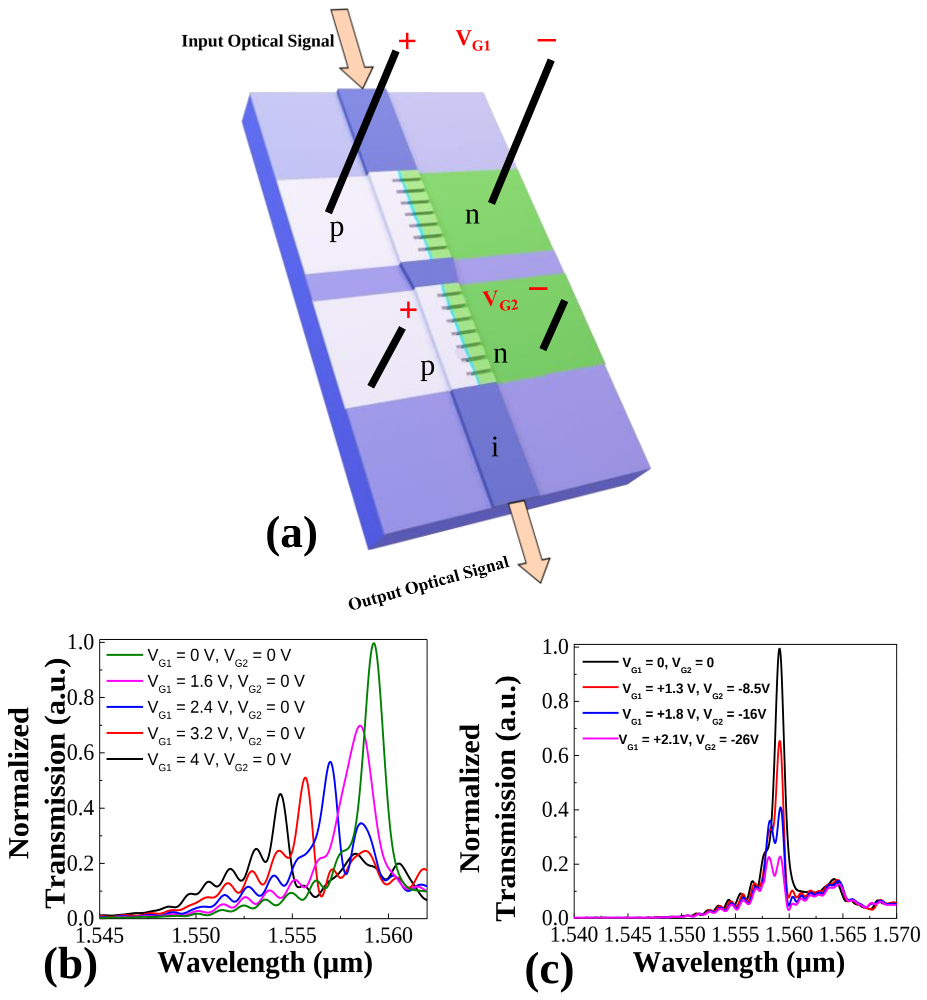

Figure 7.6 (a) Proposed device with embedded p-n junctions, V_{G1} and V_{G2} are applied bias to GS1 and GS2. (b) Simulated electrical tunable optical characteristics under different bias conditions at GS1. Blue shift in peak resonance with decaying intensity obtained for increase in forward bias. (c) Intensity modulation at fixed wavelength of $\lambda = 1.559\mu m$ is achieved with applied different set of voltages.

The electrical tunable optical characteristics of the device are theoretically investigated with the two isolated doped p-n junctions in the structure as depicted in Fig 7.6 (a). Unlike the other p-n doped structure where high doping is not preferred into the optical guiding region due to high optical losses, the high doping concertation is used in the waveguiding region with a high concentration level of 9×10^{18} /cm^3 for n junction and 1×10^{19} /cm^3 for p junction. Since our device has a length of only 22 μm thus high optical loss will not be an issue for such small length devices. High concentration ensures the ohmic contact and reduces the excess resistance at the junction with metal. Both p-n junctions are formed in both sets of gratings where the tapered cavity section acts as an insulator between those junctions. The 70 nm thick slab is chosen for the device that allows easy transportation of free carriers between two electrodes. When junctions are operated under applied external bias, change in the refractive index can be achieved as following the plasma dispersion effect[67], it modulates the optical signal propagating in the active region accordingly.

In this work, optical modulation has been achieved in two different ways. In the first case, a forward bias is applied only in the first set of the grating. Fig. 7.6 (b) shows the modulation of the optical signals with applied bias voltage. Here it should be noted that with applying forward bias to GS1, resonance peak is not only shifting to shorter wavelength but also its intensity reducing continuously. It is with the fact that only one of the resonance spectrums with GS1 is allowed to shift their spectrum whereas another spectrum (GS2) is fixed at their position. Since the output spectrum is cascaded effect of both the gratings thus peak intensity of the resonance wavelength will be decided based on the intersection of both the spectrum at a common wavelength. The shift in the resonance peak is observed in the wavelength range of 1559.16 nm to 1554.36 nm and overall transmission reduced from 100% to 46% when GS1 is operated in forward bias up to 4 V and GS2 is kept grounded. This novel approach to achieve electrically controllable optical characteristics have the potential to achieve a high extinction ratio as compared to conventional resonance-based modulating structures. However, due to applied forward bias, the value of 3dB bandwidth is limited to 4.2 GHz which further can be improved with the lower doping concentration level and small forward bias.

The given approach of the electrical tunable optical signal is sometimes problematic in many situations due to its shifting in peak position which is not suitable for many applications like DWDM where the number of signals travels together and those are densely spaced near to each other in a spectrum. For this reason, we have investigated electrical tunable optical characteristics with applied bias at two isolated p-n junctions simultaneously. In this approach of optical modulation, a shift in the peak position with an applied bias to one set of gratings is compensated by applying reverse polarity to another junction. As shown in Fig. 7.6 (c), different bias voltages at both the set of gratings are applied such that the peak of the resonance is fixed at λ = 1559.16 nm. Here it should be noted that not only the peak intensity is changing but also the FWHM of the resonance varies. With the applied set of voltages, a heavy reduction in the transmission peak intensity of 79% is observed. Further tuning of the optical signal is not preferable as it will cause a reduction of resonance intensity below than sidelobe which is not desirable. The proposed device can be programmed in such a way that it can compensate any shift in peak position either with applied bias or due to any thermal variation. We also predict that the use of less corrugated asymmetrical gratings one can achieve the narrower transmission peak but at the cost of limited FSR. In such a narrow transmission spectrum, low swing voltage can bring a larger modulation depth. To achieve a very high extinction ratio, MZI configuration can also be used as reported by Zhang et. al. [18]. However, it will require a much larger footprint area due to long arm length (typically in mm) required to obtain the π-phase shift. This approach of optical tuning offers direct modulation of the resonance peak position at a fixed wavelength. Zero drift attributes of the peak position at the output are much desirable in the DWDM technique along with optical modulation that can incorporate more and more signals in a given bandwidth, thus the capacity of the network can be improved.

7.6 Summary

In summary, a compact tapered cavity coupled comb-shaped asymmetric grating structure is proposed for multi-functional applications. Deliberately designed multimode waveguide support two modes of propagation in the waveguiding region. Asymmetricity caused by placing of sidewalls in the grating section stimulates the non-zero coupling of these modes in the co-propagation and counter-propagation direction. A narrowband transmission peak of 1.2 nm FWHM with a high extinction ratio of 14 dB is demonstrated in a highly compact active area of 21 μm^2. We have investigated the electrical tunability of the optical signals using FDTD method when two isolated p-n junctions are formed in both the grating sections. The shift in the resonance peak with decaying intensity is obtained with an external bias applied to one junction of the device. For the first time, we reported direct optical modulation at a fixed wavelength by applying electrical biasing to two independent p-n junctions. Due to a highly compact footprint area and novel approach to achieve zero-drift optical tuning makes it a strong candidate for solving several issues present in the communication system. For example, the proposed device can be programmed to make the device characteristics thermally stable by applying the appropriate biasing.

Chapter 8 Conclusion and future scope

8.1 Conclusion

On-chip silicon photonics emerging as a promising technology for electronic photonic integrated circuits (EPICs) due to mass production, low cost, and large-scale integration capabilities enabled by matured CMOS compatible fabrication flow. This thesis investigated engineered structure design on high index contrast silicon waveguide for on-chip optical guidance and modulation. The major contribution of the work included in the thesis are as follows:

Chapter 1: In this chapter evolution of silicon photonics to overcome the fundamental limitations of the electronic integrated circuit are discussed. This chapter includes some fundamental optical structures like ridge, rib, slot, photonic crystal, and grating-based structure along with its guiding mechanism and potential applications. A brief description of various photonic components used in optical interconnects is also included in this chapter.

Chapter 2: In this chapter, we have discussed various physical effects that have been extensively used for manipulation of the light signal with applying the electrical field. A detailed literature review of silicon-based optical modulators is also discussed in this chapter.

Chapter 3: This chapter consist of two different grating-based structures to guide and control the path of the optical signal. The first device included in the chapter is an off-chip grating coupler which couples the light from off chip fiber to silicon waveguide. The measured optical characteristics of the fabricated coupler shows broadband coupling efficiency for different cladded materials. In another device structure, Si-air High Contrast Grating (HCG) is designed and fabricated which act as a mirror for a broad range of wavelength and offers flexibility to shine the light from wide shallow angles.

Chapter 4: In this chapter, horizontally aligned p-n junction embedded in the slotted rib structure is proposed for high-speed optical modulation using the traveling-wave electrode. A low value of group index obtained in a proposed slotted-rib modulator offers a strong coupling of RF and optical mode at higher microwave frequencies. With the help of excellent index matching, high electrical bandwidth of 22.4 GHz is calculated for the proposed device at V_R = -6 V. Depletion of the free charge carriers at the junction with applied reverse bias offers modulation efficiency of 2.1 V.cm, with high data-rate capability up to 70 Gbit/s with an extinction ratio of 4.9 dB.

Chapter 5: In this chapter, two electrically isolated vertical p-n junction is designed at each side of the cladding region situated in slot structure. The various performance parameters like modulation efficiency, bandwidth, modulation speed and insertion loss are calculated using FDTD method. With the help of an optical slot structure, a high intrinsic bandwidth of 56 GHz is reported. Electrically isolated p-n junctions allow tuning of optical mode present in the slot region by maintaining the high modulation efficiency of 0.74 V-cm along with a high data rate up to 100 Gbit/s.

Chapter 6: In this chapter, a comb-like grating structure is designed, fabricated, and measured. The device consists of the π-phase shift cavity section coupled in between two sets of gratings. The gratings are deeply etched in the lateral direction to ensure the nonzero coupling of various optical modes present in the waveguide. In contrast to conventional Bragg grating where stopband lies in the transmission spectrum, we have demonstrated a single narrow passband transmission peak with a high extinction ratio of 20 dB. The large Free Spectral Range (FSR) attributed is achieved with the help of engineered photonic bandgap of two modes present in the waveguide region. The device is deliberately designed such that a slightly wide resonance peak is obtained that makes device operation thermally stable for a large temperature variation of ±15 K.

Chapter 7: In this chapter, a compact tapered cavity coupled asymmetric grating structure is designed, fabricated and measured. The fabricated structure exhibits a single transmission peak with a high extinction ratio of 14 dB and large FSR attributes which makes it suitable for the verity of on-chip applications including optical filter, modulator, etc. The theoretical analysis is performed to achieve efficient optical modulation of the signal at a fixed operating wavelength. For this reason, both the set of gratings are doped with p-n junctions such that the cavity act as an insulator between them. The shift in the peak position due to applied bias at one junction is compensated by applying a reverse electric field at another junction. The resonance peak is electrically tuned at $\lambda = 1559.16$ nm such that the transmission intensity reduced by 79% at the output of the device.

8.2 Future Scope

Although we have demonstrated single narrowband optical transmission characteristics in the comb-like asymmetrical grating structures, it remains with several future possibilities to further extend the objective of the thesis. Following are the future work for the thesis:

1. The proposed device demonstrates a relatively wide resonance peak (>1 nm) that can be narrower with further optimization process. For example, the corrugation width can be reduced to increase the quality factor of the device.
2. Theoretically investigated electro-optic tuning requires experimental verification with doped junctions.
3. The optical modulation can also be achieved when device is used with some electro-optic polymers, transparent conducting oxide materials and nano-composite materials as cladding of the device.
4. Multi cavity sections can be introduced in the device to achieve a slow light effect. However, this will increase the required length of the device.
5. The proposed multi-bias approach to obtain optical modulation is not analyzed for varying electric field (dynamic characteristics) for the device and needs to be explore.

References

1. GlobalFoundries to Deliver Industry's Leading-Performance Offering of 7nm FinFET Technology | GLOBALFOUNDRIES. https://www.globalfoundries.com/news-events/press-releases/globalfoundries-deliver-industrys-leading-performance-offering-7nm-finfet.

2. 7nm Technology - Taiwan Semiconductor Manufacturing Company Limited. https://www.tsmc.com/english/dedicatedFoundry/technology/7nm.htm.

3. TSMC and OIP Ecosystem Partners Deliver Industry's First Complete Design Infrastructure for 5nm Process Technology. https://www.tsmc.com/tsmcdotcom/PRListingNewsAction.do?action=detail&language=E&newsid=THPGWQTHTH.

4. Samsung Completes Development of 5nm EUV Process Technology. https://www.anandtech.com/show/14231/samsung-completes-development-of-5-nm-euv-process-technology.

5. Bikki, P. & Karuppanan, P. SRAM Cell Leakage Control Techniques for Ultra Low Power Application: A Survey. *Circuits and Systems* **8**, 23-52 (2017).

6. Bogaerts, W., Fiers, M. & Dumon, P. Design challenges in silicon photonics. *IEEE Journal of Selected Topics in Quantum Electronics* **20**, 1–8 (2014).

7. Kobrinsky, M. J. *et al.* On-Chip Optical Interconnects. *Intel Technology Journal* **8**, (2004).

8. Tong, L. *et al.* Subwavelength-diameter silica wires for low-loss optical wave guiding. *Nature* **426**, 816 (2003).

9. Miya, T., Terunuma, Y., Hosaka, T. & Miyashita, T. Ultimate low-loss single-mode fibre at 1.55 μm. *Electronics Letters* **15**, 106–108 (1979).

10. Hui, R. *Introduction to Fiber-Optic Communications*, Academic Press (2019).

11. Asghari, M. & Krishnamoorthy, A. v. Silicon photonics: Energy-efficient communication. *Nature photonics* **5**, 268 (2011).

12. Ma, Y. *et al.* Ultralow loss single layer submicron silicon waveguide crossing for SOI optical interconnect. *Optics express* **21**, 29374–29382 (2013).

13. Assefa, S. *et al.* A 90nm CMOS integrated nano-photonics technology for 25 Gbps WDM optical communications applications. in *Electron Devices Meeting (IEDM), 2012 IEEE International* 33–38 (2012).

14. Sun, C. *et al.* A monolithically integrated chip-to-chip optical link in bulk CMOS. *IEEE Journal of Solid-State Circuits* **50**, 828–844 (2015).

15. Juodawlkis, P. W. *et al.* Optically sampled analog-to-digital converters. *IEEE Transactions on Microwave Theory and Techniques* **49**, 1840–1853 (2001).

16. Kim, T. K., Song, Y., Jung, K., Kim, C., Kim, H., Nam, C. H., & Kim, J., Sub-100-as timing jitter optical pulse trains from mode-locked Er-fiber lasers. Optics letters, **36**, 4443-4445, (2011).

17. Jalali, B., & Fathpour, S. Silicon photonics. *Journal of lightwave technology*, **24**, 4600-4615 (2006).

18. Zhang, W. & Yao, J. A fully reconfigurable waveguide Bragg grating for programmable photonic signal processing. *Nature communications* **9**, 1396 (2018).

19. Soref, R., Mid-infrared photonics in silicon and germanium. Nature photonics, **4**, 495-497 (2010).

20. Preble, S. F. *et al*. On-Chip Quantum Interference from a Single Silicon Ring-Resonator Source. *APS* **4**, (2015).

21. Leuthold, J., Freude, W., Brosi, J. M., Baets, R., Dumon, P., Biaggio, I., & Koos, C. Silicon organic hybrid technology—A platform for practical nonlinear optics. Proceedings of the IEEE, **97**, 1304-1316, (2009).

22. Fan, L. *et al.* An all-silicon passive optical diode. *Science* **335**, 447–450 (2012).

23. Liu, M., Yin, X., Ulin-Avila, E., Geng, B., Zentgraf, T., Ju, L., & Zhang, X. A graphene-based broadband optical modulator. *Nature*, ***474***, 64-67, (2011).

24. Dalir, H., Xia, Y., Wang, Y. & Zhang, X. Athermal broadband graphene optical modulator with 35 GHz speed. *Acs Photonics* **3**, 1564–1568 (2016).

25. Gabrielli, L. H., Liu, D., Johnson, S. G., & Lipson, M. On-chip transformation optics for multimode waveguide bends. *Nature communications*, ***3***, 1-6, (2012).

26. Sun, J., Timurdogan, E., Yaacobi, A., Hosseini, E. S., & Watts, M. R. Large-scale nanophotonic phased array. *Nature*, ***493***, 195-199, (2013).

27. Crespi, A., Ramponi, R., Osellame, R., Sansoni, L., Bongioanni, I., Sciarrino, F., & Mataloni, P. Integrated photonic quantum gates for polarization qubits. *Nature communications*, ***2***, 1-6, (2011).

28. Silverstone, J. W. *et al.* On-chip quantum interference between silicon photon-pair sources. *Nature Photonics* **8**, 104–108 (2014).

29. Jia, H., Yang, S., Zhou, T., Shao, S., Fu, X., Zhang, L., & Yang, L. WDM-compatible multimode optical switching system-on-chip. *Nanophotonics*, ***8***, 889-898, 2019.

30. Säynätjoki, A., Karvonen, L., Alasaarela, T., Tu, X., Liow, T. Y., Hiltunen, M., & Honkanen, S. Low-loss silicon slot waveguides and couplers fabricated with optical lithography and atomic layer deposition. *Optics express*, ***19***, 26275-26282, (2011).

31. Xu, Q., Almeida, V. R., Panepucci, R. R., & Lipson, M. Experimental demonstration of guiding and confining light in nanometer-size low-refractive-index material. *Optics letters*, ***29***, 1626-1628, (2004).

32. Wang, Z., Zhu, N., Tang, Y., Wosinski, L., Dai, D., & He, S. Ultracompact low-loss coupler between strip and slot waveguides. *Optics letters*, ***34***, 1498-1500, (2009).

33. Passaro, V. M. N. & Notte, M. la. Optimizing SOI Slot Waveguide Fabrication Tolerances and Strip-Slot Coupling for Very Efficient Optical Sensing. *Sensors* **12**, 2436–2455 (2012).

34. Jain, S., Rajput, S., Kaushik, V., Sulabh & Kumar, M. Efficient Optical Modulation with High Data-Rate in Silicon Based Laterally Split Vertical p-n Junction. *IEEE Journal of Quantum Electronics* **56**, (2020).

35. Jain, S., Rajput, S., Kaushik, V. & Kumar, M. High speed optical modulator based on silicon slotted-rib waveguide. *Optics Communications* **434**, 49–53 (2019).

36. Alloatti, L. *et al.* 100 GHz silicon--organic hybrid modulator. *Light: Science & Applications* **3**, e173 (2014).

37. Kumar, M. *et al.* Low birefringence and 2-D optical confinement of hollow waveguide with distributed Bragg reflector and high-index-contrast grating. *IEEE Photonics Journal* **1**, 135–143 (2009).

38. Kumar, M., Sakaguchi, T. & Koyama, F. Wide tunability and ultralarge birefringence with 3D hollow waveguide Bragg reflector. *Optics letters* **34**, 1252–1254 (2009).

39. Kumar, M. Narrow bandwidth and polarization independent design of hollow waveguide in-plane mirror with ultrawide tuning-range. *Applied optics* **52**, 1847–1851 (2013).

40. Rajput, S., Kaushik, V., Jain, S. & Kumar, M. Slow Light Enhanced Phase-shifter Based on Low-loss Silicon-ITO Hollow Waveguide. *IEEE Photonics Journal* (2019).

41. Kumar, M., Sakagichi, T. & Koyama, F. Giant birefringence and tunable differential group delay in Bragg reflector based on tapered three-dimensional hollow waveguide. *Applied Physics Letters* **94**, 61112 (2009).

42. Paniccia, M., Krutul, V., Jones, R., Cohen, O., Bowers, J., Fang, A., & Park, H. A Hybrid Silicon Laser: Silicon photonics technology for future tera-scale computing. *White Paper, (2006)*.

43. Boyd, R. *Nonlinear optics*, Academic Press (2019).

44. Chuang, S. L. Physics of Optoelectronic Devices John Wiley & Sons. *New York*, (1995).

45. Soref, R. A. Silicon-Based Optoelectronics. *Proceedings of the IEEE* **81**, 1687–1706 (1993).

46. Solutions, F. Lumerical Solutions. *Inc.*, http://www.lumerical.Com, (2003).

47. Sze, S. M., & Ng, K. K., *Physics of semiconductor devices*. John wiley & sons, (2006)

48. Li, Z., Lv, Y., Ren, L., Li, J., Kong, L., Zeng, Y., & Wang, D. Efficient strain modulation of 2D materials via polymer encapsulation. *Nature communications*, ***11***, 1-8, (2020).

49. Abel, S., Eltes, F., Ortmann, J. E., Messner, A., Castera, P., Wagner, T., & Ma, P. Large Pockels effect in micro-and nanostructured barium titanate integrated on silicon. *Nature materials*, ***18***, 42-47, (2019).

50. Jacobsen, R. S., Andersen, K. N., Borel, P. I., Fage-Pedersen, J., Frandsen, L. H., Hansen, O., & Peucheret, C. Strained silicon as a new electro-optic material. *Nature*, ***441***, 199-202, (2006).

51. Soref, R. & Bennett, B. Electrooptical effects in silicon. *IEEE journal of quantum electronics* **23**, 123–129 (1987).

52. Miller, D. A. B. *et al.* Band-edge electroabsorption in quantum well structures: The quantum-confined stark effect. *Physical Review Letters* **53**, 2173–2176 (1984).

53. Kuo, Y. H., Lee, Y. K., Ge, Y., Ren, S., Roth, J. E., Kamins, T. I., & Harris, J. S. Strong quantum-confined Stark effect in germanium quantum-well structures on silicon. *Nature*, ***437***, 1334-1336, (2005).

54. Dumas, D. C. S. *et al.* Ge/SiGe quantum confined Stark effect electro-absorption modulation with low voltage swing at λ = 1550 nm. *Optics Express* **22**, 19284 (2014).

55. Gan, F. & Tong, S. J. *High-Speed Silicon Electro-Optic Modulator for Electronic Photonic Integrated Circuits*. https://dspace.mit.edu/handle/1721.1/40498 (2000).

56. Schroder, D. K. *Semiconductor material and device characterization*. John Wiley & Sons, (2015).

57. Komma, J., Schwarz, C., Hofmann, G., Heinert, D. & Nawrodt, R. Thermo-optic coefficient of silicon at 1550 nm and cryogenic temperatures. *Applied Physics Letters* **101**, (2012).

58. Gan, S. *et al.* A highly efficient thermo-optic microring modulator assisted by graphene. *Nanoscale* **7**, 20249–20255 (2015).

59. Grinenko, A. *et al.* Tunable beam shaping with a phased array acousto-optic modulator. *Optics Express* **23**, 26 (2015).

60. Kim, S., Barbastathis, G. & Tuller, H. L. MEMS for optical functionality. *Journal of Electroceramics* vol. **12** 133–144 (2004).

61. Wang, J. *CMOS-Compatible Key Engineering Devices for High-Speed Silicon-Based Optical Interconnections*. Springer, (2018).

62. Liu, A., Jones, R., Liao, L., Samara-Rubio, D., Rubin, D., Cohen, O., & Paniccia, M. A high-speed silicon optical modulator based on a metal–oxide–semiconductor capacitor. *Nature*, ***427***, 615-618, (2004).

63. He, M., Xu, M., Ren, Y., Jian, J., Ruan, Z., Xu, Y., & Liu, L. High-performance hybrid silicon and lithium niobate Mach–Zehnder modulators for 100 Gbit s− 1 and beyond. *Nature Photonics*, ***13,*** 359-364, (2019).

64. DeRose, C. T. *et al.* Ultra compact 45 GHz CMOS compatible Germanium waveguide photodiode with low dark current. *Optics Express* **19**, 24897 (2011).

65. Huang, Z. *et al.* A 25Gbps low-voltage waveguide Si-Ge avalanche photodiode. in *2016 Conference on Lasers and Electro-Optics, CLEO 2016* vol. 3 793–798 (Institute of Electrical and Electronics Engineers Inc., 2016).

66. Reed, G. T., Mashanovich, G., Gardes, F. Y., & Thomson, D. J. Silicon optical modulators. *Nature photonics*, ***4,*** 518-526, (2010).

67. Soref, R. & Bennett, B. Electrooptical effects in silicon. *IEEE journal of quantum electronics* **23**, 123–129 (1987).

68. Reed, G. T., Mashanovich, G., Gardes, F. Y., & Thomson, D. J. Silicon optical modulators. *Nature photonics*, ***4,*** 518-526, (2010).

69. Xu, Q., Manipatruni, S., Schmidt, B., Shakya, J. & Lipson, M. 12.5 Gbit/s carrier-injection-based silicon micro-ring silicon modulators. *Optics express* **15**, 430–436 (2007).

70. Manipatruni, S., Xu, Q., Schmidt, B., Shakya, J. & Lipson, M. High speed carrier injection 18 Gb/s silicon micro-ring electro-optic modulator. in *Lasers and Electro-Optics Society, 2007. LEOS 2007. The 20th Annual Meeting of the IEEE* 537–538 (2007).

71. Manipatruni, S., Xu, Q., Schmidt, B., Shakya, J., & Lipson, M. High speed carrier injection 18 Gb/s silicon micro-ring electro-optic modulator. In *LEOS 2007-IEEE Lasers and Electro-Optics Society Annual Meeting Conference Proceedings* (pp. 537-538), (2007)

72. Liu, A. *et al.* A high-speed silicon optical modulator based on a metal-oxide-semiconductor capacitor. *Nature* **427**, 615–618 (2004).

73. Gardes, F. Y., Reed, G. T., Emerson, N. G. & Png, C. E. A sub-micron depletion-type photonic modulator in Silicon On Insulator. *Optics Express* **13**, 8845 (2005).

74. Liu, A. *et al.* High-speed optical modulation based on carrier depletion in a silicon waveguide. *Optics Express* **15**, 660 (2007).

75. Xiao, X. *et al.* 44-Gb/s silicon microring modulators based on zigzag PN junctions. *IEEE Photonics Technology Letters* **24**, 1712–1714 (2012).

76. Gardes, F. Y. *et al.* High-speed modulation of a compact silicon ring resonator based on a reverse-biased pn diode. *Optics Express* **17**, 21986 (2009).

77. Vlasov, Y. A., O'boyle, M., Hamann, H. F. & McNab, S. J. Active control of slow light on a chip with photonic crystal waveguides. *Nature* **438**, 65 (2005).

78. Baba, T. *et al.* Slow-light Mach--Zehnder modulators based on Si photonic crystals. *Science and technology of advanced materials* **15**, 24602 (2014).

79. Gardes, F. Y. *et al.* High-speed modulation of a compact silicon ring resonator based on a reverse-biased pn diode. *Optics Express* **17**, 21986 (2009).

80. Rasigade, G., Marris-Morini, D., Vivien, L. & Cassan, E. Performance evolutions of carrier depletion silicon optical modulators: From p-n to p-i-p-i-n diodes. *IEEE Journal on Selected Topics in Quantum Electronics* **16**, 179–184 (2010).

81. Rasigade, G. *et al.* High extinction ratio 10 Gbit/s silicon optical modulator. *Optics Express* **19**, 5827 (2011).

82. Thomson, D. J. *et al.* High contrast 40Gbit/s optical modulation in silicon. *Optics Express* **19**, 11507 (2011).

83. Xu, H. *et al.* High speed silicon Mach-Zehnder modulator based on interleaved PN junctions. *Optics Express* **20**, 15093 (2012).

84. Baehr-Jones, T. *et al.* Ultralow drive voltage silicon traveling-wave modulator. *Optics express* **20**, 12014–12020 (2012).

85. Tu, X. *et al.* 50-Gb/s silicon optical modulator with traveling-wave electrodes. *Optics Express* **21**, 12776 (2013).

86. Timurdogan, E. *et al.* An ultralow power athermal silicon modulator. *Nature Communications* **5**, 1–11 (2014).

87. Zhang, W., Ehteshami, N., Liu, W. & Yao, J. Silicon-based on-chip electrically tunable sidewall Bragg grating Fabry–Perot filter. *Optics Letters* **40**, 3153 (2015).

88. Ding, J., Shao, S., Zhang, L., Fu, X. & Yang, L. Method to improve the linearity of the silicon Mach-Zehnder optical modulator by doping control. *Optics Express* **24**, 24641 (2016).

89. Maegami, Y. *et al.* High-efficiency strip-loaded waveguide based silicon Mach-Zehnder modulator with vertical pn junction phase shifter. *Optics express* **25**, 31407–31416 (2017).

90. Yong, Z. *et al.* U-shaped PN junctions for efficient silicon Mach-Zehnder and microring modulators in the O-band: erratum. *Optics express* **26**, 32757 (2018).

91. Deng, H. & Bogaerts, W. Pure phase modulation based on a silicon plasma dispersion modulator. *Optics Express* **27**, 27191 (2019).

92. Cui, Y., Liu, K., MacFarlane, D. L. & Lee, J.-B. Thermo-optically tunable silicon photonic crystal light modulator. *Optics Letters* **35**, 3613 (2010).

93. Li, Y., Yu, J., Chen, S., Li, Y. & Chen, Y. Submicrosecond rearrangeable nonblocking silicon-on-insulator thermo-optic 4×4 switch matrix. *Optics Letters* **32**, 603 (2007).

94. Chaisakul, P., Marris-Morini, D., Rouifed, M. S., Isella, G., Chrastina, D., Frigerio, J., & Vivien, L., 23 GHz Ge/SiGe multiple quantum well electro-absorption modulator. *Optics Express*, ***20***, 3219-3224, (2012).

95. Zhang, L., Sinsky, J., Van Thourhout, D., Sauer, N., Stulz, L., Adamiecki, A., & Chandrasekhar, S., Low-voltage high-speed travelling wave InGaAsP-InP phase modulator. *IEEE Photonics Technology Letters*, ***16***, 1831-1833, (2004).

96. Rong, Y., Ge, Y., Huo, Y., Fiorentino, M., Tan, M. R., Kamins, T. I., & Harris Jr, J. S. Quantum-confined Stark effect in Ge/SiGe quantum wells on Si. *IEEE Journal of selected topics in quantum electronics*, ***16***, 85-92, (2009).

97. Liu, J., Pan, D., Jongthammanurak, S., Wada, K., Kimerling, L. C., & Michel, J., Design of monolithically integrated GeSi electro-absorption modulators and photodetectors on an SOI platform. *Optics Express*, ***15***, 623-628, (2007).

98. Feng, D. *et al.* High speed GeSi electro-absorption modulator at 1550 nm wavelength on SOI waveguide. *Optics Express* **20**, 22224 (2012).

99. Feng, N.-N. *et al.* 30GHz Ge electro-absorption modulator integrated with 3$µ$m silicon-on-insulator waveguide. *Optics express* **19**, 7062–7067 (2011).

100. Lim, A. E.-J. *et al.* Novel evanescent-coupled germanium electro-absorption modulator featuring monolithic integration with germanium pin photodetector. *Optics express* **19**, 5040–5046 (2011).

101. Schmid, M. *et al.* Franz--Keldysh effect of germanium-on-silicon p--i--n diodes within a wide temperature range. *Thin Solid Films* **525**, 110–114 (2012).

102. Reed, G. T. & Knights, A. P. *Silicon photonics: an introduction*. (John Wiley & Sons, 2004).

103. Liu, J. *et al.* Waveguide-integrated, ultralow-energy GeSi electro-absorption modulators. *Nature Photonics* **2**, 433 (2008).

104. Mastronardi, L. *et al.* High-speed Si/GeSi hetero-structure electro absorption modulator. *Optics express* **26**, 6663–6673 (2018).

105. Bolotin, K. I. *et al.* Ultrahigh electron mobility in suspended graphene. *Solid State Communications* **146**, 351–355 (2008).

106. Mak, K. F. *et al.* Measurement of the optical conductivity of graphene. *Physical review letters* **101**, 196405 (2008).

107. Bao, Q. & Loh, K. P. Graphene photonics, plasmonics, and broadband optoelectronic devices. *ACS nano* **6**, 3677–3694 (2012).

108. Xu, Y. *et al.* Hybrid Graphene-Silicon Based Polarization-Insensitive Electro-Absorption Modulator with High-Modulation Efficiency and Ultra-Broad Bandwidth. *Nanomaterials* **9**, 157 (2019).

109. Dalir, H., Xia, Y., Wang, Y. & Zhang, X. Athermal broadband graphene optical modulator with 35 GHz speed. *Acs Photonics* **3**, 1564–1568 (2016).

110. Wang, B. *et al.* Plasmonic-based subwavelength graphene-on-hBN modulator on silicon photonics. *IEEE Journal of Selected Topics in Quantum Electronics* (2019).

111. Liu, J. *et al.* Recent advances in polymer electro-optic modulators. *Rsc Advances* **5**, 15784–15794 (2015).

112. Binh, L. N. Optical multi-bound solitons. *LN Binh--CRC Press.--2015.--567 p* (2015).

113. Kieninger, C. *et al.* Ultra-high electro-optic activity demonstrated in a silicon-organic hybrid modulator. *Optica* **5**, 739–748 (2018).

114. Norwood, R. A., Kuzyk, M. G. & Keosian, R. A. Electro-optic tensor ratio determination of side-chain copolymers with electro-optic interferometry. *Journal of applied physics* **75**, 1869–1874 (1994).

115. Shi, S. & Prather, D. W. Dual RF-optical slot waveguide for ultrabroadband modulation with a sub-volt Vπ. *Applied Physics Letters* **96**, 201107 (2010).

116. Chang-Hasnain, C. J., & Yang, W. High-contrast gratings for integrated optoelectronics. *Advances in Optics and Photonics*, ***4***, 379-440, (2012).

117. Loewen, E. & Popov, E. *Diffraction gratings and applications*. (2018).

118. Nambiar, S., Ranganath, P., Kallega, R. & Selvaraja, S. K. High efficiency DBR assisted grating chirp generators for silicon nitride fiber-chip coupling. *Scientific Reports* **9**, 1–9 (2019).

119. Goeman, S., Boons, S., Dhoedt, B., Vandeputte, K., Caekebeke, K., Van Daele, P., & Baets, R. First demonstration of highly reflective and highly polarization selective diffraction gratings (GIRO-gratings) for long-wavelength VCSELs. *IEEE Photonics Technology Letters*, ***10***, 1205-1207, (1998).

120. Astilean, S., Lalanne, P., Chavel, P., Cambril, E., & Launois, H., High-efficiency subwavelength diffractive element patterned in a high-refractive-index material for 633?? nm. *Optics letters*, ***23***, 552-554, (1998).

121. Dewanjee, A., Caspers, J. N., Aitchison, J. S., & Mojahedi, M. Demonstration of a compact bilayer inverse taper coupler for Si-photonics with enhanced polarization insensitivity. *Optics Express*, ***24***, 28194-28203, (2016).

122. Ren, G., Chen, S., Cheng, Y., & Zhai, Y., Study on inverse taper based mode transformer for low loss coupling between silicon wire waveguide and lensed fiber. *Optics Communications*, ***284***, 4782-4788, (2011)

123. Taillaert, D., Bogaerts, W., Bienstman, P., Krauss, T. F., Van Daele, P., Moerman, I., & Baets, R. An out-of-plane grating coupler for efficient butt-coupling between compact planar waveguides and single-mode fibers. *IEEE Journal of Quantum Electronics*, ***38***, 949-955, (2002).

124. Chen, X., Li, C., & Tsang, H. K. Fabrication-tolerant waveguide chirped grating coupler for coupling to a perfectly vertical optical fiber. *IEEE Photonics Technology Letters*, ***20***, 1914-1916, (2008).

125. Antelius, M., Gylfason, K. B., & Sohlström, H. An apodized SOI waveguide-to-fiber surface grating coupler for single lithography silicon photonics. *Optics express*, ***19***, 3592-3598, (2011).

126. Li, C., Zhang, H., Yu, M. & Lo, G. Q. CMOS-compatible high efficiency double-etched apodized waveguide grating coupler. *Optics Express* **21**, 7868 (2013).

127. Vermeulen, D. *et al.* High-efficiency fiber-to-chip grating couplers realized using an advanced CMOS-compatible Silicon-On-Insulator platform. *Optics Express* **18**, 18278 (2010).

128. Moharam, M. G., & Gaylord, T. K. Rigorous coupled-wave analysis of planar-grating diffraction. *JOSA*, ***71***, 811-818, (1981).

129. Zhou, Y., Karagodsky, V., Pesala, B., Sedgwick, F. G. & Chang-Hasnain, C. J. A novel ultra-low loss hollow-core waveguide using subwavelength high-contrast gratings. *Optics Express* **17**, 1508 (2009).

130. Senior, J. & Jamro, M. Optical fiber communications: principles and practice. (2009).

131. Wang, X. & Liu, J. Emerging technologies in Si active photonics. *Journal of Semiconductors* **39**, 1–29 (2018).

132. Thomson, D. *et al.* Roadmap on silicon photonics. *Journal of Optics* **18**, 73003 (2016).

133. Lim, A. E.-J. *et al.* Review of silicon photonics foundry efforts. *IEEE Journal of Selected Topics in Quantum Electronics* **20**, 405–416 (2014).

134. Won, R. & Paniccia, M. Integrating silicon photonics. *Nature Photonics* **4**, (2010).

135. Subbaraman, H. *et al.* Recent advances in silicon-based passive and active optical interconnects. *Optics express* **23**, 2487–2511 (2015).

136. Chen, L., Preston, K., Manipatruni, S. & Lipson, M. Integrated GHz silicon photonic interconnect with micrometer-scale modulators and detectors. *Optics express* **17**, 15248–15256 (2009).

137. Gunn, C. CMOS photonics for high-speed interconnects. *IEEE micro* **26**, 58–66 (2006).

138. Thomson, D. J. *et al.* 50-Gb/s Silicon Optical Modulator. *IEEE PHOTONICS TECHNOLOGY LETTERS* **24**, (2012).

139. Xu, H. *et al.* Demonstration and characterization of high-speed silicon depletion-mode Mach--Zehnder modulators. *IEEE Journal of Selected Topics in Quantum Electronics* **20**, 23–32 (2014).

140. Xu, Q., Schmidt, B., Pradhan, S. & Lipson, M. Micrometre-scale silicon electro-optic modulator. *nature* **435**, 325 (2005).

141. Zhu, S., Lo, G. Q. & Kwong, D. L. Electro-absorption modulation in horizontal metal-insulator-silicon-insulator-metal nanoplasmonic slot waveguides. *Applied Physics Letters* **99**, 151114 (2011).

142. Green, W. M. J., Rooks, M. J., Sekaric, L. & Vlasov, Y. A. Ultra-compact, low RF power, 10 Gb/s silicon Mach-Zehnder modulator. *Optics express* **15**, 17106–17113 (2007).

143. Geng, M. *et al.* Four-channel reconfigurable optical add-drop multiplexer based on photonic wire waveguide. *Optics express* **17**, 5502–5516 (2009).

144. Dragone, C., *U.S. Patent No. 5,002,350*. Washington, DC: U.S. Patent and Trademark Office, (1991)

145. Ziebell, M. *et al.* 40 Gbit/s low-loss silicon optical modulator based on a pipin diode. *Optics express* **20**, 10591–10596 (2012).

146. Dakin, J. P. & Brown, R. G. W. *Handbook of Optoelectronics (two-volume set)*. (CRC Press, 2006).

147. Singh, L., Sharma, T. & Kumar, M. Controlled Hybridization of Plasmonic and Optical Modes for Low-Loss Nano-Scale Optical Confinement With Ultralow Dispersion. *IEEE Journal of Quantum Electronics* **54**, 1–5 (2018).

148. Bonaccorso, F., Sun, Z., Hasan, T. & Ferrari, A. C. Graphene photonics and optoelectronics. *Nature photonics* **4**, 611 (2010).

149. Jindal, S., Sobti, S., Kumar, M., Sharma, S. & Pal, M. K. Nanocavity-coupled photonic crystal waveguide as highly sensitive platform for cancer detection. *IEEE Sensors Journal* **16**, 3705–3710 (2016).

150. Ding, J. *et al.* Low-voltage, high-extinction-ratio, Mach-Zehnder silicon optical modulator for CMOS-compatible integration. *Optics express* **20**, 3209–3218 (2012).

151. Burla, M., Wang, X., Li, M., Chrostowski, L. & Azaña, J. Wideband dynamic microwave frequency identification system using a low-power ultracompact silicon photonic chip. *Nature communications* **7**, 13004 (2016).

152. Roelkens, G. *et al.* Silicon-based photonic integration beyond the telecommunication wavelength range. *IEEE Journal of Selected Topics in Quantum Electronics* **20**, 394–404 (2014).

153. Kaminow, I. P. Optical integrated circuits: a personal perspective. *Journal of Lightwave Technology* **26**, 994–1004 (2008).

154. Beausoleil, R. G. *et al.* Photonic interconnect system. (2008).

155. Singh, L., Jain, S. & Kumar, M. Electrically writable silicon nanophotonic resistive memory with inherent stochasticity. *Optics letters* **44**, 4020–4023 (2019).

156. Zhang, X. *et al.* High performance optical modulator based on electro-optic polymer filled silicon slot photonic crystal waveguide. *Journal of Lightwave Technology* **34**, 2941–2951 (2015).

157. Baek, J., You, J.-B. & Yu, K. Free-carrier electro-refraction modulation based on a silicon slot waveguide with ITO. *Optics express* **23**, 15863–15876 (2015).

158. Youngblood, N., Anugrah, Y., Ma, R., Koester, S. J. & Li, M. Multifunctional graphene optical modulator and photodetector integrated on silicon waveguides. *Nano letters* **14**, 2741–2746 (2014).

159. Rajput, S., Kaushik, V., Jain, S., Tiwari, P., Srivastava, A. K., & Kumar, M., Optical modulation in hybrid waveguide based on Si-ITO heterojunction. *Journal of Lightwave Technology*, ***38***, 1365-1371, (2019).

160. Baba, T. Slow light in photonic crystals. *Nature photonics* **2**, 465 (2008).

161. Gardes, F. Y. *et al.* High-speed modulation of a compact silicon ring resonator based on a reverse-biased pn diode. *Optics express* **17**, 21986–21991 (2009).

162. Jain, S., Srivastava, S., Rajput, S., Singh, L., Tiwari, P., Srivastava, A. K., & Kumar, M., Thermally stable optical filtering using silicon-based comb-like asymmetric grating for sensing applications. *IEEE Sensors Journal*, ***20***, 3529-3535, (2019)

163. Sulabh, Singh, L., Jain, S., & Kumar, M., Optical slot waveguide with grating-loaded cladding of silicon and titanium dioxide for label-free bio-sensing. *IEEE Sensors Journal*, ***19***, 6126-6133, (2019).

164. Zhang, X. *et al.* Integrated photonic electromagnetic field sensor based on broadband bowtie antenna coupled silicon organic hybrid modulator. *Journal of Lightwave Technology* **32**, 3774–3784 (2014).

165. Emboras, A. *et al.* Nanoscale plasmonic memristor with optical readout functionality. *Nano letters* **13**, 6151–6155 (2013).

166. Shi, J. *et al.* MoOx modified ITO/a-Si: H (p) contact for silicon heterojunction solar cell application. *Materials Research Bulletin* **97**, 176–181 (2018).

167. Flueckiger, J. *et al.* Sub-wavelength grating for enhanced ring resonator biosensor. *Optics express* **24**, 15672–15686 (2016).

168. Kita, D. M., Michon, J., Johnson, S. G. & Hu, J. Are slot and sub-wavelength grating waveguides better than strip waveguides for sensing? *Optica* **5**, 1046–1054 (2018).

169. Cao, S. *et al.* Highly sensitive surface plasmon resonance biosensor based on a low-index polymer optical fiber. *Optics express* **26**, 3988–3994 (2018).

170. Dandapat, K., Tripathi, S. M., Chinifooroshan, Y., Bock, W. J. & Mikulic, P. Compact and cost-effective temperature-insensitive bio-sensor based on long-period fiber gratings for accurate detection of E. coli bacteria in water. *Optics letters* **41**, 4198–4201 (2016).

171. Fernández Gavela, A., Grajales Garcia, D., Ramirez, J. C. & Lechuga, L. M. Last advances in silicon-based optical biosensors. *sensors* **16**, 285 (2016).

172. Sana, A. K., Honzawa, K., Amemiya, Y. & Yokoyama, S. Silicon photonic crystal resonators for label free biosensor. *Japanese Journal of Applied Physics* **55**, 04EM11 (2016).

173. Campanella, C. E., Campanella, C. M., de Leonardis, F. & Passaro, V. M. N. A high efficiency label-free photonic biosensor based on vertically stacked ring resonators. *The European Physical Journal Special Topics* **223**, 2009–2021 (2014).

174. Huang, L. *et al.* Improving the detection limit for on-chip photonic sensors based on subwavelength grating racetrack resonators. *Optics express* **25**, 10527–10535 (2017).

175. Zhang, L. & Dai, D. Silicon Subwavelength-Grating Microdisks for Optical Sensing. *IEEE Photonics Technology Letters* **31**, 1209-1212 (2019).

176. Liu, S. *et al.* End-fire injection of light into high-Q silicon microdisks. *Optica* **5**, 612–616 (2018).

177. Tu, X. *et al.* Thermal independent silicon-nitride slot waveguide biosensor with high sensitivity. *Optics express* **20**, 2640–2648 (2012).

178. Sah, P. & Das, B. K. Integrated optical rectangular-edge filter devices in SOI. *Journal of Lightwave Technology* **35**, 128–135 (2016).

179. Lai, W.-C., Chakravarty, S., Zou, Y., Guo, Y. & Chen, R. T. Slow light enhanced sensitivity of resonance modes in photonic crystal biosensors. *Applied physics letters* **102**, 41111 (2013).

180. Tu, Z., Gao, D., Zhang, M. & Zhang, D. High-sensitivity complex refractive index sensing based on Fano resonance in the subwavelength grating waveguide micro-ring resonator. *Optics express* **25**, 20911–20922 (2017).

181. Wang, X. *et al.* Narrow-band transmission filter using phase-shifted Bragg gratings in SOI waveguide. in *IEEE Photonic Society 24th Annual Meeting* 869–870 (2011).

182. Zhu, J. *et al.* On-chip single nanoparticle detection and sizing by mode splitting in an ultrahigh-Q microresonator. *Nature photonics* **4**, 46 (2010).

183. Campanella, C. M., Dunai, M., Calabrese, L. & Campanella, C. E. Design guidelines for nanoparticle chemical sensors based on mode-splitting silicon-on-insulator planar microcavities. *JOSA B* **33**, 2383–2394 (2016).

184. Kang, Y., François, A., Riesen, N. & Monro, T. Mode-splitting for refractive index sensing in fluorescent whispering gallery mode microspheres with broken symmetry. *Sensors* **18**, 2987 (2018).

185. Li, J. *et al.* Coexistence of broad-bandwidth and strong microwave absorption in Co2+-Zr4+ co-doped barium ferrite ceramics. *Ceramics International* **44**, 6953–6958 (2018).

186. Li, Y. *et al.* Enhanced performance in Al-doped ZnO based transparent flexible transparent thin-film transistors due to oxygen vacancy in ZnO film with Zn--Al--O interfaces fabricated by atomic layer deposition. *ACS applied materials & interfaces* **9**, 11711–11720 (2017).

187. Wu, Y. *et al.* Origin of the dielectric abnormities and tunable dielectric properties in doped KTN single crystals. *Applied Physics Letters* **111**, 242902 (2017).

188. Caucheteur, C., Guo, T. & Albert, J. Polarization-assisted fiber Bragg grating sensors: Tutorial and review. *Journal of Lightwave Technology* **35**, 3311–3322 (2016).

189. Xu, L., Liu, N., Ge, J., Wang, X. & Fok, M. P. Stretchable fiber-Bragg-grating-based sensor. *Optics letters* **43**, 2503–2506 (2018).

190. Puckett, M. W., Vallini, F., Grieco, A. & Fainman, Y. Multichannel Bragg gratings in silicon waveguides with asymmetric sidewall modulation. *Optics letters* **40**, 379–382 (2015).

191. Qiu, H. *et al.* Silicon band-rejection and band-pass filter based on asymmetric Bragg sidewall gratings in a multimode waveguide. *Optics letters* **41**, 2450–2453 (2016).

192. Kang, Y. M., Arbabi, A. & Goddard, L. L. Engineering the spectral reflectance of microring resonators with integrated reflective elements. *Optics express* **18**, 16813–16825 (2010).

193. Jellison Jr, G. E. & Burke, H. H. The temperature dependence of the refractive index of silicon at elevated temperatures at several laser wavelengths. *Journal of applied physics* **60**, 841–843 (1986).

194. Steglich, P. *et al.* Hybrid-waveguide ring resonator for biochemical sensing. *IEEE Sensors Journal* **17**, 4781–4790 (2017).

195. Huang, L. *et al.* Improving the detection limit for on-chip photonic sensors based on subwavelength grating racetrack resonators. *Optics express* **25**, 10527–10535 (2017).

196. Nagatsuma, T., Ducournau, G. & Renaud, C. C. Advances in terahertz communications accelerated by photonics. *Nature Photonics* **10**, 371–379 (2016).

197. Nagarajan, R. *et al.* Silicon photonics-based 100 Gbit/s, PAM4, DWDM data center interconnects. *Journal of Optical Communications and Networking* **10**, B25–B36 (2018).

198. Cheng, Q., Bahadori, M., Glick, M., Rumley, S. & Bergman, K. Recent advances in optical technologies for data centers: a review. *Optica* **5**, 1354 (2018).

199. Subbaraman, H. *et al.* Recent advances in silicon-based passive and active optical interconnects. *Optics Express* **23**, 2487 (2015).

200. Radhakrishnan, R. *et al.* Silicon photonics-based 100 Gbit/s, PAM4, DWDM data center interconnects. *Journal of Optical Communications and Networking* **10**, B25–B36 (2018).

201. Chen, C.-H. *et al.* A comb laser-driven DWDM silicon photonic transmitter based on microring modulators. *Optics Express* **23**, 21541 (2015).

202. Seyedi, M. A., Chen, C.-H., Fiorentino, M. & Beausoleil, R. Error-free DWDM transmission and crosstalk analysis for a silicon photonics transmitter. *Optics Express* **23**, 32968 (2015).

203. London, Y. *et al.* Energy Efficiency Analysis of Comb Source Carrier-Injection Ring-Based Silicon Photonic Link. *IEEE Journal of Selected Topics in Quantum Electronics* **26**, (2019).

204. Kong, D., Xin, H., Kim, K., Liu, Y., Oxenloewe, L. K., Dong, P., & Hu, H., Intra-Datacenter Interconnects with a Serialized Silicon Optical Frequency Comb Modulator. *Journal of Lightwave Technology*, (2020).

205. Urbonas, D. *et al.* Ultra-wide free spectral range, enhanced sensitivity, and removed mode splitting SOI optical ring resonator with dispersive metal nanodisks. *Optics Letters* **40**, 2977 (2015).

206. Padmaraju, K. & Bergman, K. Resolving the thermal challenges for silicon microring resonator devices. *Nanophotonics* vol. 3 269–281 (2014).

207. Li, C. *et al.* Silicon photonic transceiver circuits with microring resonator bias-based wavelength stabilization in 65 nm CMOS. *IEEE Journal of Solid-State Circuits* **49**, 1419–1436 (2014).

208. Zhou, W. *et al.* Subwavelength engineering in silicon photonic devices. *IEEE Journal of Selected Topics in Quantum Electronics* **25**, (2019).

209. Kaushal, S. *et al.* Optical signal processing based on silicon photonics waveguide Bragg gratings: review. *Frontiers of Optoelectronics* vol. **11** 163–188 (2018).

210. St-Yves, J., Bahrami, H., Jean, P., LaRochelle, S. & Shi, W. Widely bandwidth-tunable silicon filter with an unlimited free-spectral range. *Optics Letters* **40**, 5471 (2015).

211. Leal-Junior, et. al. Commercial Polymer Fiber Bragg Grating Sensors: Review and Applications. *Journal of Lightwave Technology, Vol. 37, Issue 11, pp. 2605-2615* **37**, 2605–2615 (2019).

212. Zhang, C., Zhang, S., Peters, J. D., & Bowers, J. E., 8× 8× 40 Gbps fully integrated silicon photonic network on chip. *Optica*, *3*(7), 785-786, (2016).

213. Doylend, J. et. al.. Two-dimensional free-space beam steering with an optical phased array on silicon-on-insulator. *Optics express*, ***19***, 21595-21604, (2011).

214. Zhang, Y. et. Al. ., Sub-wavelength-pitch silicon-photonic optical phased array for large field-of-regard coherent optical beam steering. *Optics express*, *27*(3), 1929-1940, (2019)..

215. Simard, A. D., Beaudin, G., Aimez, V., Painchaud, Y. & LaRochelle, S. Characterization and reduction of spectral distortions in Silicon-on-Insulator integrated Bragg gratings. *Optics Express* **21**, 23145 (2013).